Chemical and Biological Controls on Coral Nucleation

Marta Wolfshorndl

A dissertation

submitted in partial fulfillment of the

requirements for the degree of

Doctor of Philosophy

University of Washington

2021

Reading Committee:

Alexander Gagnon, Chair

Gabrielle Rocap

Anitra Ingalls

Program Authorized to Offer Degree:

Oceanography

University of Washington

Abstract

Chemical and Biological Controls on Coral Nucleation

Marta Wolfshorndl

Chair of the Supervisory Committee:
Alexander Gagnon
School of Oceanography

Coral reefs are vibrant and important ecosystems in the oceans, but reefs today are under threat from multiple sources. One such threat is ocean acidification due to anthropogenic climate change, which is reducing both seawater pH and the thermodynamic driving force for $CaCO_3$-based biomineralization (oversaturation or Ω). It is known that coral skeletal growth will decrease in an acidifying ocean, but the detailed mechanisms driving this response are still poorly understood. In addition, there is a long-standing debate in the field regarding the relative impact of skeletal organic matrix proteins on calcification and nucleation, with some claiming that these proteins can mitigate the effects of ocean acidification. Nucleation is the first step of the skeleton growing process, and as such is the step that is thought to determine the pace, pattern, and strength of the coral skeleton, and by extension, the development of the very

framework that holds reefs together. We made the first quantitative measurements of inorganic aragonite nucleation and its sensitivity to Ω, mapping the energy landscape of nucleation kinetics, and finding that it is more sensitive to oversaturation than bulk mineral growth rates in the environmentally relevant range of Ω values. Furthermore, we combined inorganic mineral growth rates from the literature with the nucleation rates measured in this work in a numerical model to make predictions about how these two processes work together to affect the overall skeleton. In order to determine the extent of biological control over nucleation, we measured the quantitative effects of a peptide from the acidic domain of a matrix protein from *Stylophora pistillata*, as well as matrix protein analogues and polypeptides with different functional groups, on nucleation rates and other growth properties. We found that although the matrix protein and analogues had an effect on nucleation, it is unlikely that this protein can counteract the effects of ocean acidification. Overall, this work provides a comprehensive look at inorganic aragonite nucleation and the balance of chemical and biological controls on inorganic rates, as well as how these inorganic studies pertain to corals. These experiments quantify the limits of corals' ability to respond to the environmental pressure of ocean acidification on skeletal growth.

TABLE OF CONTENTS

LIST OF FIGURES

LIST OF TABLES

ACKNOWLEDGEMENTS

There are many people that I need to thank who helped to bring this thesis to fruition. First and foremost I would like to thank my advisor Alex Gagnon and the rest of the Gagnon lab for five fulfilling years. Over the course of many weekly meetings, Alex helped shape my critical thinking about science: what questions to ask, different approaches to take to answer questions, and helping me understand not just my data, but how the field of science works in general. In addition, Alex always encouraged me to follow my interests, even when those interests took me away from the lab.

The Gagnon lab, especially Isaiah Bolden and Elisa Bonnin, my fellow grad students, made grad school so much fun. I learned a lot from everyone and was lucky to work with such a great group, including Anne Gothmann, Dan Anderson, Tamas Ugrai, Amy Larsen, Nick Roden, Mary Margaret Stoll, Signe Bergman, and Keely Hall.

I also want to acknowledge and thank Julian Sachs, my advisor for my Master's, and my former lab mates, Nemiah Ladd, Dan Nelson, Matthew Wolhowe, Becci Danford, and Josh Gregersen. In particular, Tessa McGee was a wonderful office mate and I'm so glad I got to start grad school with her. Ashley Maloney was an amazing mentor and friend who taught me so much about lab and life.

The oceanography graduate student community was a welcoming and safe space for me during this time, and I appreciate everything they do to make our department non-competitive and the work they are doing to make it a more inclusive space for everyone. My cohort has been a great group to go through this journey with: Shirley Leung, Elisa Bonnin, Tessa McGee, Jake Steinberg, Halle Stone, Elizabeth Brasseale, Will Gagne-Maynard, Rachel Spietz, and Ben Bloss. The chemical oceanography ladies are an awesome group of

scientists and people, including Jiwoon Park, Katherine Heale, Hilary Palevsky, and Nancy Williams. They are all great role models for me and others. Susanna Michael and Angie Boysen were great friends who, most recently, went on mental health and pastry walks with me during the pandemic.

My community outside of grad school was just as influential in allowing me to complete this work. My Seattle friends, especially Shirley Leung, Katrina Lau, Sam Yeung, Thao Truong, and Chiara Conley, have gotten me through grad school and the pandemic. My college friends Sophie Wasserman, Sara Landers, and Emily Starace have been my rocks for over ten years now. My extended family in New Jersey has always had my back and have shown me so much love and support. My parents and brother have always believed in me, and have helped me so much during the down times. Finally, I could not have completed this thesis without the support and love of Ben Roth. Thank you for feeding me and believing in me. I can't wait for our next adventures.

Chapter 1. INTRODUCTION

Coral reefs are unique and important ecosystems that today are under threat from a variety of environmental changes. Coral reefs are thought to be home to approximately a quarter of marine species (1), are a substantial source of food for up to a billion people worldwide, and provide other ecosystem services for people, including protection from storms and tourism, that is estimated to be worth over $375 billion annually (2). However, anthropogenic climate change is impacting oceanic conditions and the future of coral reefs. One of the effects of anthropogenic climate change is ocean acidification, whereby CO_2 emitted from the burning of fossil fuels enters the ocean, becomes part of the buffering carbonate system, and subsequently lowers pH. Coral skeletons are made out of a form of calcium carbonate ($CaCO_3$) called aragonite, and ocean acidification shifts the speciation of the carbonate system to have less carbonate ion at equilibrium, lowering the saturation state of the ocean, Ω.

$$\Omega = \frac{[CO_3^{2-}][Ca^{2+}]}{k_{sp}} \qquad \text{(Chapter 1.1)}$$

where k_{sp} is the equilibrium solubility product.

There is significant evidence from culture studies that coral calcification decreases with decreasing pH in the ocean, although the functional form of the response varies significantly between species (3, 4). The mechanism of this effect has been attributed to a correlation between Ω and calcification in corals (3, 5, 6), because a decrease in external pH will decrease availability of CO_3^{2-} in seawater. The pH of the global average ocean has already decreased 0.11 units since preindustrial times (7), and it is predicted that the pH will further decrease by 0.2-0.4 units by 2100 (8, 9). This decrease in pH will result in an approximate decrease in CO_3^{2-} ion concentration by almost 60% (9). Taking into account combined effects of decreasing pH resulting in a decreased

CO_3^{2-} concentration and increasing temperatures, it is predicted that all corals will reduce their calcification rates relative to pre-industrial rates by greater than 80% when CO_2 atmospheric concentrations reach 560 ppm (10). Atmospheric concentrations of CO_2 will reach above 560 ppm by the end of the century given business-as-usual scenarios (11). Because of these drastic changes in the ocean, it is imperative to understand the exact mechanism of how corals calcify, identify the most sensitive step of calcification, explain the functional form of the response of corals to ocean acidification, and find and measure any intrinsic ability of corals to adapt to these changes.

1.1 NUCLEATION

Nucleation is the first step in calcification, a phase change when solid crystals form from ions out of solution, and was first shown in a series of studies by Gladfelter to be a process that behaves profoundly differently than that of overall skeletal growth and calcification (12–14). As the first step in the skeletal growth process, nucleation is likely to be vital for the growth of the entire organism, and by extension, the entire reef. Despite this importance, the sensitivity and response of nucleation to environmental factors such as ocean acidification have not previously been studied.

Classical nucleation theory (CNT) is one model for understanding the thermodynamics and kinetics that drive the nucleation process. In the classical model, nucleation occurs ion by ion as these molecules randomly move through solution and collide. The free energy of formation of a heterogeneous nucleus (ΔG^*) is given by the formation of a new phase on a surface as a function of the radius, r, of the nucleus under a given set of conditions. In order to form a stable nucleus on a surface, enough molecules must join together to form a nucleus that has a radius larger than the critical radius size (15). The main factors that affect the critical radius size are the interfacial

energy, which is the energy it takes to disrupt the bonds of the solution or the solution and the surface in order to form a stable nucleus, and the supersaturation, Ω, which controls the stability of the new solid. At equilibrium, the steady state nucleation rate, J, can be determined from the size of ΔG^*, which forms the thermodynamic barrier required to form a nucleus of a certain size. The nucleation rate equation can be written as:

$$J = Ae^{\frac{B\alpha^3}{\sigma^2}} \quad \text{(Chapter 1.2)}$$

Where A is the kinetic constant cofactor, determined by rate limitation of molecular motion, σ is the supersaturation term, equal to lnΩ, α^3 is the interfacial energy term, and B is a constant that is shape- and volume- specific and that is experimentally determined. This equation can be log-log transformed to be written as:

$$lnJ = lnA - B\alpha^3 \frac{1}{\sigma^2} \quad \text{(Chapter 1.3)}$$

The linear form of Chapter 1.2 is useful because it allows us to separate the parameters that affect nucleation within the CNT framework. When plotted, the slope of the line is proportional to the interfacial energy, and the intercept is related to A, which is the maximum nucleation rate under given conditions. If nucleation data is linear when $\frac{1}{\sigma^2}$ is plotted versus lnJ, then CNT is a reasonable empirical fit for nucleation under those conditions, whether or not the mechanistic details of nucleation follow this theory or not.

In Chapter 2, I measured nucleation rates using a flow cell set up at constant chemical conditions. For inorganic aragonite nucleation we observed steady state nucleation rates and found that these data could be fit using CNT. I therefore used this model as a framework to compare all of the inorganic nucleation experiments that I performed, including those in Chapter 3.

Other models of nucleation growth are accepted in the field of biomineralization, and usually are used to describe growth where the classical model cannot explain the observations. In particular, growth observations that are far faster than the classical model would predict have been explained by alternate dynamics. Some examples of these other explanations include particle attachment, prenucleation clusters, and amorphous precursors (16). CNT is generally the simplest model and since it fits our inorganic data we use it as a basis for comparison between different experiments and as a way to obtain estimates of different parameters to explain the kinetics observed. We discuss in Chapter 3 conditions under which the classical model does not hold and what dynamics might be occurring in those cases.

1.2 MECHANISM OF CALCIFICATION: INFLUENCES OF AQUATIC CHEMISTRY

Corals calcify extracellularly in the calcifying space located between the skeleton and two layers of tissue. The calcifying space must have a supply of ions needed for calcification, and one prevailing idea is that seawater supplies Ca^{2+} and CO_3^{2-} ions to this area of the coral (3, 17–20). The basis for many paleoproxies relies on the fact that coral skeletal composition is linked to the ionic, metal, or isotopic ratios and composition of seawater (e.g. Mg/Ca ratios or $\boldsymbol{\delta}^{18}O$ as temperature proxies).

However, it has also been shown that corals have a measure of control over the ionic composition of the calcifying space and can use this to create a more advantageous environment for calcification. By concentrating the ions that are most useful for calcification, they can drive up pH and Ω, and therefore the thermodynamic favorability of skeleton formation. Ca^{2+} ions diffuse in passively through spaces in between cells (20), or are brought in and concentrated by Ca^{2+}-ATPase (21, 22). Ca^{2+}-ATPase works by transporting Ca^{2+} in in exchange for two H^+ ions,

maintaining the ionic gradient, while simultaneously increasing the pH in the calcifying space and increasing Ω (22).

Direct and indirect measurements of calcifying fluid pH show that it is elevated above that of ambient seawater over a range of levels of exposure. Al-horani et al., 2003 used microelectrodes placed directly inside the calcifying space to observe a pH of 9.28, elevated above seawater pH of 8.2. Using pH sensitive fluorescent dyes viewed through confocal microscopy, Venn et al., 2011 found that pH values in the calcifying space were elevated above the surrounding seawater with a pH of 8.15 by 0.5 units in the light and 0.2 units in the dark. In another experiment, Venn et al., 2013 observed elevated pH values in the calcifying space across four pH treatments, with a pH of 8.42 at an exterior pH of 8.13 and a pH of 7.82 at an exterior pH of 7.28. Both experiments were done using the tropical Pacific coral *Stylophora pistillata*. Crucially, in this second experiment, although pH of the calcifying space was elevated above that of seawater at each pH treatment, the values still declined as the ambient seawater pH declined. The rate of decline was not equal internally and externally – the difference between the two values increased as external pH decreased. Indirect measurements of calcifying fluid pH using boron isotopes provide similar results, as do investigations into cold-water corals (Gagnon, 2013 and references therein).

This measured increase in pH shifts the carbonate equilibrium in the calcifying space, decreasing the amount of CO_2 and increasing the amount of CO_3^{2-}. This results in a corresponding increase in calcifying fluid Ω. Several indirect measurements and estimates of this Ω value have been made. Al-Horani et al., 2003 calculated that calcifying fluid Ω was ~25, well above the ambient seawater Ω value of 4 (average value in the ocean), while Venn et al., 2011 estimated Ω to range between 11-20, depending on whether the coral was under dark or light conditions. DeCarlo et al., 2017 used an empirical relationship between the calcifying fluid Ω and Raman peak

width in abiogenic aragonite to calculate Ω to be 12.3 ± 0.3 in the international coral standard JCp-1 (*Porites*) (26). One direct measurement of calcifying fluid Ω was made by Sevilgen et al., 2019, when they made microsensor measurements of calcium and carbonate ion concentrations in *S. pistillata* in light conditions. They calculated Ω to be 12.1 ± 3.6 (27). All of these studies agree on a range of Ω values in the calcifying fluid between approximately 8-25. These experiments tell us that corals have a measure of control over the calcifying space, which they can increase even as pH in the ocean is lowered; however, this control does not mean that they are impervious to the effects of ocean acidification.

The fact that corals' calcifying fluid pH decreases as external oceanic pH drops, even with an offset, indicates that the simple chemistry of external seawater exerts some level of control on calcification, which we term "geochemical control". As mentioned earlier, culture studies bear this out, exposing a linear relationship between seawater Ω and calcification. However, the exact response of individual corals and different coral species to Ω varies considerably, with corals displaying a wide array of tolerances for increasingly acidic conditions (3, 4). The geochemical story alone seems insufficient to explain the variety of functional responses to ocean acidification, and a debate has arisen in the field about the relative importance of the skeletal organic matrix (SOM) in controlling coral calcification and its response to ocean acidification.

1.3 MECHANISMS OF CALCIFICATION: INFLUENCES OF ORGANIC MATRIX PROTEINS

The SOM, a layer of proteins that are laid on top of and incorporated into the skeleton of biomineralizing organisms, has long been known to exist, and the nature of its influence on calcification long been speculated on. Goreau, 1959 proposed a mechanism of action for an SOM

in corals consisting of “an acid mucopolysaccharide-like substance” that acts as a template for Ca^{2+} adsorption, eventually leading to $CaCO_3$ formation (Goreau, 1959) . Mitterer, 1978 later found that approximately 40-50 mole percent of the amino acids associated with the SOM in five scleractinian coral species were acidic residues, with aspartic acid in highest abundance, which he predicted acts as a Ca^{2+} binder (Mitterer, 1978). Constantz and Weiner, 1988 further discovered that the acidic residues were part of an assemblage of glycoproteins that contained sulfated polysaccharide side chains in two coral species Constantz and Weiner, 1988. The high percentage of acidic residues and glycine in SOM proteins was further confirmed in two coral species by Ingalls et al., 2003, who also found that amino acids from mineral precipitating proteins made up 30-45% of total organic carbon preserved in the skeletons of both corals. Proteins isolated from the SOMs of other biomineralizing marine organisms such as mollusks have been highly acidic in nature (32), indicating that this motif in SOM proteins might be conserved across biomineralizing organisms.

The SOM has been thought to have a potential role in nucleation. It has been theorized that the SOM could promote nucleation by lowering the surface energy of the nucleating substrate or by participating in ion organization and orientation. Conversely, it could have a role in calcification by inhibiting excessive growth along certain faces of a mineral surface (32, 33). Only recently have specific proteins from the SOM of the tropical coral *Stylophora pistillata* been isolated and identified, and a group of highly acidic proteins with alternating conserved non-acidic domains came to light (known as coral acid rich proteins or CARPs) (34). Roughly half of the amino acids in these CARPs are acidic residues, primarily aspartic acid. Preliminary analysis indicates that at least some of these proteins are conserved (31-85% of known sequence) across four different species of corals, and are not found outside of the order *Scleractinia* (34, 35).

The first experiments testing the effects of SOM proteins on calcification used matrix protein analogue templates to quantitatively measure the effect on nucleation orientation, shape, and rate. Primarily these experiments measured calcite, the most stable form of calcium carbonate, produced by organisms such as foraminifera. A series of experiments in the 1990s measured how organic templates controlled orientation of $CaCO_3$ nucleation. Mann et al., 1993, Heywood and Mann, 1994, and Aizenberg et al., 1999 grew calcite and aragonite nuclei on different organic template surfaces and found they could control the specific face of orientation depending on the head group of the organic template. Mann et al., 1993 attributed this mechanism to stereochemical complementarity between surface and crystal. Teng et al., 1998 and Orme et al., 2001 measured effects of acidic organic molecules on calcite nucleation thermodynamics and kinetics in an effort to reconcile previous viewpoints of stereochemical effects of organic molecules with kinetic effects. They used atomic force microscopy (AFM) and molecular modelling to determine that aspartic acid changed both the crystal morphology and the surface energy of the nucleating substrate and the growing crystal edge, leading to the conclusion that organic matrix proteins act through both stereochemical matching and surface energy changes.

Hu et al., 2012 and Hamm et al., 2014 further explored the kinetic effect of organic molecules on nucleation by measuring quantitative calcite nucleation rates as they formed *in vitro* on surfaces templated with differently functionalized self-assembled monolayers. Nucleation rates were specific to each substrate head group and tail length and could easily be explained by reductions in thermodynamic barriers due to changes in interfacial energy between nucleus and surface. Furthermore, they found that the relationship between nucleation rate and the surface energy of each template-covered substrate matched that of the CNT model of growth. In addition to determining that SOM protein analogues affect rates of nucleation as well as orientation, these

experiments showed that CNT is a reasonable and useful model for measuring the relationship between changes in surface energy and resultant changes in nucleation rates.

Experiments measuring the effects of specific coral SOM proteins (CARPs) on coral calcification *in vitro* were done by Mass et al., 2013. In those experiments, the only ones that directly tested both the effects of CARPs and pH on calcification, they incubated CARPs 1-4 individually in artificial seawater under two different pH conditions: 8.2 and 7.6. In comparison to two controls, which were incubated with bovine serum albumin (BSA) or with His-tagged glycosyl hydrolase 2, they noted the precipitation of calcium carbonate crystals in both pH treatments of CARP incubations. Mass et al., 2013 proposed a mechanism of calcium binding to the acidic regions of CARPs, which raises the ionic strength of the microenvironment and subsequently lowers the pKa of the microenvironment, and increases the proportion of CO_3^{2-} ion present locally.

In later experiments with CARPs, Mass et al., 2014 observed CARPs embedded within the skeleon of *S. pistillata* using immunogold labelling assays, with each CARP having a unique location and a presumed unique function in the SOM. CARP1 was localized to the early mineralization zones, where nucleation occurs, while CARPs 2 and 3 were found in different areas of the mineral growth layers. CARP4 was found in both the nucleation areas and the growth layers (43). In addition, immunohistochemical staining was used to localize CARPs in the coral tissue. CARPs 1, 2, and 3 were found in the cells associated with forming the skeleton, while CARP4 was located around the desmocytes, connecting cells between skeleton and tissue (43). In 2016, expression patterns of CARP family genes were analyzed during the early life stages of *Pocillopora damicornis* larvae, and genes for CARPS 1, 3, 4, and 5 were upregulated during the post settlement stage of the larvae, when they were building aragonite skeletons, while CARP2 was upregulated during the earlier phase when the larvae settle (44). Furthermore, CARPS 1, 3,

and 4 were found to be localized to the cells near the skeleton during this same phase. A similar expression pattern during life stages was observed in *S. pistillata*, by Akiva et al., 2018, who also observed that CARPs 1, 3, and 4 were associated with aragonite skeleton while CARP2 was more highly associated with amorphous calcium carbonate using NMR techniques (45).

Mass et al., 2017 also observed CARPs 1 and 4 co-localized on newly forming crystals produced extracellularly on *S. pistillata* proto-polyps. Drake et al., 2017 measured gene expression in *S. pistillata* proto-polyps grown under low (400 ppmV) to high (2000 ppmV) pCO_2 levels. They found that at the highest pCO_2 levels, genes for CARPs 3 and 4 were up-regulated, and calcification occurred at every pCO_2 level, even when aragonite was under saturated (gene expression for CARPs 1 and 2 was not measured). Finally, two studies have found that CARP3 affects polymorph selection of calcium carbonate *in vitro* from artificial seawater solutions, forming either Mg-calcite or vaterite (48, 49).

These experiments taken together show that some or all of the CARPs are involved in biomineralization in corals. In particular, the different temporal and spatial localization of CARP2 compared to the other CARPS may indicate that it is CARPs 1, 3, and 4 which play a crucial role in biomineralization in adult coral. In addition, CARPs 1 and 4 specifically are found to be localized near nucleation sites in coral skeletons, which may mean they are involved in nucleation and growth, while CARP3 possibly plays a role in polymorph selection. Overall, the roles of individual CARPs are still unclear, and there are many open questions about how CARPs may affect calcification and nucleation, and how these effects fit in with the the idea of geochemical control of calcification. My dissertation will use quantitative measurements of inorganic nucleation at a range of chemical conditions and with different organic matrix protein analogues

to help unite these two viewpoints about the control of skeletal growth and gain further insight in the mechanism of calcification.

1.4 CHAPTER OVERVIEW

Chapter 4 of my dissertation for my master's work focused on a different aspect of geochemistry, investigating hydrogen isotope ratios of algal lipids as paleoproxies for rainfall and climate in tropical locations. This chapter compared culture and field studies to examine how growth rate and irradiance affect $^{2}H/^{1}H$ ratios in alkenones, lipids produced by coccolithophores. I found that both growth rate and irradiance can affect $^{2}H/^{1}H$ ratios in lipids, but that effects seen in the field were much smaller than those observed in the lab.

For my PhD work, in Chapter 2, I made the first quantitative measurements of inorganic aragonite nucleation at different Ωs to determine the sensitivity of nucleation to ocean acidification. I found that aragonite nucleation will respond more quickly to changes in environmental Ω than mineral growth rate because it has a more sensitive response to Ω in the range of values that are occurring in the calcifying space. Furthermore, I used a numerical model to predict what the combined effects of the different responses of mineral growth and nucleation to Ω may have on the overall coral skeleton, and found that nucleation is crucial in increasing horizontal growth above mineral growth rate alone, but does not play a large role in vertical growth of the coral. In Chapter 3, I explored the effects of organic matrix protein analogues and CARPs on inorganic nucleation over a wide range of Ω values. In this chapter I found that a peptide from the acidic domain of CARP1 has the ability to elevate nucleation rates at Ω values above 15.2, but that it inhibits nucleation below this Ω. I also determined that chain length and polypeptide functional group play a role together in effecting nucleation growth.

As a whole, these chapters provide a comprehensive picture of aragonite nucleation and its response to the chemical environment the coral is grown in as well as organic matrix proteins that the coral may produce, showing how the balance of these forces provide a means of control over the nucleation process.

Chapter 2. MEASURING AND MODELING INORGANIC ARAGONITE NUCLEATION TO PREDICT IMPACTS OF OCEAN ACIDIFICATION ON CORAL REEFS

2.1 ABSTRACT

Nucleation acts as a gatekeeper, controlling the location, timing, and even the composition of skeletal growth in both juvenile and adult coral, with implications for calcification rates in a changing ocean, coral-based paleoproxies, reef strength in the face of storms, and larval development. However, the energetics and regulation of this critical chemical process are poorly understood in coral. Indeed, the same characteristics that allow nucleation to act as a useful physiological checkpoint, namely large energy barriers coupled with high-order sensitivity to local chemistry, also imply that nucleation should be exceptionally sensitive to environmental conditions like ocean acidification. We conducted inorganic nucleation rate experiments under controlled chemical conditions to measure the sensitivity of aragonite nucleation in seawater to oversaturation, and determined that, in the range of environmentally relevant oversaturation values, nucleation is more sensitive to the chemical environment than mineral growth rate is. Using our inorganic nucleation rates and aragonite mineral growth rates from previous work, we developed a numeric model to predict how the relative sensitivities of these two modes of growth affect calcification. We found that horizontal extension of the skeleton is controlled by nucleation while vertical extension is controlled by mineral growth rate, and that horizontal extension is therefore potentially more tunable by the coral through the use of interfacial energy changes from organic matrix proteins. These experiments quantify the limits of corals' ability to respond to the environmental pressure of ocean acidification on skeletal growth.

2.1 INTRODUCTION

Coral reefs are important ecosystems in the ocean that are home to a wide diversity of organisms, act as coastal barriers against storms, and provide numerous economic benefits to people all over the world. Coral reefs in the oceans today are affected by anthropogenic processes, including ocean acidification, whereby human emitted carbon dioxide in the atmosphere equilibrates with the carbonate system in the oceans, lowering the pH. Adding CO_2 to the carbonate system shifts the equilibrium in a mix of bicarbonate (HCO_3^-) and carbonate (CO_3^{2-}) to having more HCO_3^- and less CO_3^{2-}. The generalized reaction for the system can be seen below.

$$CO_2 + H_2O \rightarrow HCO_3^- + H^+ \qquad \text{(Chapter 2.1)}$$

Reef-building stony corals build their skeletons out of a form of calcium carbonate ($CaCO_3$) called aragonite, and require a supply of CO_3^{2-} in the ocean to grow and thrive. The term for the thermodynamic potential of the $CaCO_3$ to form is called the saturation state (Ω), and is represented by the equation:

$$\frac{[Ca^{2+}][CO_3^{2-}]}{k_{sp}} = \Omega \qquad \text{(Chapter 2.2)}$$

where k_{sp} is the solubility product at equilibrium. If Ω is greater than 1, $CaCO_3$ can spontaneously form in the ocean, and if it is lower than 1, dissolution occurs. Environmental Ω has an average value of 3.03 across the global ocean today, and is higher in the tropics (50). Ocean acidification causes a decrease in Ω because it decreases the concentration of CO_3^{2-} ions present in the water, and by 2100, the pH of the average global ocean is predicted to decrease a further 0.2-0.4 units from present (8, 9). This decrease in pH will result in an approximate decrease in CO_3^{2-} ion concentration by almost 60% (9). Culture studies have shown that the overall growth of corals is correlated to the Ω value that the corals are grown in, showing that this chemical parameter is the

ultimate external control on coral growth, although the functional form of the response varies between species (3, 5, 6).

The mechanism of this control and of the coral skeletal architecture as a whole is more complicated, however. Corals calcify their skeletons internally in an extracellular chamber between their layers of tissue and the old skeleton called the calcifying space. Although this space is isolated from seawater, multiple experiments have shown that seawater does enter the calcifying space and is possibly the main source of ions for calcification (3, 17–20). The corals have a measure of control over the ions in the fluid calcifying space – the pH in this fluid is shown to be elevated above that of the surrounding seawater through both direct and indirect measurements (22–25). However, as the external pH decreases, the calcifying fluid pH also decreases, showing that the pH is not completely independent of the environment (25).

Several studies have attempted to estimate the calcifying fluid Ω value. One study by Venn et al., used pH sensitive dyes to measure the pH of the calcifying fluid of *Stylophora pistillata*, and then made estimates of carbonate system parameters, calcium concentration, and temperature in the fluid to estimate internal Ω to be between 11-20, depending on whether the coral was in dark or light conditions (51). Another study by Al-Horani et al. directly measured pH in the calcifying fluid of *Galaxea fascicularis* using microsensors, and then estimated internal Ω to be ~25 in the light based on their working model of calcification (22). DeCarlo et al. utilized a relationship between the calcifying fluid Ω and Raman peak width in abiogenic aragonite to calculate Ω to be 12.3 ± 0.3 in the international coral standard JCp-1 (*Porites*) (26). There has only been one calculation of calcifying fluid Ω using direct measurements of each parameter. Sevilgen et al. used microsensor measurements of both calcium and carbonate concentrations to directly calculate Ω to be 12.1 ± 3.6 in *S. pistillata* in the light (27). Both estimates and the one direct measurement of

calcifying fluid Ω agree on a general range of values in multiple different species and under different experimental conditions.

Although the relationship between overall skeletal growth rates have been measured in cultures and in the field, the mechanism and detail of the coral calcifying process is not fully understood. A longstanding question in the field of biomineralization is regarding the role of the skeletal organic matrix, a group of proteins and other biomolecules produced by the organism and thought to aid in calcification. Research of these proteins across different organisms, including corals and mollusks, has found that the organic matrix contains proteins that are highly acidic, a feature conserved across different species and clades (28–32). The identities of these proteins and other organic matrix molecules have been unknown until relatively recently, when proteins were identified from three coral skeletons from the families Pocilloporidae and Acroporidae using proteomics methods ((34, 52, 53). All three studies found acid rich proteins in the SOM. In particular, four acidic proteins were predicted from the genome of the tropical Indo-pacific coral *Stylophora pistillata* (35).

Since then, multiple studies have investigated the role these specific proteins play in calcification, determining that acidic proteins are located in the skeleton itself, near to nucleation sites, are upregulated when corals are grown under higher concentrations of CO_2, can promote calcification even under low Ω conditions, and can possibly select polymorphs (35, 43, 46–49). Fundamental questions that have remained unanswered are to what extent the organic matrix in corals can counteract the effects of external changes in pH, as well as the mechanism of how these proteins work to promote nucleation and calcification. Understanding the balance between organic matrix control of calcification versus geochemical control of calcification would enable more accurate predictions of the future of coral reefs in the ocean.

In order to make predictions and policies regarding the future of corals in the ocean, the skeletal growth process needs to be better understood. Coral skeleton formation has two main steps: nucleation followed by crystallization or mineral growth (12–14). Nucleation is the first step in the formation of a new phase, when the ions in solution form a solid and are deposited on the old skeleton. Nucleation is a random process that should be dependent on the thermodynamic potential of the calcifying fluid (15). Crystallization is the next step where nuclei get larger, and crystals overgrow and infill around the nuclei and become ordered. In the larger scale of the microstructure of the coral skeleton, nuclei appear as centers of calcification (COCs), linear features within the skeleton parallel to the axis of growth surrounded by aragonite fibers (32). These two processes likely have different rates of growth and would respond differently to the same environmental changes. However, while overall skeletal growth has been measured often in culture and field studies, these two processes have not been separated out and measured independently. Specifically, nucleation is the first step of skeletal growth and must therefore play a role in determining overall growth patterns and density, but rates of growth and sensitivity to changes in the chemical environment have never been measured.

Here we report the first quantitative measurements of inorganic aragonite nucleation, providing an understanding of the kinetics and thermodynamics of that process. We find that nucleation growth rate is more steeply sensitive to changes in Ω than aragonite growth rate in the environmentally relevant range of Ωs, which has implications for predicting the future of corals in the ocean. Using an inorganic numerical model of nucleation and crystal growth, we predict skeletal growth parameters, including linear extension, calcification, and ratio of nuclei to volume, for both horizontal and vertical growth in corals, and find that nucleation can greatly increase horizontal linear extension as compared to growth with no nucleation.

2.2 METHODS

2.2.1 *Aragonite Nucleation Rate Measurements*

Two solutions of modified seawater, one containing Ca^{2+} and alkalinity and one containing DIC, were mixed together in spiral tubing using a microprocessor-controlled peristaltic pump at 4 mL/min. The solutions were pumped into a Warner Instruments Low Profile Parallel Plate Flow Chamber (RC-31) with laminar flow and glass slides on top and bottom. The volume of the flow cell chamber was 0.234 cm^3, and the residence time was 3.51 seconds. The solutions were held at a constant temperature of 25°C and continuously pumped out through the exit line of the cell. Nucleation occurred heterogeneously on both surfaces, and was monitored on the underside of the top glass slide of the flow cell. The cell was placed under a Nikon Eclipse E600 POL microscope with cross-polarized light and time-lapse images were taken throughout each experiment every 30 seconds or more frequently. The microscope was focused on the underside of the top glass slide and recorded each nucleation event as it occurred. Any homogeneous nucleation events that occurred in the solution or nuclei that landed on the bottom slide were not recorded. Experiments lasted between 1-7 hours, depending on the Ω, which varied between 5-120. Forty experiments were performed, 32 of which were used for the final analysis. The experiments that were not included had technical problems with the experimental setup, such as leaking of solution, bubbles entering the flow cell and obscuring the field of view, or incorrect focus, or had clear evidence of non-random configuration of the nuclei, such as a consistent non-random pattern across the entire field of view, attributable for example to scratches on the glass.

2.2.2 *Preparation of Solutions*

The two modified seawater solutions contained NaCl and when mixed together had an ionic strength of 0.67, close to the ionic strength of seawater, which is approximately 0.7 (55). They were created for each nucleation experiment or group of experiments at a specified Ω. Solutions contained salinity of 35, the carbonate alkalinity, and some of the major ions of seawater, including Na^+, Cl^-, Ca^{2+}, and Mg^{2+}, but did not contain SO_4^{2-}, K^+, Sr^{2+}, Br^-, $B(OH)_3$, or F^-, any minor ions, trace metals, nutrients, or other dissolved species found in natural seawater.

Both solutions contained NaCl from the same batch solution, and one solution contained Ca^{2+} and Mg^{2+}, added through $CaCl_2 \cdot 2H_2O$ and $MgCl_2 \cdot 6H_2O$, while the other contained sodium bicarbonate ($NaHCO_3$) and sodium hydroxide (NaOH). The amount of NaOH was varied to change the pH of the final solution, and therefore Ω, while DIC was held constant at 0.008 mol/kg. The concentrations of Ca^{2+} and Mg^{2+} were held constant at 0.01 mol/kg and 0.02 mol/kg, respectively. Higher Mg^{2+} concentrations led to precipitation of brucite at the high pH levels maintained in these experiments. Supplementary Table 2.2 lists the solution chemistry for each experiment. Ω remained constant throughout the experiment because of the flow-through system replenishing the chemistry of the solutions in the cell. The rates of nucleation and aragonite growth at even the highest Ω do not draw enough $CaCO_3$ out of solution to change the Ω in the cell substantially (calculation for highest Ω value in supplemental). At Ω values below 50, the maximum change in Ω possible due to nucleation and aragonite do not change Ω more than 1 unit or 2%, with a corresponding decrease in $\Delta\Omega$ as the prescribed Ω decreases (Supplementary Table 2.3).

2.2.3 *Characterization of Nuclei*

Nuclei on the glass slide were characterized by light microscopy, Raman spectroscopy, and scanning electron microscopy (SEM) (Supplementary Figure 2.11 and Figure 2.12). A Renishaw InVia Raman system equipped with a Leica DMIRBE inverted optical microscope with a laser excitation source at 514 nm was used to ascertain the identity of the crystals, and Raman spectra of aragonite and calcite standards were collected as a comparison. These methods verified that the majority of the nuclei were aragonite.

2.2.4 *Calculating Nucleation Rate and Relationship between Nucleation Rates and Ω*

For each experiment, the nucleation rate was calculated by counting the number of nuclei in each image and plotting the number of nuclei versus time. When the relationship of the two is linear, it signifies steady state nucleation growth, and the slope of the line is the rate (Supplementary Figure 2.10). All rates were normalized to area.

The exponential plot between nucleation rates and Ω was fit by first fitting the linear form of the log-log plot between these two parameters using a weighted linear regression and transforming the linear equation of fit for the exponential plot.

2.2.5 *Nucleation Model*

The nucleation model used the inorganic rates of nucleation (measured in this study) and aragonite mineral growth (56) as the parameters controlling growth of the skeleton. A flow chart outlining the steps the simulation takes is contained in the supplemental (Figure 2.13). Both the nucleation rate and the mineral growth rate are dependent on Ω, which is held constant for each simulation. Nuclei are represented by hemispheres for ease of simulation and model representation. A single nucleus with radius of 0.005 μm was deposited randomly in a given area

of a 100 μm^2 box to start a simulation. At each time step moving forward, the probability of additional nucleation is evaluated and nuclei that are already present grow at a fixed rate. The amount of growth was determined by the length of the timestep and the mineral growth rate dependency on Ω (56). The probability that a nucleus was deposited was determined by the length of the timestep, the area (held constant), and the nucleation rate J. The placement of each new deposited nucleus was done randomly.

To start each simulation, the deposition surface is flat and the probability of deposition in any given region is equal to any other region of the same size. As soon as nuclei are deposited, the deposition surface becomes irregular, and it is more complicated to determine the overall surface area, associated nucleation rate, and location of nucleation. To determine these quantities, a 3D grid of the surface of the nuclei and deposition plane was created, with 1 μm x 1 μm size grid cells. The overall model domain was 100 by 100 grid cells, and boundary conditions were not periodic. The area of each grid cell is calculated and the probability of randomly placing a new nucleus in a particular grid cell is weighted by area. Once a grid cell is chosen as the deposition point, the nucleus is randomly placed within the cell. For each timestep, the surface grid is recalculated to update the grid with any new nuclei present and the larger size of the nuclei that had grown. Nuclei were allowed to deposit on top of other nuclei and grow continuously throughout each simulation. The timestep length varied depending on Ω, with a typical timestep in the tens of seconds.

Model runs were done at Ω values of 5, 7.5, 10, 15, 20, 25, 30, 60, and 90 and for each Ω, three repetitions were performed. The model was run until growth had reached steady state conditions, which were determined to be when the vertical linear extension rate and the vertical calcification rate were constant with time. Horizontal growth was determined using the time point at which the initial surface was 90% covered. Horizontal growth is a non-steady state process, so the area of

the box is important in determining the resulting rates from the model. The box length chosen of 100 μm per side enables comparison between the horizontal and vertical extension rates because it is similar in scale to the average height when steady state is reached (between 25 -70 μm).

To ensure that choosing a spherical shape for nuclei isn't unduly influencing the model results, we tested running the model using oblate and prolate spheroids, cubes, and rectangular prisms as nuclei shapes. Each shape was tested at a range of Ω values, and it was found that the shape did not influence the trends or overall conclusions resulting from the model.

2.2.6 *Acropora Samples Grown Using the Flat Growth Prep Technique*

The flat growth prep samples for comparison were *Acropora* species that were grown in salinity of 40 using Red Sea water on glass slides. Samples were provided by Jonathon Erez's lab. The coral samples were imaged using SEM with back scattered electrons (Supplementary Figure 2.15). Nuclei appeared as irregular rings of concentric circles throughout the skeleton. These rings were determined to be nuclei because they also appeared in the individual nuclei that were forming in the areas of new growth of the skeleton. Nucleation density of these samples was measured through manual counting.

2.3 RESULTS

2.3.1 *Inorganic Nucleation Rate Measurements*

Nucleation occurred on the glass slide in the flow cell at a range of Ω values from 5.5 through 118 (Figure 2.1 for examples). At higher Ωs, nucleation events occurred more quickly and had a faster induction time. The linear portion of these plots were used to calculate the rates of nucleation at each Ω. In each experiment, after the linear section of the plot, the number of nuclei over time tapered off asymptotically with little or no growth (not shown in Supplementary Figure 2.1).

Figure 1). The log of the nucleation rates was plotted versus Ω to determine the sensitivity of aragonite nucleation to this chemical parameter, and showed that the relationship between the two is exponential (Figure 2.2). From the fit of this relationship, it can be determined that aragonite nucleation is most steeply sensitive to supersaturation at lower values of Ω. In the range of 10-20, if Ω drops by 1, nucleation rate drops by ~15%. This range is the most environmentally relevant because it is the estimated range of values of Ω in the calcifying space in corals. These nucleation experiments are a direct analogue to processes occurring in the calcifying space.

2.3.2 *Output of Skeletal Growth Model*

The sensitivity of aragonite nucleation to Ω and the sensitivity of aragonite mineral growth rate to Ω were compared and used as inputs in a skeletal growth model to quantitatively determine the effects of their different responses to external parameters on the overall skeleton (56). Figure 2.3 shows that there is a textural difference in the skeleton grown at different Ω values, with the surface being much less smooth at Ω = 5 compared to the Ω values of 10, 15, and 20. This textural difference is due to the relative influence of mineral growth and nucleation.

The total volume, nuclear density on a flat surface, calcification rate, horizontal linear extension rate, and ratio of nuclei to total volume were all calculated at a range of Ω values from 5 to 90 when 90% of the surface area was covered in order to compare across Ω values when the skeleton was growing horizontally (Figure 2.4, Supplementary Table 2.4), and the calcification rate, vertical linear extension rate, and ratio of nuclei to total volume were calculated for the same Ω values when the model was in steady state vertical growth (Figure 2.5, Supplementary Table 2.5). Steady state was determined to be when the vertical growth rate and calcification rate became linear with time.

For both horizontal and vertical growth, the calcification rate increases as Ω increases in non-linear fashion, as a product of x^2, although the rates for vertical growth are slightly higher than those for horizontal growth. The horizontal linear extension rate and the vertical linear extension rates also both follow the form of a quadratic, with the linear extension rates higher for the same Ω values than the vertical extension rates. The ratio of nuclei to total growth, representing the nuclear density in the volume of the skeleton, has the same trend for both horizontal and vertical growth, with a maximum value at Ω = 15. The nuclear density on a flat surface, representing nuclear density per area, follows the same general pattern, with a broader peak at Ω values of 15 and 20. As Ω decreases from 15 to 10, nuclei to volume ratio drops by ~25% in horizontal growth and vertical growth calculations, while the nuclear density on a surface drops by 16%. The total volume measured when the surface area is 90% covered has the opposite trend, with a broad minimum around the Ω value of 15. Total volume increases by ~11% as Ω values change from 15 to 10, but there is a sharp increase in values from 10 to 5, with an increase in volume of >100%. The time it takes to cover the surface area increases as Ω values decrease, meaning it would take 2.3 times as long to cover the same amount of surface at an Ω of 10 versus an Ω of 15.

When compared to inorganic mineral rate of growth of aragonite, calcification rates from both horizontal and vertical growth and vertical linear growth rates are all very similar to the inorganic rate across the range of Ω values (Figure 2.8). Horizontal linear extension is the only rate measured that has a greater magnitude than the inorganic mineral rate of growth alone.

2.4 DISCUSSION

2.4.1 *Inorganic Nucleation Measurements*

Rate Measurements and CNT

In this study, to our knowledge, were made the first quantitative measurements of aragonite nucleation rates on a substrate. Full kinetic constraints of the skeletal growth process in corals can be determined for the first time, combining this data with bulk mineral growth rates. Rate measurements of aragonite nucleation can be used not only to determine the sensitivity of nucleation to specific chemical properties of the environment, but also to determine quantitatively the mechanism of how this nucleation sensitivity occurs. Classical nucleation theory (CNT) is a way to understand the thermodynamic and kinetic factors that govern the process of nucleation and provides an equation for understanding the terms of the process (57, 58). The free energy of formation of a nucleus (ΔG^*) is given by the formation of a new phase on a surface as a function of the radius, r, of the nucleus under a given set of conditions. ΔG^* is a function of the supersaturation and the interfacial energy, an energy penalty that the nucleus must pay as it is forming, caused by interactions with the nucleating surface and solution. At equilibrium, the steady state nucleation rate, J, can be determined from the size of ΔG^*, which forms the thermodynamic barrier required to form a nucleus of a certain size. The nucleation rate equation can thus be written as:

$$J = Ae^{\frac{B\alpha^3}{\sigma^2}} \qquad \text{(Chapter 2.3)}$$

A is the kinetic constant cofactor, determined by rate limitation of molecular motion, σ is the supersaturation term, equal to $\ln\Omega$, α^3 is the interfacial energy term, and B is a constant that is

shape- and volume- specific and that is experimentally determined. Equation 2.3 can be log-log transformed to be written as

$$lnJ = lnA - B\alpha^3 \frac{1}{\sigma^2} \quad \text{(Chapter 2.4)}$$

This linear form of the equation is useful because the slope of the line, $B\alpha^3$, is proportional to the interfacial energy penalty, and the intercept is lnA, a term that provides information about molecular motion and the maximum nucleation rate possible in given conditions. Equation 2.4 can be fit to the data shown in Figure 2.2 measuring nucleation rates. This has been done in Figure 2.6, showing two model fits for the data when plotted as lnJ versus $\frac{1}{\sigma^2}$. The linear fit (adjusted R^2 = 0.63, p-value << 0.001) between the two parameters is predicted by classical nucleation theory, and from this fitted line, the interfacial energy and ln A can be calculated to be 6.74 mJ/m^2 and 15.38, respectively. We include the quadratic model (adjusted R^2 = 0.71, p-value << 0.001) of the data to show an alternate fit, which would suggest that nucleation formation is non-classical, at least under these conditions and at higher Ω values. It is possible this alternate fit provides a better prediction of the relationship between nucleation rate and Ω, which is why we include it here. However, because there is no overwhelming evidence in favor of one model over the other, and in the region of environmentally relevant Ω values, the fit appears linear, we use the linear relationship moving forward.

Assuming classical theory holds, the critical radius of the nuclei forming, or the minimum value the radius needs to be in order for the nuclei to form, can be determined from these equations and the experimental setup. The critical size of the nucleus and therefore the critical radius can be found when ΔG^* is at a maximum, thereby determining the energy barrier to nucleation. Using Supplementary Equation 2.6, finding the maximum free energy and solving for r gives the equation for the critical radius as

$$r^* = \frac{2\alpha v}{\sigma k_B T} \quad \text{(Chapter 2.5)}$$

Where k_B is the Boltzmann constant and T is the temperature. The critical radii measured in this experiment over a range of Ω values can be seen in Table 2.1, as well as the number of molecules that fit inside the critical radius. The critical radius displays asymptotic behavior with respect to Ω, with values of the critical radius increasing sharply as Ω drops below 30, while above 30 is the same value to 8 decimal places.

The fact that the inorganic aragonite nucleation data can be fit with the CNT equation is significant because it provides a simple model of growth from which to compare nucleation kinetics in different conditions. Knowing rates of growth under different saturation states as well as the critical radius of the nuclei allows predictions of nucleation rates in live coral for the first time. The critical radii data show that the size of the radius, and therefore the nucleation rate, is fairly insensitive to Ω above a value of 30. In the range of Ω values below 30 where radius size is sensitive to Ω values, the critical radius doubles in size from 30 to 5. This range of Ω values lines up with the range of values that have been predicted and measured for the calcifying space in corals. It is reasonable for these values to align because corals have presumably optimized the process of increasing Ω values of the calcifying fluid space, and therefore kinetics, as much as possible for the least amount of energy; at higher values of Ω above 30, any change in Ω values would only minimally impact kinetics and would not energetically be worthwhile for the coral to invest in.

Using a CNT framework to understand inorganic data is useful because it provides a way to separate effects of the chemical environment, such as changes in Ω, from other possible factors that are thought to affect nucleation in corals, such as the organic matrix. These experiments provide a baseline of kinetics and interfacial energy between aragonite and a glass substrate over

a range of Ωs, and this baseline will be a useful comparison for future experiments measuring effects of organic matrix proteins on nucleation rates. Besides assessing how biomolecules affect the rates of growth, the CNT framework allows for elucidation of mechanisms as well. If nucleation rates in the presence of organic matrix proteins fit into the CNT model, changes in the interfacial energy or in *lnA* as compared to the baseline values measured in this study would point to either reducing the energy barrier to nucleation or to controlling the process of molecular organization, respectively. These questions have long been speculated on in the biomineralization community. If the data does not fit into the CNT model, information is still provided about how the organic matrix works to change the nucleation process.

To put the calculated interfacial energy between aragonite and glass in this study (6.74 mJ/m^2) in context and check the validity of using CNT, we compare to other measured or predicted interfacial energies for calcium carbonate of various forms. The surface energy of an aragonite nucleus formed homogeneously in water was calculated to be 280 mJ/m^2 (59), and it is reasonable that this value is much higher than for aragonite nuclei formed heterogeneously on glass. There have been no other interfacial energies reported specifically for aragonite in the literature that we could find. As a reference, interfacial energies measured for calcite, or calcium carbonate precipitation assumed to be calcite, on a variety of surfaces, in different solution types, and with different precipitation techniques yield energies that range from 37.3 to 97 mJ/m^2 (42, 60–65). The surface energy of a calcite nuclei formed homogeneously in water was calculated to be 210 mJ/m^2 (59). For vaterite, heterogeneous measurements range from 7 to 77 mJ/m^2, with 90 mJ/m^2 predicted for homogeneous vaterite (30 and references therein). Although these values are not directly comparable to aragonite on glass, they provide context for the number in this study, and show that the CNT fit to the data provides a reasonable interfacial energy.

Implications for Corals

Now that the sensitivity of nucleation to Ω has been measured, it is possible to compare how nucleation and mineral growth rates are impacted by changes in Ω in the environment. That comparison is shown in Figure 2.7. Inorganic aragonite growth rate data was obtained from (56), in order to compare to the inorganic nucleation data of this study. Inorganic aragonite growth rates were measured in units of mol/m^2/h. Units of growth rate and nucleation rate were both normalized to their respective values at Ω = 10 to be able to compare the respective curves of the two relationships with Ω. It can be seen in the inset in Figure 2.7 that the shape of the two curves are different, with nucleation rate having a concave shape and growth rate having a convex shape. Because of these two shapes, nucleation rate has a shallow sensitivity at high values of Ω, as shown by the critical radius data, and a steep sensitivity at low values of Ω, which is the more environmentally relevant portion of the curve. Aragonite growth rate has the opposite sensitivity. Specifically, in the environmentally relevant portion of Ω range from 10-20, if Ω is decreased by 1, nucleation rate will drop by 15.1% while aragonite growth rate will decrease by 12.6%. Figure 2.7 (main figure) is a closer look at the relevant portion of the plot showing the different slopes of the two lines.

Since this data shows that nucleation rates are more sensitive to changes in Ω in the environment than mineral growth rates for the first time, it potentially changes predictions of how coral growth will be affected by an acidifying environment. Because nucleation is the first step in skeletal growth, that step being impacted by changing environmental conditions would presumably have a large relative impact on the rest of the skeleton. As mentioned, coral skeletal growth has two characteristic stages, deposition of nuclei and infilling of the crystals around and on top of those nuclei. If the infilling step stays relatively constant as Ω changes in the oceans, but the

nucleation rate drops more quickly, one possibility is that coral skeletons will remain relatively the same size, but they will be much less dense. Porosity could increase as nucleation decreases, and this in turn could lead to a loss of strength in the skeleton and an increased inability to withstand physical stress.

2.4.2 *Skeletal Growth Model*

Effects of Nucleation on Skeletal Growth Processes

In order to quantitatively answer these questions about how different sensitivities to Ω of nucleation and bulk growth rate affect the overall skeleton, we used the skeletal growth model. One question we sought to answer using the model was: what is the proportionate amount of control that nucleation has on growth parameters, as opposed to bulk mineral growth rates? To answer this question, we calculated the linear extension and calcification rates at different Ω values using the aragonite mineral rate law from (56) alone, and compared those rates to the ones output by the model. Although linear extension and calcification are different processes that are measured differently in corals and in the model, they can be directly compared because they have the same units. This comparison shows that calcification calculated from horizontal growth, calcification calculated from vertical growth, and vertical linear extension rate all have fairly similar values to the growth rates calculated using the mineral rate law as compared to horizontal linear extension (Figure 2.8). Nucleation clearly has the highest impact on horizontal linear extension, which has the highest percent difference from the mineral growth rate calculated result at $\Omega = 15$, the same pattern as that for the ratio of nuclei to total growth in the skeleton. It is apparent that nucleation plays the biggest role at that Ω, with a steep drop in influence as Ω decreases. At $\Omega = 15$, horizontal linear extension rates are 12 times higher than without nucleation, and even at an Ω of 5, horizontal

linear extension is ~4 times greater than without nucleation. Horizontal growth calcification, on the other hand, is about 40% less than the value calculated using mineral growth rates alone on average across the range of Ω values. This implies that nucleation rates can actually slow down calcification during horizontal growth.

Because nucleation is important in controlling horizontal growth processes, it is most important in scenarios when the skeleton is growing laterally on new surfaces. Another way to view this is that nucleation is more important during 2-dimensional growth than the 3-dimensional processes represented by vertical growth. The fact that nucleation can increase growth above that of mineral growth rates could potentially be a very important tool for corals. Having access to a faster mode of growth simply by increasing nucleation could allow corals to decide to grow quickly at certain times where it would be more advantageous to do so.

It is somewhat surprising that nucleation does not appear to be having more of an effect on calcification rates or vertical linear extension rates. However, when measuring the average z height of the growing skeleton in the model, it becomes clear that the average height added to the growing skeleton in steady state with each timestep is much greater than the height of a new nucleus deposited on the surface. When the skeleton starts growing, the average height added across the surface is smaller than an individual nuclei's radius, as most of the surface is not covered. As the surface is populated and starts to grow, the average height added is increased until it hits steady state. The average change in height added each timestep is at least an order of magnitude greater than the radius of a new nucleus added for every Ω value, so any new nuclei deposited do not have a significant impact on overall volume added. The initial nuclei radius length is of critical importance in this determination because if the radius length was larger than the height added each timestep, nucleation would play a much more influential role in calcification and vertical growth

processes. The critical radius length is calculated from our experimental data in Table 2.1 for each Ω value. We tested a range of radius values at different orders of magnitude (Supplementary Figure 2.14), and found that for radius values below 0.5 μm, there was no difference in model output, as these radius values are below the order of magnitude of the addition of growth on the skeleton each timestep. The initial radius used in the model is a radius on the order of the critical radii measured in Table 2.1.

It is worth considering if there are any conditions under which nucleation might become an important factor in calcification and vertical extension. As the radius sensitivity tests would indicate, having large enough nuclei (or conversely, low enough mineral growth rates) would lead to potentially more of a role for nucleation in these processes. One way for mineral growth rates to potentially be low in the vertical direction has to do with the shape of the nuclei and the directions of mineral growth on those nuclei. The model used hemispheres as the shape of initial nuclei, and allowed isotropic mineral growth. We performed a shape sensitivity analysis by using oblate and prolate spheroids, cubes, and rectangular prisms as nuclei shapes, and found that no matter the shape, the increase in height with each timestep in the model was higher than the nucleus radius added. The exceptions were when Ω was low (~5). However, in these scenarios, nucleation rates are also so low that overall calcification is still controlled by mineral growth rates.

There is evidence that mineral growth of calcite is affected by amino acids and short polypeptides, which act as modifiers of crystal shape and inhibit calcite growth above a certain concentration (40, 67). If organic matrix proteins act similarly to these amino acids and polypeptides, or if there was anisotropic mineral growth of the nuclei for another reason, there could be a scenario in which nucleation becomes an important factor in calcification and vertical growth. If we assume spherical nuclei and isotropic growth are realistic representations of

nucleation and mineral growth in coral, then the model indicates that in skeleton built using inorganic kinetics alone, nucleation plays little role in calcification and vertical extension.

Optimal Ω for Coral Growth

Another particularly interesting model result is how, for both horizontal and vertical growth, the ratio of nuclei to overall growth, and the nuclei density on a flat surface and total volume when the horizontal surface is covered, all have maxima or minima at $\Omega = 15$. This value is very relevant to the actual processes occurring in coral skeletons because it falls directly in the range of Ωs measured and predicted to be in the coral calcifying space. The density on a flat surface (Figure 2.4D) is representative of the balance between nucleation and mineral growth rate, and the highest density of nuclei in a given area falls at Ωs of 15. At higher Ωs, many nuclei are deposited, but the mineral growth rate is fast enough that those deposited nuclei grow quickly to fill the space, while at lower Ωs, nucleation rates drop off so quickly that mineral growth takes over completely. The ratio of nuclei to total growth (Figure 2.4C and Figure 2.5C) follows the same pattern as nuclei surface density over the range of Ω values, and indeed, the two parameters are highly correlated ($R^2 = 0.97$, $p << 0.01$), as are the horizontal and vertical nuclei to volume ratios ($R^2 = 0.99$, $p<<0.01$) . This indicates that nuclei surface density can be used as a proxy for overall nuclei density in the skeleton. Because total volume at 90% surface coverage has a minimum at $\Omega = 15$. as well, this means that the coral has to grow the least amount to cover the same amount of space as at other Ω values, which could be advantageous for the organism.

The peak in nuclei density occurs at the same Ω value as the peak in the percent increase in horizontal extension as compared to mineral growth rates (Supplemental Figure). The fact that the maxima occur at the same Ω value of 15 and the two curves have similar shapes indicates that the

nucleation density is related to the increase in horizontal extension rates as compared to mineral growth rates, and may even be the cause of this increase. Based on this data, we predict that as nucleation density increases, there should be a related increase in horizontal extension in corals, for the values of Ω that are found in the coral calcifying space.

The fact that available data suggest corals in the modern ocean control their calcifying spaces to ensure an Ω close to 15, and therefore to maximize nucleation density and percent increase in horizontal extension, and minimize total growth, could indicate that corals evolved to optimize these parameters. Calcification and linear extension have more straightforward responses to changes in Ω values (as Ω values increase, so do these rates), and it would seem most simply as though it would make sense for corals to have the highest calcifying fluid Ω value achievable to increase calcification and linear extension as much as possible. However, viewed in the context of efficiency of growth, from a kinetics perspective, this data points to Ω values around 15 as possibly being the most advantageous for corals growing their skeletons in order to optimize certain parameters and expend less energy than they would to attain higher internal Ω values.

Comparison to Live Coral Growth

How does this new model of nucleation and overall growth fit into our previous knowledge about how coral skeletons grow? It is clear that in the model, horizontal and vertical calculations of different parameters represent fundamentally different processes, as well as non-steady state versus steady state growth, respectively. The patterns of horizontal and vertical growth over the range of Ω values investigated were the same for both states, but the magnitudes were different. One interpretation is that these different calculations are directly analogous to the equivalent growth in the coral, i.e. horizontal growth emulates coral lateral growth as the organism fends for

space and grows over new surfaces, while vertical growth presumably occurs once the skeleton is removed from the influence of the surface and is creating the mass of the skeleton. Nucleation would primarily play a larger role in scenarios where competition for space is important, perhaps, for example, during the settling of juveniles. Corals that are trying to expand onto new surfaces extend quickly and could deposit a nuclei rich layer of skeleton to claim territory. Once a new area has been colonized, the skeleton as a whole extends more slowly as mineral growth rates take over.

The work from this model is based purely on inorganic rates of growth, but it is also clear from the long literature on biomineralization that the organic matrix plays a vital role in coral skeletal growth as well. This brings up the question of how accurate the inorganic skeletal growth model can be when trying to predict rates of change in live corals. At the least, the model provides kinetic constraints on possible growth in aragonite skeletons, and might be able to provide insight into how much of skeletal growth processes are controlled by the organic matrix versus kinetics alone. To check how well the model can be used to quantitatively predict changes in coral skeletal processes, the model output was compared to nucleation density and horizontal linear extension from coral samples prepared using the flat growth prep technique (68). In an effort to accurately compare coral growth processes that are on a similar scale, and to be clear that we are comparing the same processes between the model and live corals (i.e. horizontal linear extension in both as opposed to vertical), we compare between two carefully controlled studies that use this growth technique and the model.

In the first study, the nucleation density of an *Acropora* sample grown using the flat growth prep technique measured in coral samples was 0.00362 nuclei/um^2 (Supplementary Figure 2.15). When compared to the model output data (Figure 2.4D, **Error! Reference source not found.**), the two are the same order of magnitude and the actual data from *Acropora* falls within the values

predicted by the model. The model output shows the relationship of each property with Ω, so using this correlation, the Ω of the coral calcifying space can be predicted. If the model data were used to determine the Ω of the calcifying fluid of the *Acropora* in this test case, it would predict an Ω of 5.09, slightly lower than the measured values of 9-15 during the daylight, but close to a realistic value for corals (27).

In the second study, using the flat growth prep technique, linear extension and nuclei density were measured in three *Acropora* samples grown in an aquarium in the Gagnon lab at the University of Washington (69). Nuclei and crystal growth were observed under a microscope and time lapse images of the growing edge of the coral were taken to quantitatively measure the parameters of density and extension. In this study, three modes of growth were observed: laminar, scattered, and mixed. These modes correspond to slow growth with few nuclei, fast growth with many nuclei, and intermediate growth and number of nuclei, respectively. Qualitatively, these results agree with the model prediction that nuclei density is related to linear extension, and at higher nuclei densities, there should be higher extension rates.

The quantitative measurements of densities and extensions also validate the model prediction, as data points from all three coral samples show that an increase in nuclei density is linearly correlated to an increase in horizontal extension (69). Perhaps even more remarkable is the fact that the range of nuclei density values measured in these live coral samples is the exact same range as the nuclei density predictions from the model for Ω values in the coral calcifying space. This gives us high confidence that the model is correctly predicting nuclei density and the relative balance of nucleation and mineral growth rates. Nucleation density is an emergent property of the model, meaning it is not tuned to any input parameter, so it serves as a good test of the model's ability to predict trends in live corals.

Predictions for Future Coral Skeletal Growth

The model comparison with the coral data available in the literature shows that the inorganic model is a reasonable fit for processes involving nucleation occurring in live coral (horizontal linear extension, nuclei to volume ratio, and nuclei ground density), and can therefore be used to make relevant predictions for those processes in coral skeletal growth in the future. Corals today are growing in an ocean with an Ω ranging from 3 to 4. By 2100, Ω is predicted to drop below 4 everywhere in the ocean, and to an average of 2 in the tropics (70). Under the RCP 8.5 projection (business as usual emissions scenario), the Community Earth System Model Biogeochemical predicts a 0.25 to 0.35 decrease in pH values, a -50 to 250 μmol/kg change in DIC, and a 0.85-1.95 decrease in Ω in global ocean reef sites by 2100. If external Ω in the ocean decreases by 1.95, then the internal Ω of the calcifying space is predicted to drop, but the exact relationship between the two is not known. We will conservatively assume a 1:1 relationship between the changes in internal and external Ω of the corals for predictions.

If corals today have an internal Ω value of 12.1 (the value measured in *S. pistillata* in (71)), then using the maximum changes in Ω predicted, horizontal linear extension would decrease by 28%, nuclei to volume ratio would decrease by 15-16.5% during both horizontal and vertical growth, and nuclei ground density would decrease by 16% as well. It is possible corals on average have higher internal Ω values in the modern ocean, of around 20. If that were the case, then by 2100, horizontal linear extension would have only decreased by at most 16%, while nuclei to volume ratio and nuclei ground density would both increase by up to 16%. However, it is also likely that some corals in the modern ocean fall on the lower end of calcifying fluid Ω values measured in (71), of 8.5. If that is the modern calcifying fluid Ω value for corals, then by 2100 they would see decreases of 45% in horizontal linear extension, 50% in nuclei to volume ratio, and

39% in nuclei ground density. As internal Ω values decrease, the relationships between growth parameters and Ω become more precipitous. Because the inorganic model is a good fit for coral growth measured today, these predictions provide realistic benchmarks for how coral certain skeletal growth processes will decrease in an acidifying ocean.

Organic Matrix Effects on Skeletal Growth

Another question that the inorganic model can help to answer is the role of the organic matrix in mineral growth. The possibilities range from full kinetic control of crystallization to a process where proteins arrange ions into position and lower energetic barriers in a tightly coordinated manner. The fully inorganic model in this study matches fairly well with data from live corals regarding processes that involve nucleation, indicating that inorganic kinetic processes play a fundamental role in some aspects of coral skeletal growth. If the model results of nuclear density vastly overshot the values measured in live corals, say by orders of magnitude, it would be likely that another process was a primary control on skeletal growth; instead, the model output data is very close to values measured in live corals.

One example of how local kinetics can control the skeletal growing process comes from the flat growth prep samples that produced, in this study, the nuclei density on a surface measurement in *Acropora* (Supplementary Figure 2.15). In some cases, there were instances of scratches in the glass slides that the corals were grown on. In those cases, the corals consistently nucleated along the scratch, forming straight lines of nuclei in an otherwise random pattern. Although the organic matrix is undoubtedly playing a role in mineralization as a whole, local kinetics overrode the organic matrix effects along the scratches, causing nucleation to occur. It is energetically more favorable to nucleate along a feature that has more surface area, such as a scratch in glass, because

it means less disruptive contact between the nucleus and the solution as the nucleus forms. This example is one way in which kinetics control the skeletal growing process at the level of nucleation, and the model output indicates that kinetic constraints might play a large role in controlling the entire skeletal growing process as well.

The fact that the model results indicate that nucleation rates are most relevant for horizontal extension processes in corals brings up some interesting implications for the role of organic matrices in skeletal growth. It has long been posited that organic matrices play a role in nucleation, particularly by changing interfacial energy, organizing ions to form a nucleus, or in changing local chemistry in order to promote a more favorable micro-environment (32, 35, 40, 42, 72, 73), and if organic matrices can control nucleation in the coral, they can act as a way to increase skeletal growth even under unfavorable conditions. However, if, as the model results indicate, nucleation plays a minimal role in calcification or can even slow down calcification in the coral skeleton, it is unlikely that control over the nucleation process could significantly increase calcification in corals. To test this, the model was run as α in the nucleation rate equation was manipulated to simulate raising and lowering the interfacial energy during nucleation, effectively changing the ratio of nucleation to mineral growth and, respectively, decreasing and increasing the amount of nuclei deposited.

The results show (Figure 2.9) that for Ω values of 10, 15, and 20, horizontal calcification was increased by up to 10% when the interfacial energy was 1.5 times the original value. However, vertical calcification was decreased at each new α value tested, by up to 23%. It is interesting that effectively decreasing nucleation has opposite effects on calcification when measured horizontally or vertically, reinforcing that these two processes are differently controlled. Nucleation rates have a clear effect on horizontal calcification, and some minimal influence, but a less clear control on

vertical calcification. In no case were the calcification values with changes in α significantly higher than the value predicted by the mineral rate law equation, and they were sometimes lower, showing that it is unlikely the organic matrix would increase calcification in corals through control of nucleation rates. Vertical linear extension is slightly increased by changes in α, but not in a systematic way across different Ω values. This result brings up questions about the role that the organic matrix plays in nucleation and skeletal growth as a whole, and the mechanisms of how it interacts with the skeleton.

However, horizontal linear extension can be increased through decreasing the interfacial energy in the nucleation rate equation, which is consistent with horizontal extension being a nucleation-controlled process. The lower the Ω value, the greater the effect of the organic matrix in increasing extension. For Ω = 10, when α is decreased by 25%, horizontal extension more than doubles. At Ω =20, horizontal extension is increased only 60% for the same decrease in α. Given the predicted decreases in horizontal linear extension of up to 50% by 2100, depending on the internal Ω value of the corals, changing the surface energy of growth does have the potential to override these changes in horizontal extension and keep growth relatively the same even as external and internal Ω values decrease. The fact that there is a clear mechanism for how the organic matrix could systematically affect horizontal linear extension, and not the other growth parameters, is perhaps an argument in favor of the idea that horizontal linear extension, or 2D growth, is occurring throughout the skeleton, as it would fit with experiments showing the effects of the organic matrix on growth.

2.5 CONCLUSION

This study measured the first rates of inorganic aragonite nucleation on glass and the sensitivity of nucleation rates to changes in supersaturation. Comparison of sensitivities of nucleation rates to inorganic aragonite growth rates for the first time revealed that nucleation is more sensitive to environmentally relevant supersaturations than bulk growth, and this has repercussions for predicting growth of the overall skeleton and the sensitivity of certain growth parameters. Our inorganic model that combines these two rates was able to distinguish certain processes that nucleation plays a key role in, namely horizontal linear extension, and others that were seemingly not influenced by nucleation, like calcification. The model is useful for examining processes that are hard to measure in live corals, including the ratio between nuclei and mineral growth in the skeleton and the way that the ratio between these two processes can change overall growth. Experiments with live coral validated the relationship seen in the model between horizontal extension and nucleation density, as well as the specific range of density values predicted by the model. These model results can be used to make predictions about coral growth in the future and establish relationships between nucleation and internal Ω values that could then be applied to paleo records of coral skeletons, for instance. The model is also useful for providing another constraint on internal Ω values in corals. However, these results also bring up more questions about how nucleation and horizontal versus vertical growth fit into the skeleton as a whole, and along with that, the mechanism of how the organic matrix can affect skeletal growth through nucleation, since there is a clear mechanism for influencing horizontal growth, but not calcification.

2.6 ACKNOWLEDGEMENTS

The authors acknowledge D. Anderson for his work in developing methods for flow cell experiments and making preliminary measurements of nucleation rates; S. Bergstrom and K. Hall for lab assistance.

2.7 TABLES

Table 2.1. Critical Radii Over a Range of Ω Values

Ω	Critical Radius (nm)	Critical Number of Molecules
5	0.4256891	1.87605E+18
10	0.29754391	1.3113E+18
15	0.2529939	1.11497E+18
20	0.22869873	1.00789E+18
25	0.21284455	9.38024E+17
30	0.20560568	9.06122E+17
40	0.20560568	9.06122E+17
50	0.20560568	9.06122E+17
60	0.20560568	9.06122E+17
70	0.20560568	9.06122E+17
80	0.20560568	9.06122E+17
90	0.20560568	9.06122E+17
100	0.20560568	9.06122E+17

2.8 FIGURES

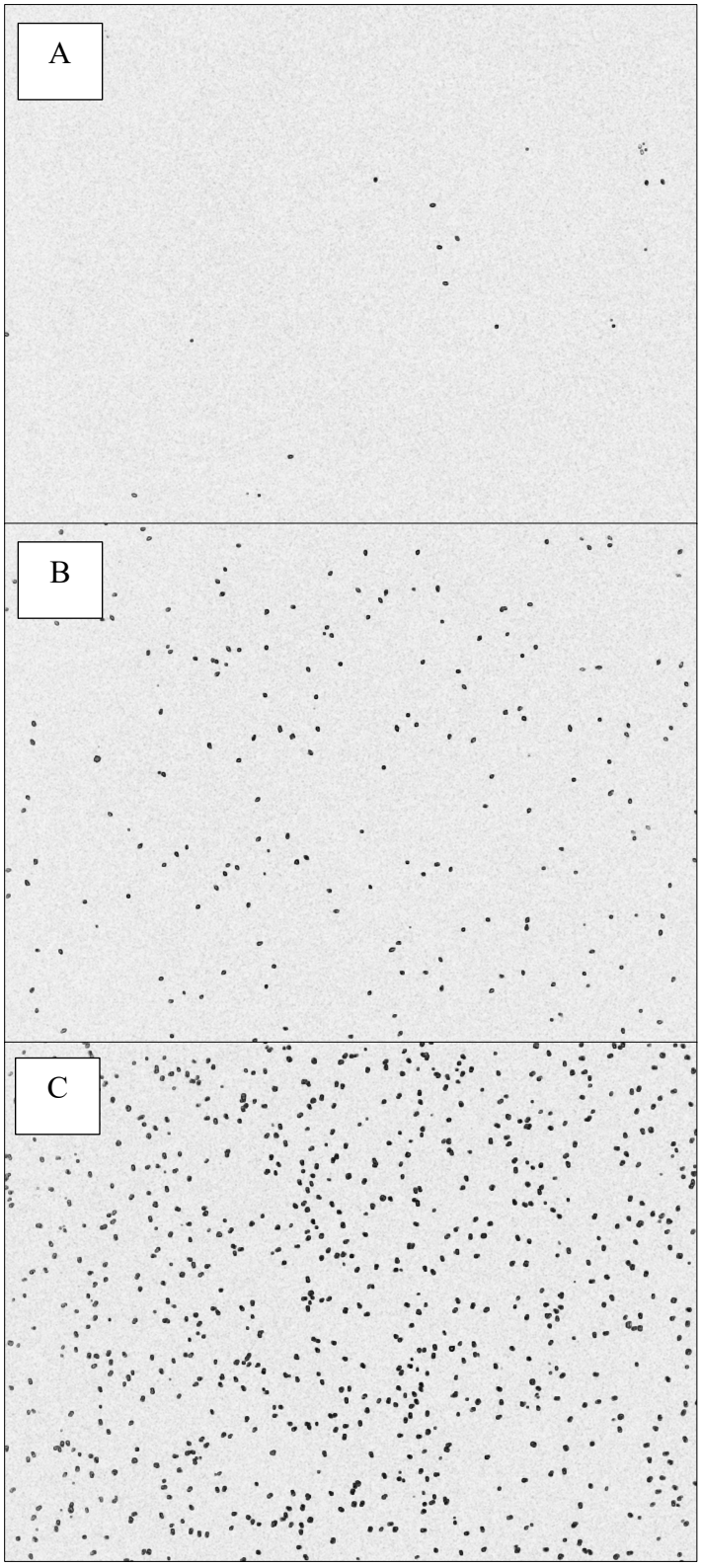

Figure 2.1. Nucleation on the top glass slide of the flow cell under polarized light microscopy. (A) is from an experiment with an Ω value of 7.8, timepoint of 136.5 minutes, (B) is from an experiment with an Ω value of 15.2, timepoint 60.5 minutes, and (C) is from an experiment with an Ω value of 106.4, timepoint of 37.5 minutes. The dark spots are nuclei. Images have been converted to grayscale and background subtracted. These images show that inorganic aragonite nucleation is sensitive to Ω.

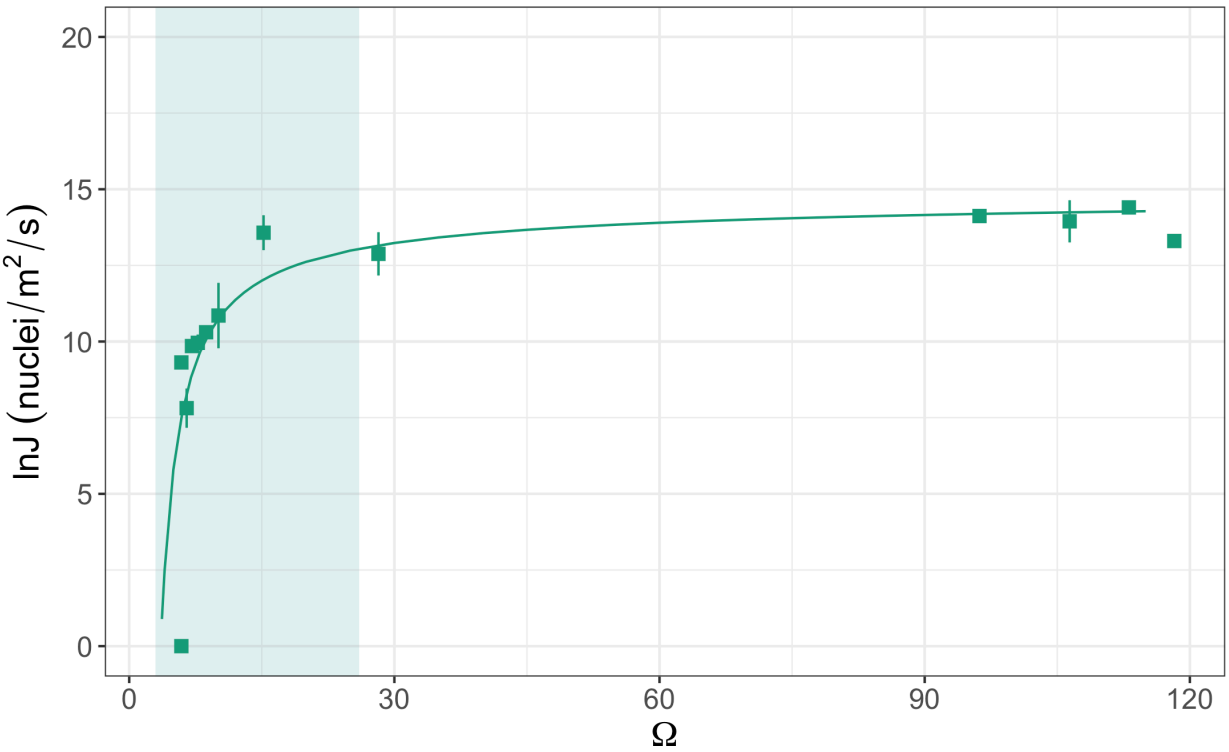

Figure 2.2. Measured inorganic aragonite nucleation rate over a range of Ω values. The fit is taken from the linear regression from Figure 6. The blue box indicates the range of Ω values that have been measured in the coral calcifying space.

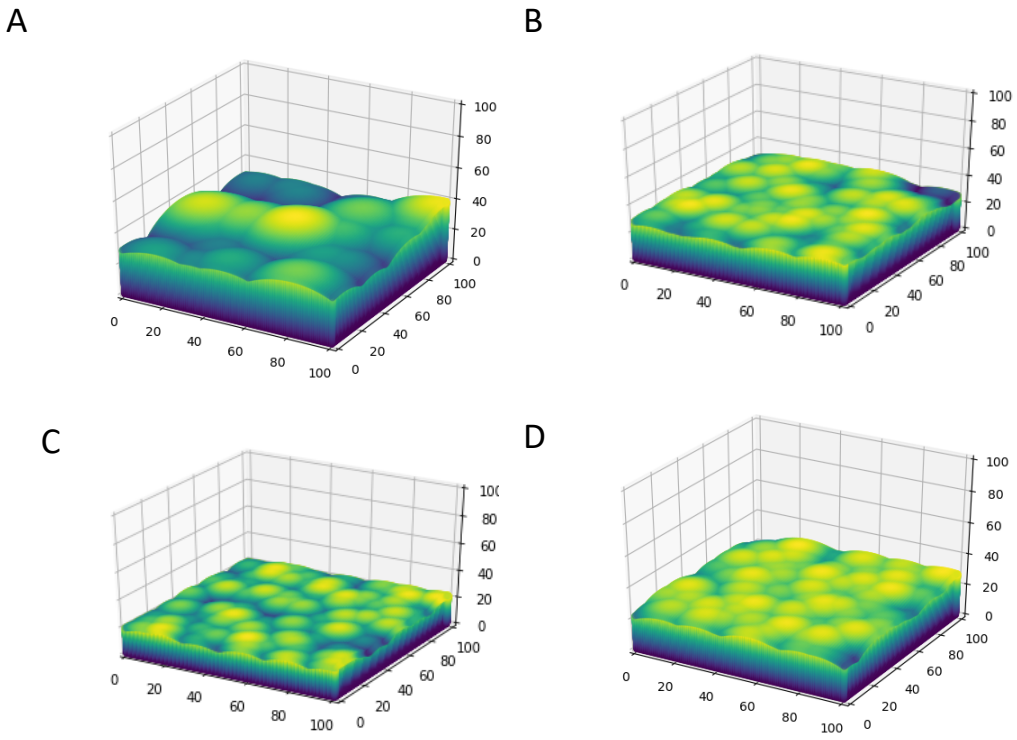

Figure 2.3. Model output from steady state vertical growth at Ω values of (A) 5, (B) 10, (C.) 15, and (D) 20. Ω changes the relative rates of nucleation and mineral growth, causing an overall textural change of the skeleton.

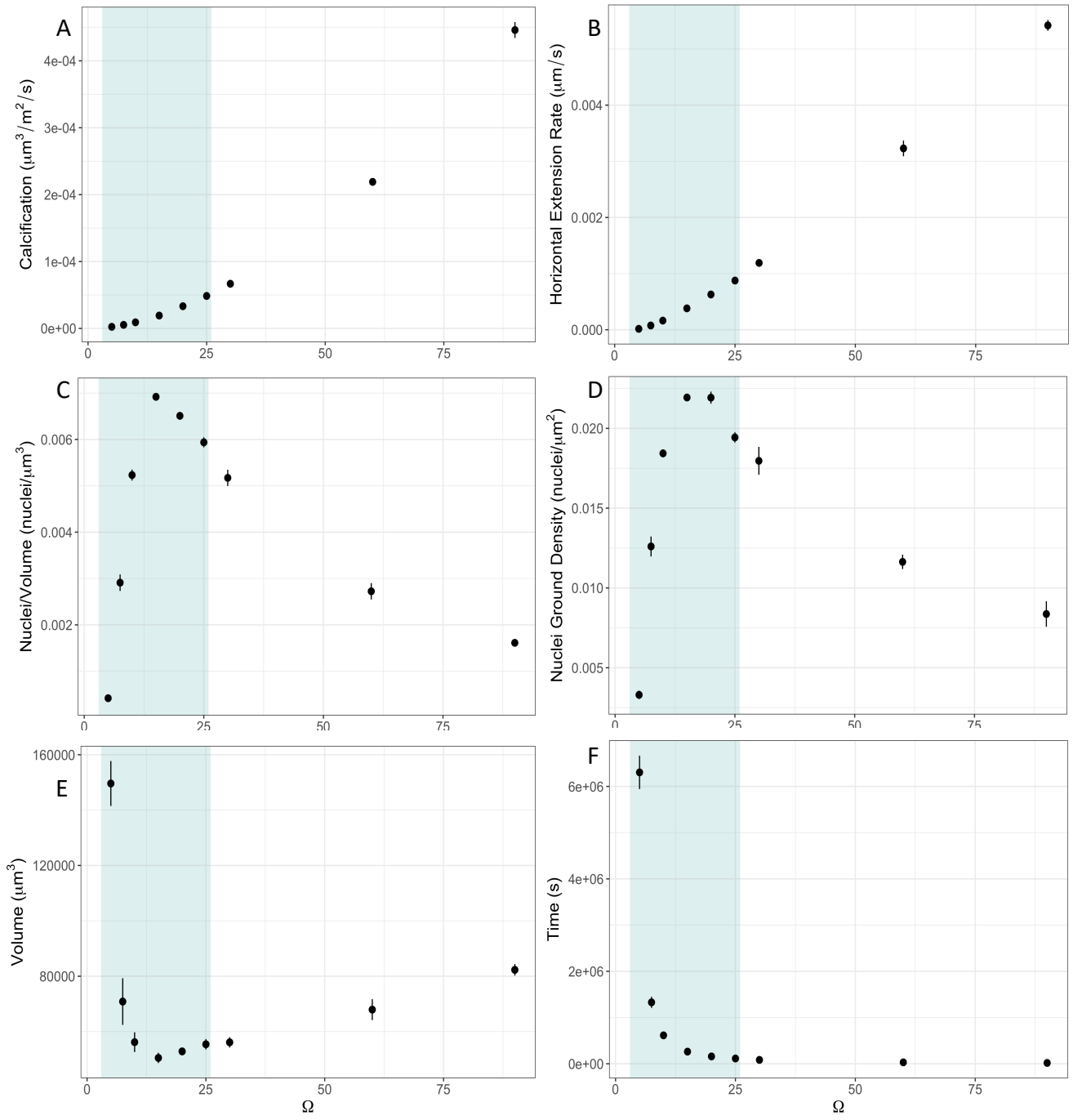

Figure 2.4. Model output when 90% of the surface is covered by calcium carbonate. Each data point is the average of three model runs, and the error bars are two times the standard deviation of the three runs. The blue shaded region is the range of Ω values that are relevant to the coral calcifying space. (A) Calcification rate is total growth, while (B) is the horizontal extension, a measurement of growth across a surface. (C) Nuclei/Volume ratio is the nucleation density in the 3D structure while (D) Nuclei Ground Density is the density in the 2D extension. The peak

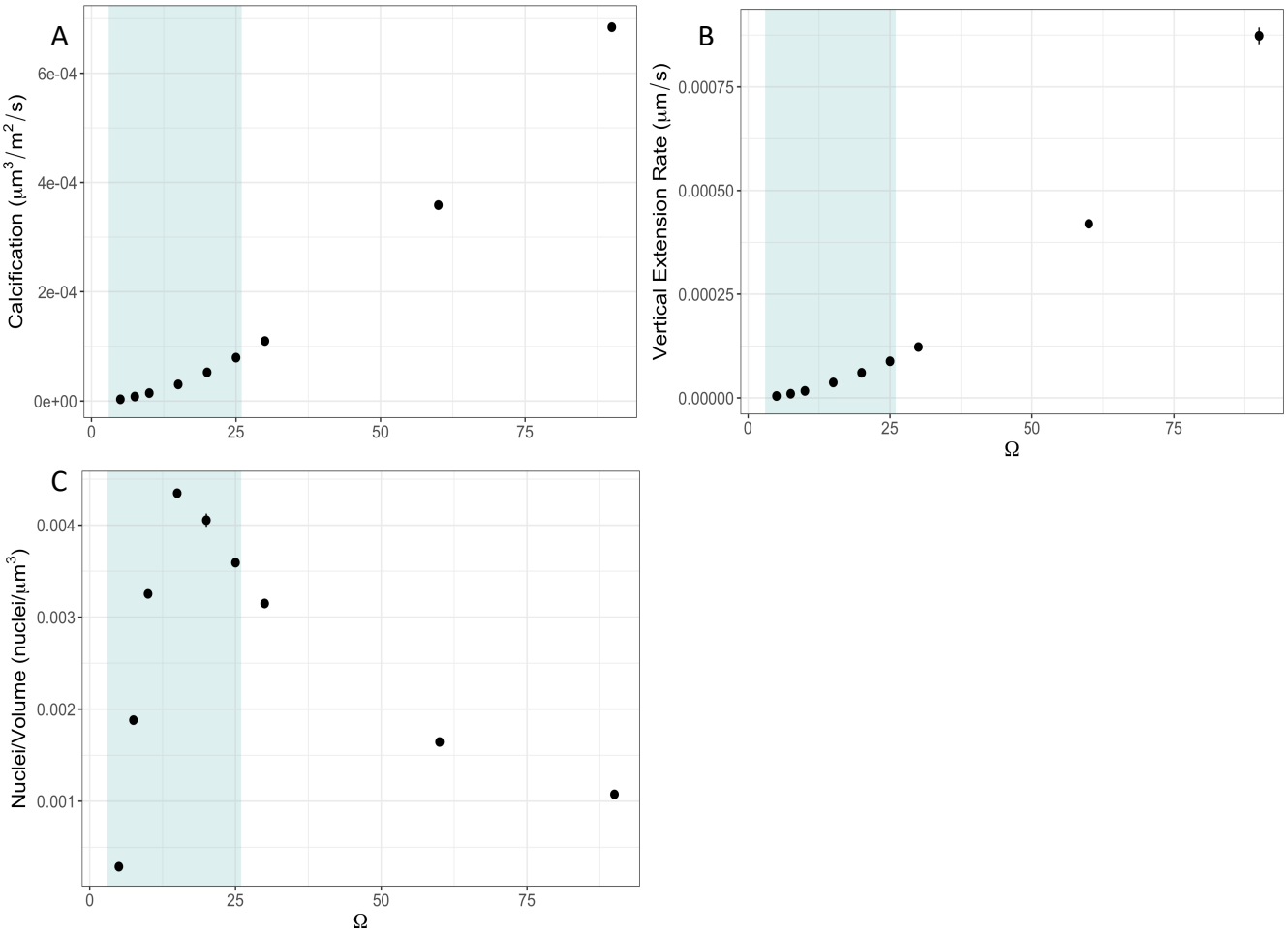

Figure 2.5. Model output when growth is in steady state. Each data point is the average of three model runs, and the error bars are 2 times the standard deviation of the three runs. (A) Calcification rate is total growth, while (B) is vertical extension, the growth in the vertical direction only. (C) Nuclei/Volume is the nuclei density in the 3D structure. The blue shaded area is the region of Ω values that are relevant to the calcifying space in corals.

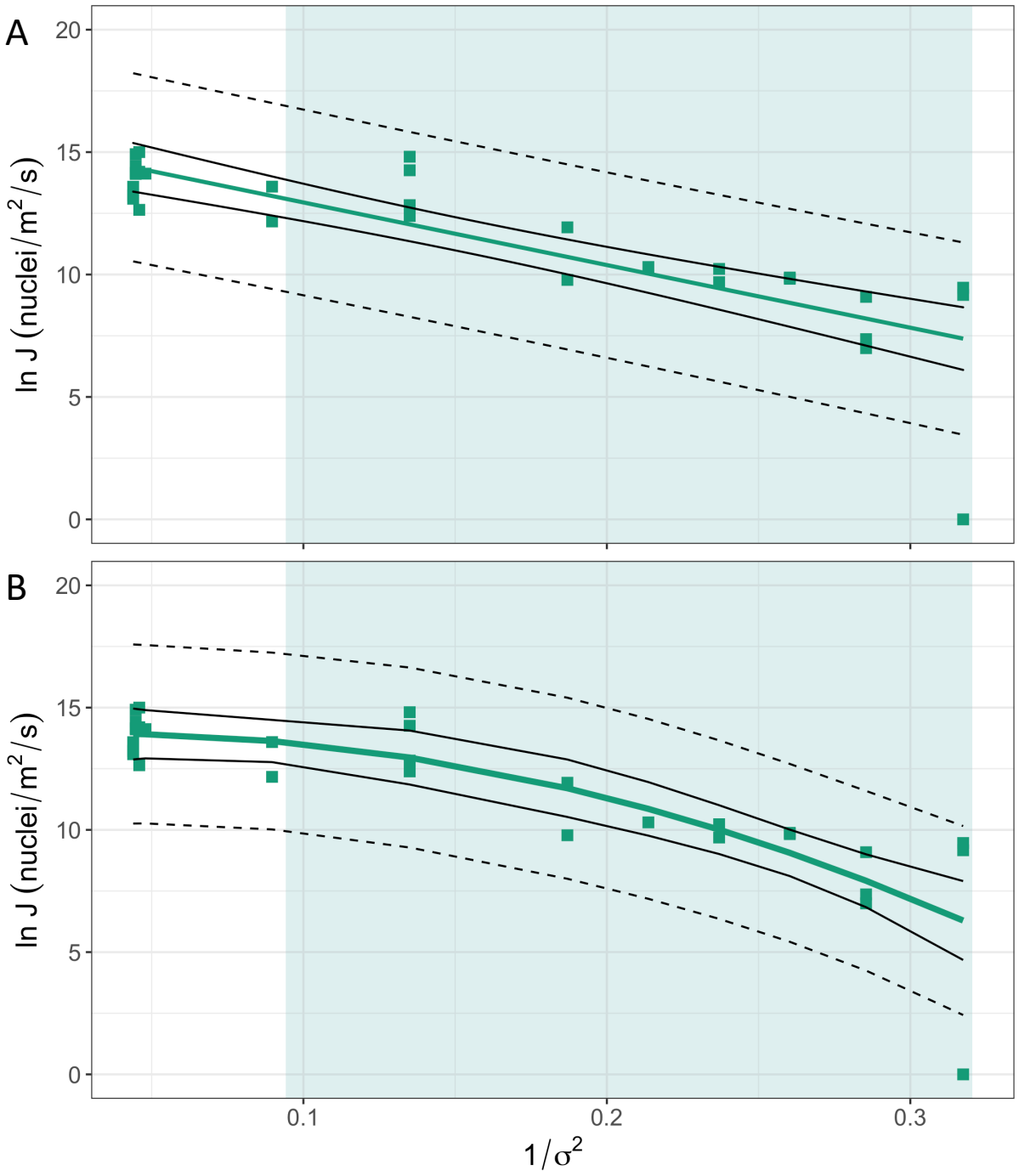

Figure 2.6. Model fit of log-log transformed plot of inorganic aragonite nucleation rates over a range of $(1/(\ln\Omega)^2)$ values with a linear regression (R^2=0.63, p-value << 0.001) and quadratic fit (R^2=0.71, p-value<<0.001). The 95% confidence interval around the line and the 95% prediction interval around the data points are added. The shaded blue area indicates the region of Ω values that are relevant to the calcifying space in corals.

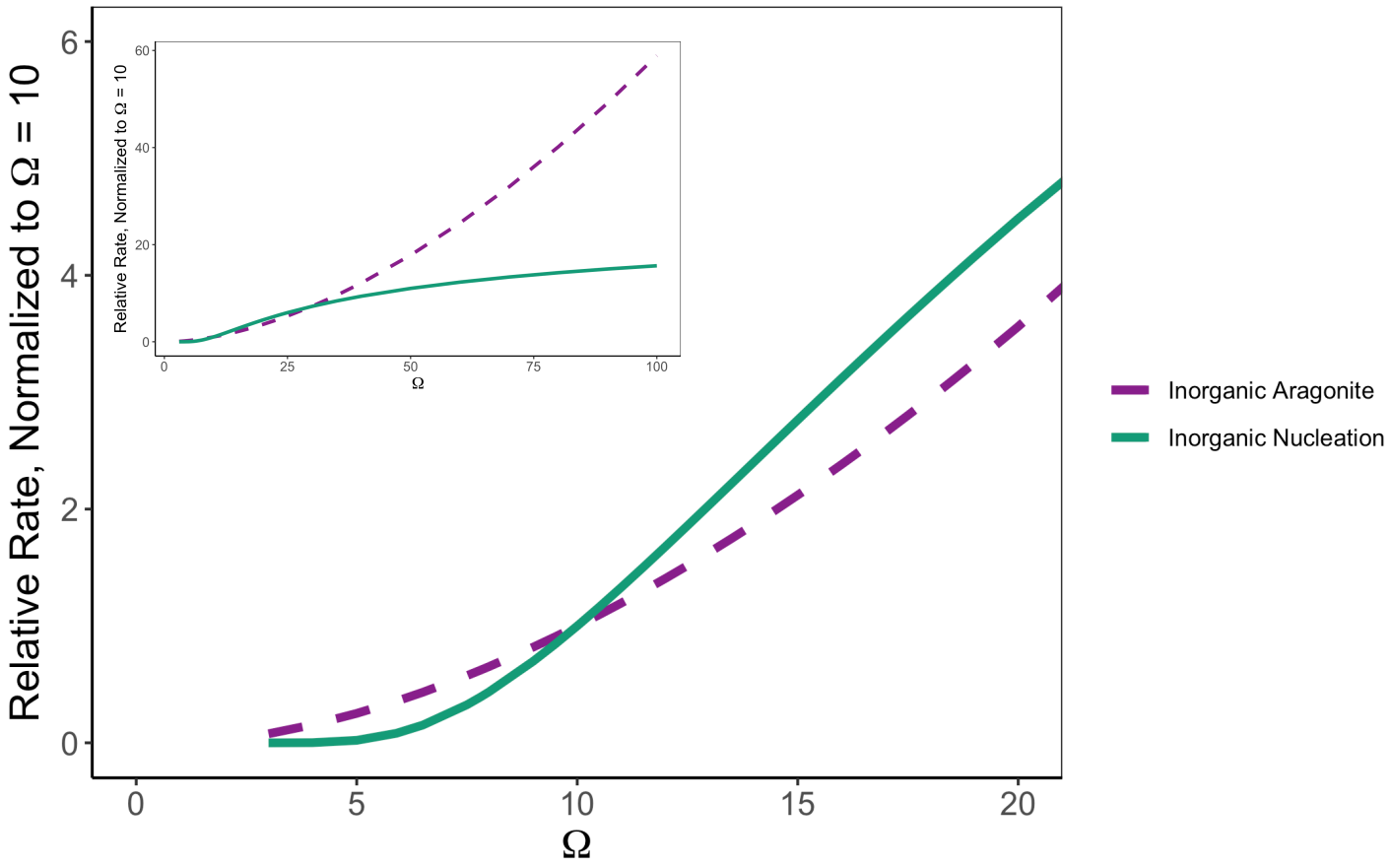

Figure 2.7. Inorganic nucleation rates from this study (solid green line) and inorganic aragonite growth rates from (56) (dashed purple line) are both normalized to their respective rates at an Ω value of 10 to be able to compare the rates to each other. The value of 10 as the normalization point was chosen because it is an Ω value relevant to the Ω in the calcifying space in corals. As Ω increases or decreases from 10, the nucleation rate of change is steeper than the mineral growth rate of change. The inset plot is the full range of Ω values and the main plot is zoomed in on the environmentally relevant portion of the plot.

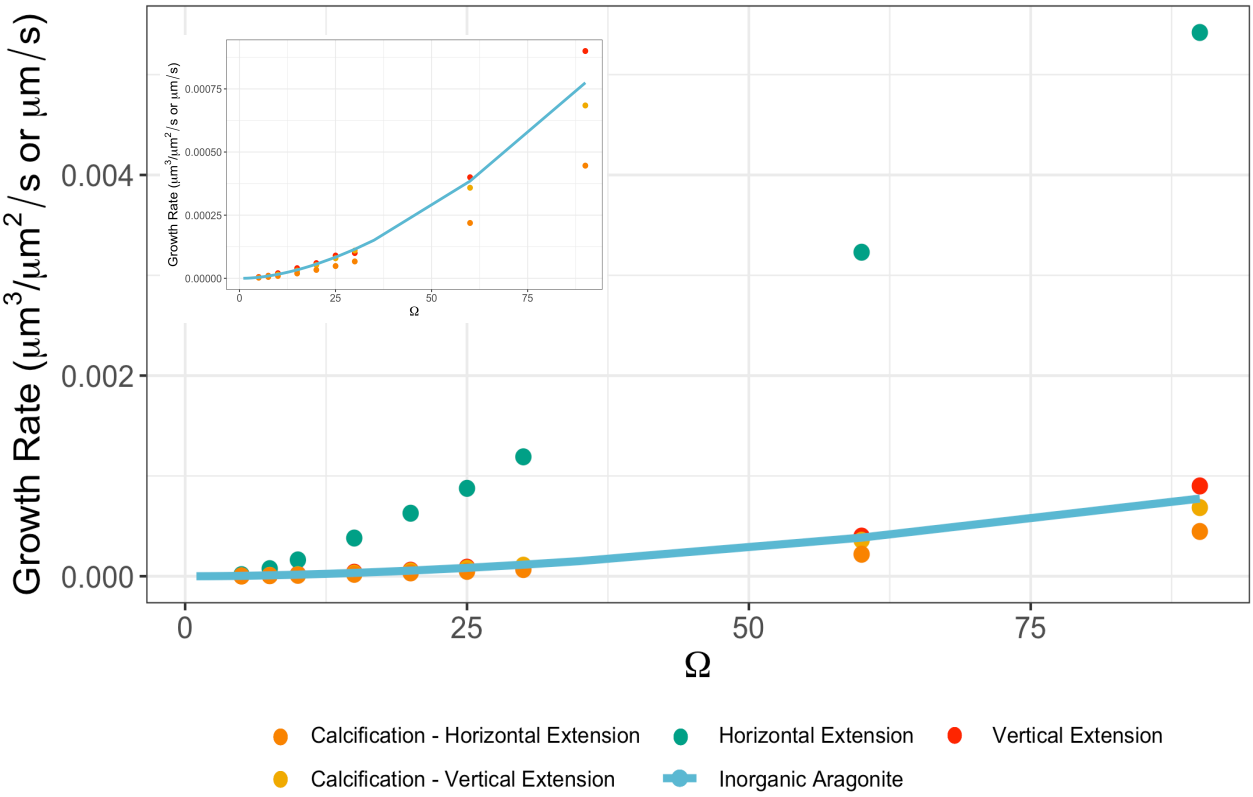

Figure 2.8. The calcification and linear extension rates compared to inorganic mineral growth rate, calculated from (56). Calcification rates were calculated at the time when the surface was 90% covered as well as when the growth was in vertical steady state. All growth rates are measured in either $\mu m^3/\mu m^2/s$ or $\mu m/s$, which are equivalent. Both calcification rates and vertical extension are very similar to inorganic mineral growth (inset is zoomed in to show these rates), while horizontal extension is clearly higher across all Ω values.

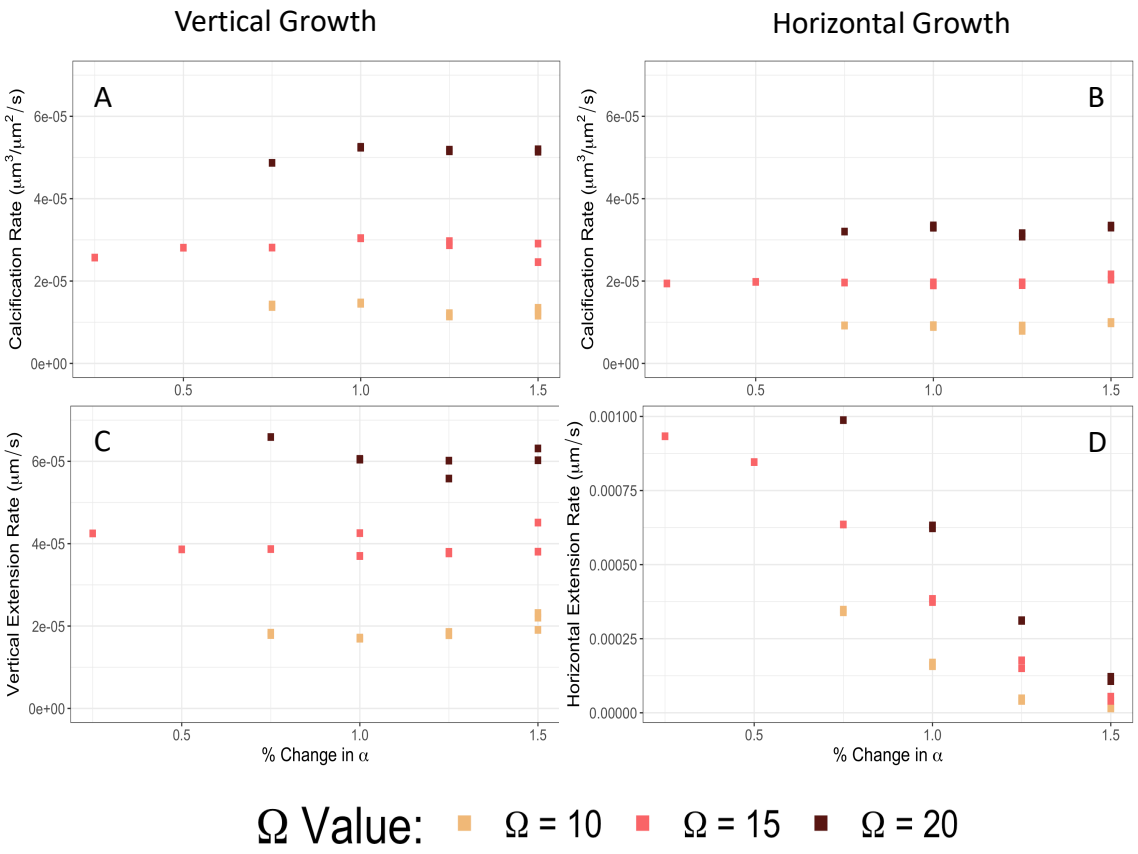

Figure 2.9. Changes in calcification and linear extension rates for three different Ω values as the ratio of nucleation rate to mineral growth rate is changed by changed the parameter α, the interfacial energy. (A) and (C) are measures of vertical growth in steady state and (B) and (D) are horizontal growth. Only horizontal extension (D) shows significant change in growth with changes in α. Note the different y-axis scale on (D).

2.9 SUPPLEMENTAL TABLES

Table 2.2. Inorganic Experiment Solution Chemistry

Omega	Ionic Strength	DIC (mol/kg)	Alkalinity	pH	[NaCl] (mol/kg)	[NaHCO3] (mol/kg)	[NaOH] (mol/kg)	[CaCl2·2H2O] (mol/kg)	[MgCl2·6H2O] (mol/kg)
118.24	0.6748	0.008	0.0159	10.425	0.569	0.008	0.00790	0.01	0.02
113.1	0.6743	0.008	0.0154	10.1225	0.569	0.008	0.00744	0.01	0.02
106.37	0.6739	0.008	0.0149	9.8845	0.569	0.008	0.00695	0.01	0.02
96.2	0.6732	0.008	0.0143	9.6417	0.569	0.008	0.00626	0.01	0.02
28.16	0.6687	0.008	0.00981	8.57	0.569	0.008	0.00181	0.01	0.02
15.25	0.6679	0.008	0.00895	8.25	0.569	0.008	0.000948	0.01	0.02
10.05	0.6675	0.008	0.00859	8.05	0.569	0.008	0.000586	0.01	0.02
8.76	0.6674	0.008	0.00849	7.986	0.569	0.008	0.000491	0.01	0.02
7.76	0.6673	0.008	0.00841	7.93	0.569	0.008	0.000415	0.01	0.02
7.11	0.6673	0.008	0.00836	7.89	0.569	0.008	0.000364	0.01	0.02
6.51	0.6672	0.008	0.00832	7.85	0.569	0.008	0.000315	0.01	0.02
5.89	0.6672	0.008	0.00826	7.805	0.569	0.008	0.000263	0.01	0.02
5.51	0.6671	0.008	0.00823	7.775	0.569	0.008	0.000230	0.01	0.02

Table 2.3. Maximum Change in Ω during Inorganic Experiments

Prescribed Ω	Ω after Maximum Nucleation and Aragonite Growth
106.37	101.82
28.16	27.69
15.25	14.98
10.05	9.98
8.76	8.69
7.76	7.72
7.11	7.07
6.5	6.48
5.89	5.93

Table 2.4. Inorganic Model Output Parameters for Horizontal Growth. This table is provided in a separate XLSX file.

Table 2.5. Inorganic Model Output Parameters for Vertical Growth. This table is provided in a separate XLSX file.

2.10 SUPPLEMENTAL FIGURES

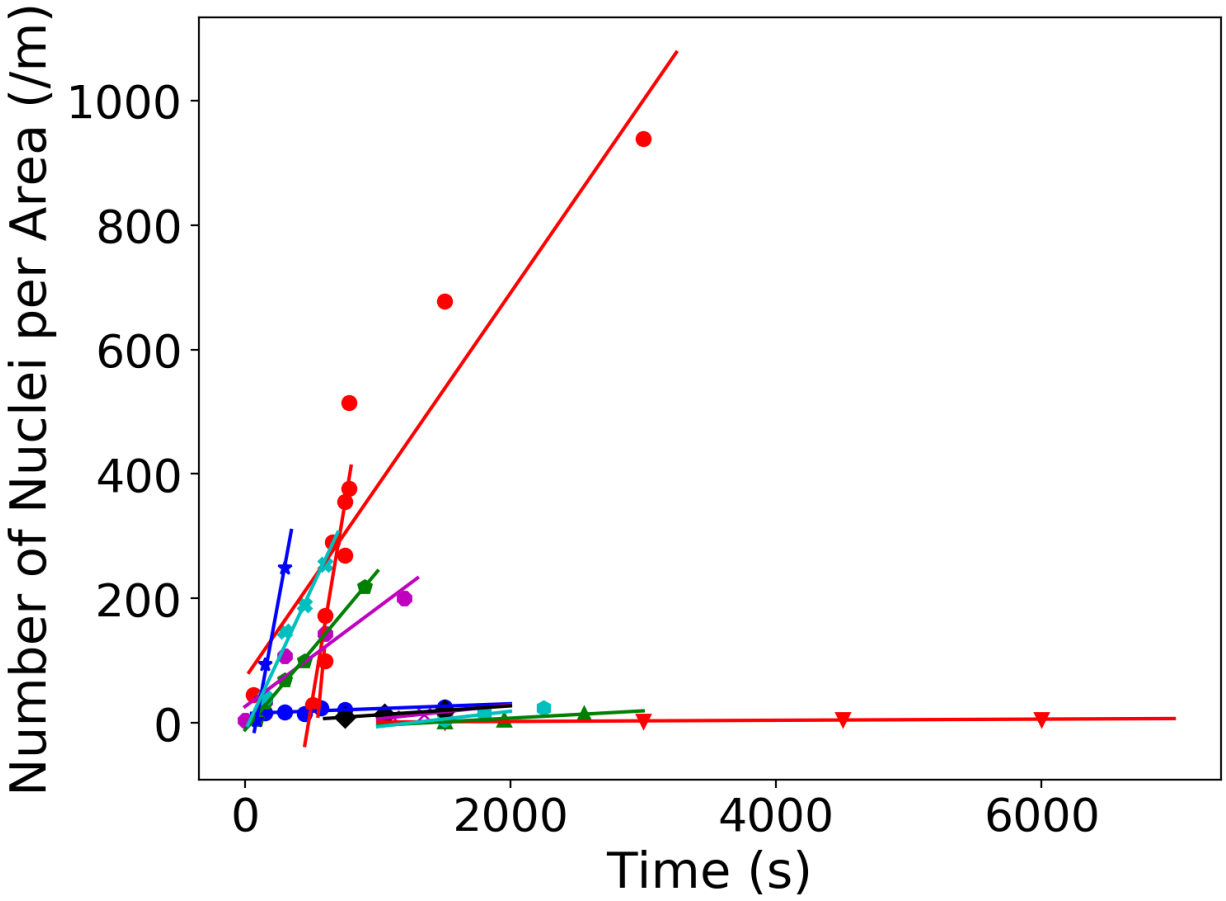

Figure 2.10. Nucleation rates at Ω values ranging from 5.9 to 118. Rates were in steady state and linear during the beginning of each experiment, and then leveled off (not shown).

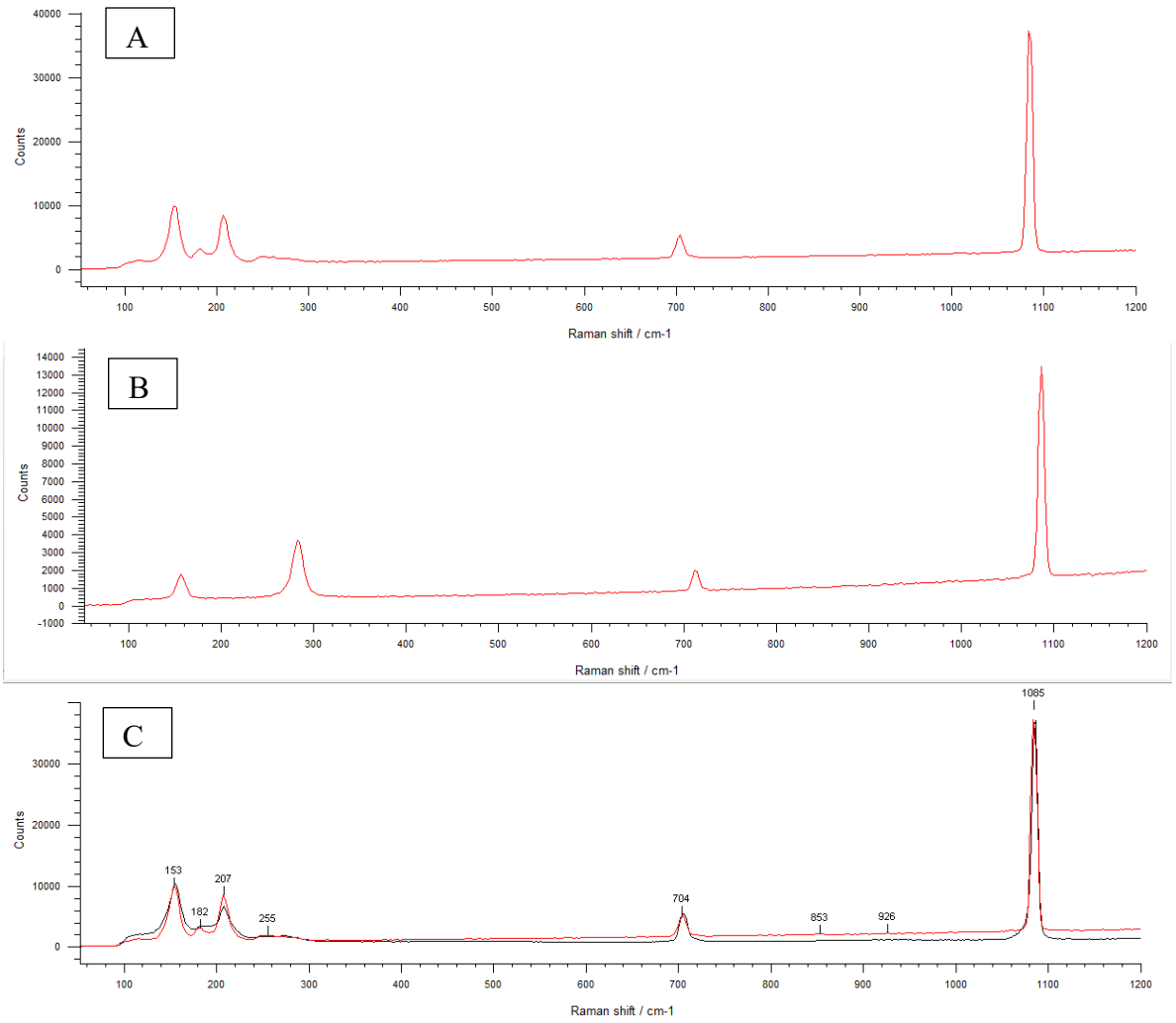

Figure 2.11. Raman spectra of (A) an aragonite standard and (B) a calcite standard. (C) shows both a spectrum from a nucleation experiment (from Ω=91.2 experiment) and the aragonite standard, representative of nucleation in all experiments.

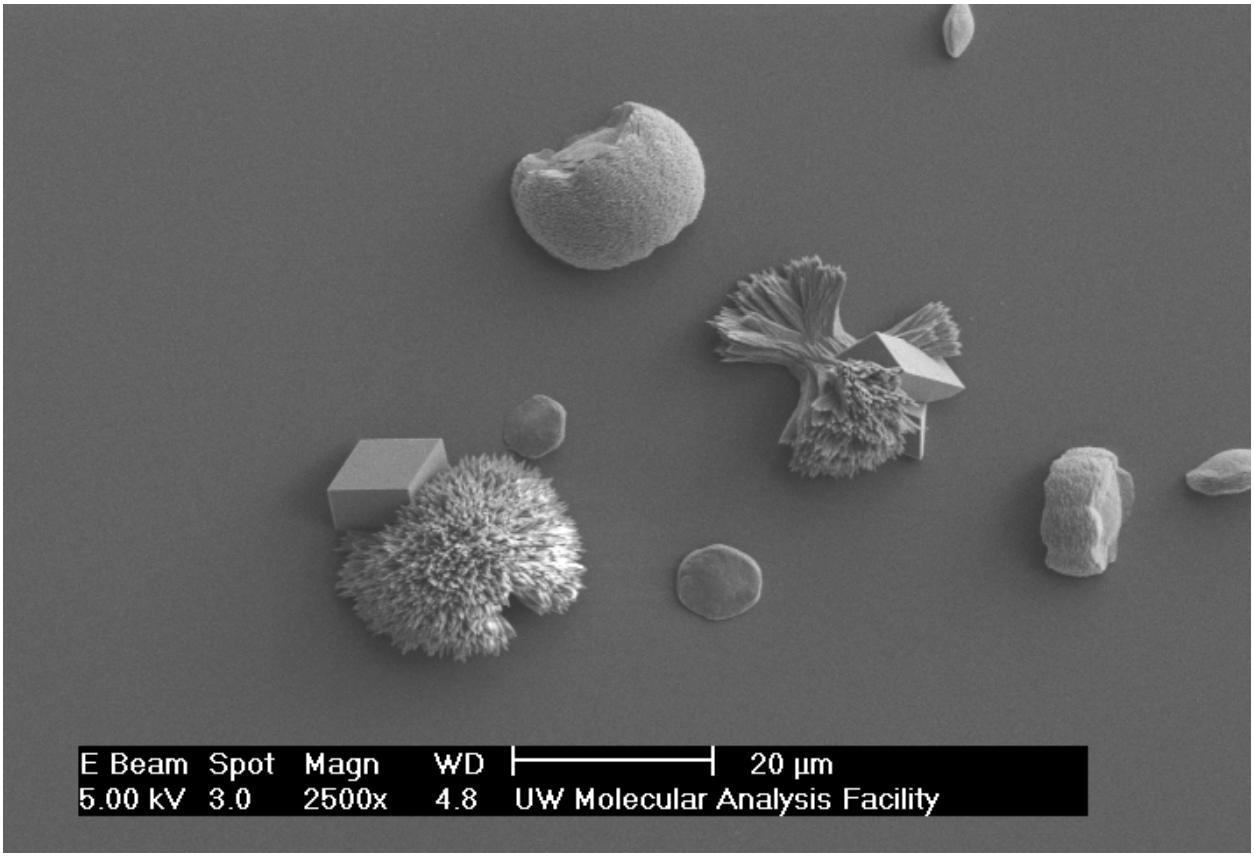

Figure 2.12. SEM image of nuclei on a glass slide, showing an example of aragonite, calcite, and vaterite nuclei in an early experiment in which all three formed. For the experiments done in this study, primarily aragonite nuclei formed on the glass slides.

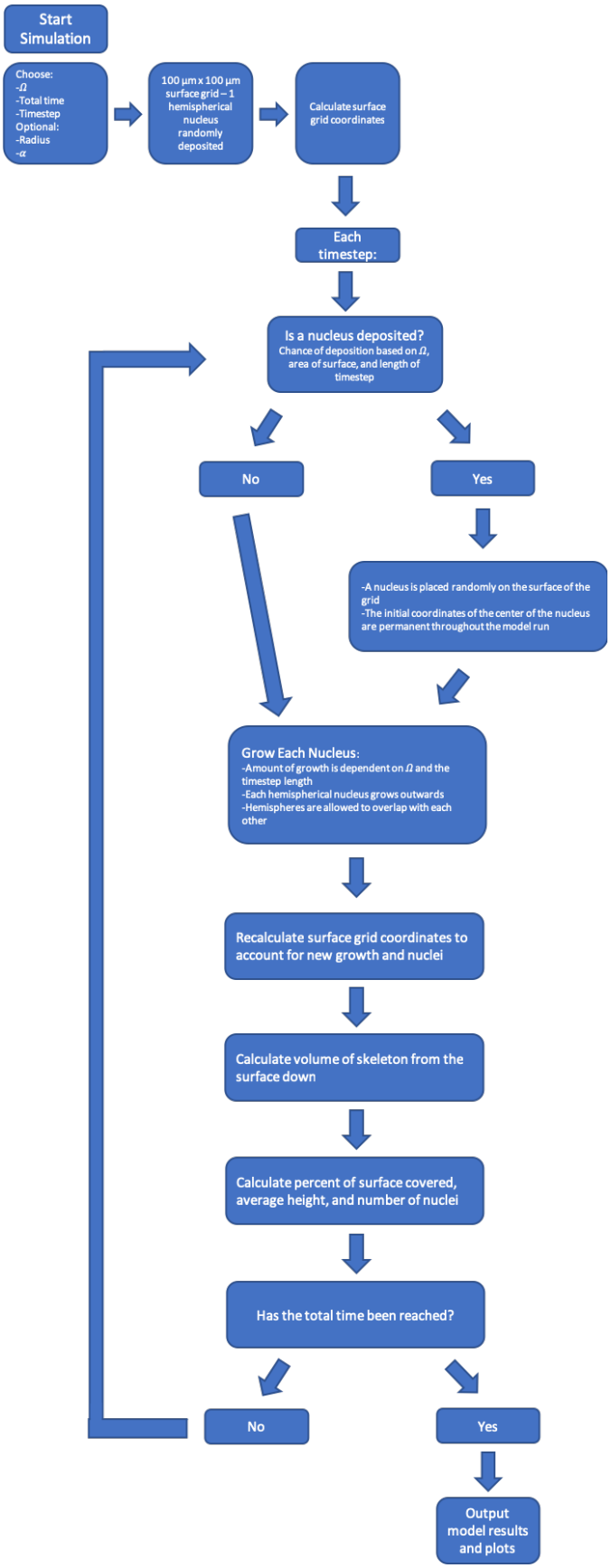

Figure 2.13. A flow chart of the steps taken in the inorganic nucleation model.

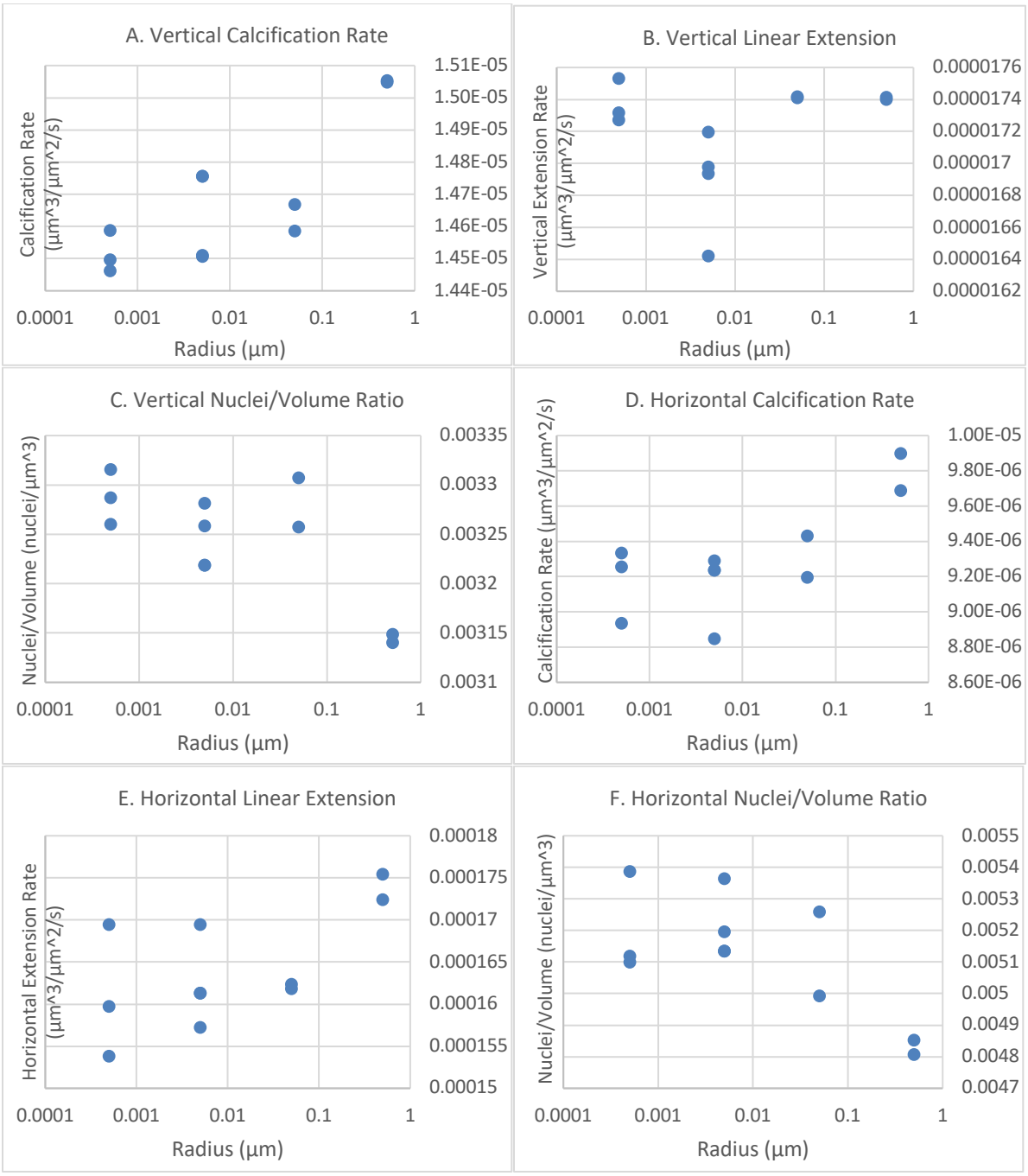

Figure 2.14. The effects of radius on calcification and linear extension rates at $\Omega = 10$. When the radius reaches 0.5 µm, the calcification rates and nuclei density in both horizontal and vertical growth processes are significantly different than at any other smaller radii value.

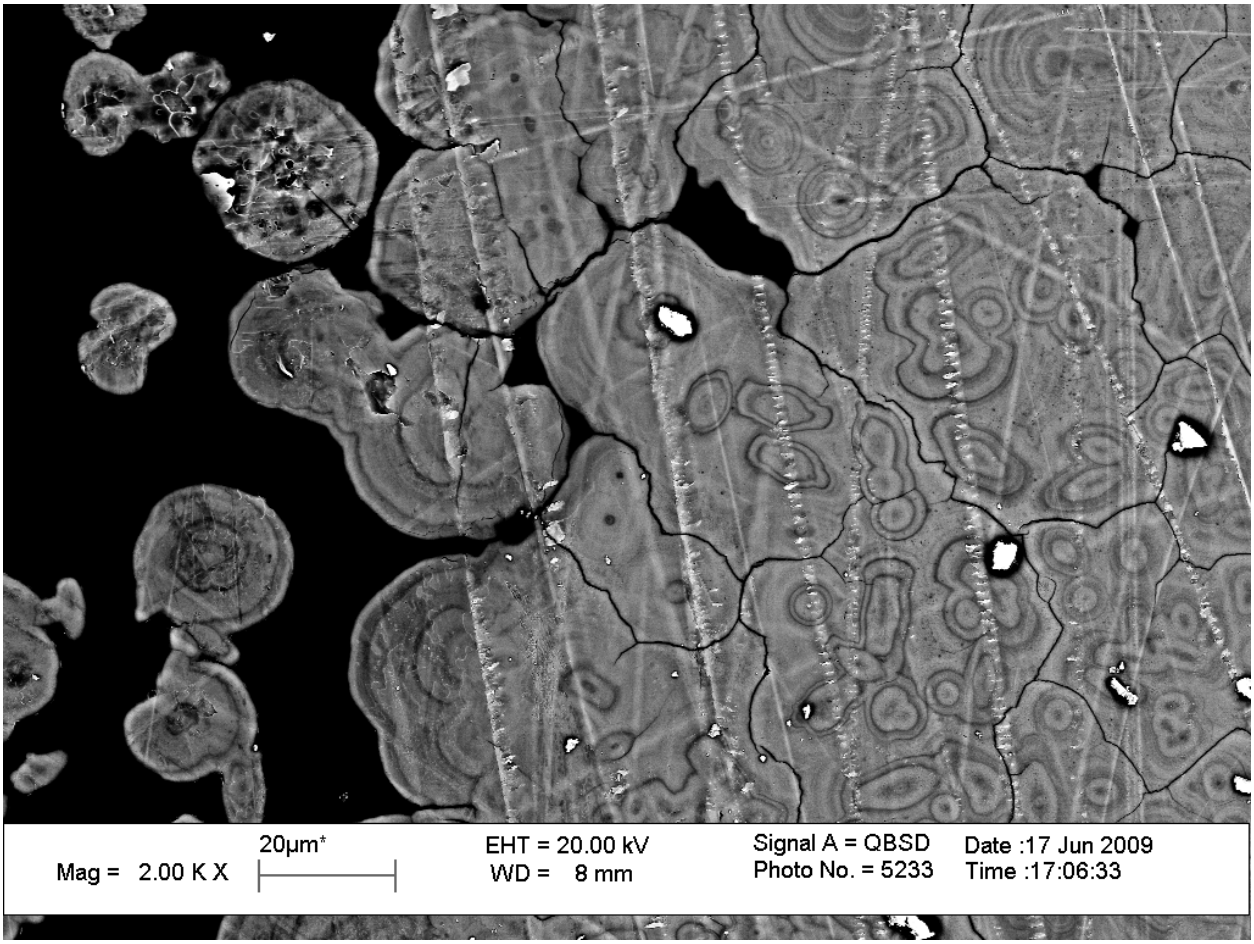

Figure 2.15. Acropora sample grown using the flat growth prep technique. The number of nuclei was determined by counting the nucleation cites, which were determined to be the centers of areas of concentric rings. The nucleation density of this sample falls within the range of values predicted by the inorganic model.

2.11 SUPPLEMENTAL CALCULATIONS

2.11.1 *Calculation of Possible Changes in Ω in the Flow Cell*

Example calculation at Ω = 106.4, showing the largest change in Ω that would occur in the flow cell during a nucleation experiment.

Residence time in flow cell (t): 3.51 sec
Volume in flow cell (v_{fc}): 2.339E-7 m^3
Area of each glass slide available for nucleation (a): 0.0006021 m^2
Highest nucleation rate measured (at Ω = 106.37) (J): ~1,300,000 nuclei/m^2/s
Critical radius of nuclei (r*) forming at Ω = 106.37: 2.05606E-4 µm
Volume of a sphere = $\frac{4}{3}\pi r^3$
Unit cell of aragonite volume (v_{uc}) = 2.2691E-22 μm^3 (mindat.org)
Number of $CaCO_3$ molecules per unit cell = 4
Avogadro's number (N_A) = 6.022E23 mol^{-1}
Initial Ca^{2+} concentration (I_{Ca}): 0.01 mol/kg
Initial CO_3^{2-} concentration (I_{CO3}): 0.006927 mol/kg
Density of seawater (d_{sw}): ~1030 kg/m^3
k_{sp} = 6.46E-7
Equation for aragonite growth rate (R, mol/m^2/h) from (56): $R = k(\Omega - 1)^n$
k (rate constant obtained empirically, from (56)) = 2.344E-5
n (obtained empirically, from (56))= 1.6

Change in Ω due to nucleation

1. Number of nuclei forming on top and bottom glass slide (N) during the residence time of the solution:
N = a*J*t*2
N = (0.0006021 m^2)*(1,300,000 nuclei/m^2/s)*(3.51 s)*2 = 5494.764 nuclei

2. Volume of each nuclei (v_n) formed during that time, assuming nuclei form semi-spherically on a surface:

$v_n = \frac{4}{3}\pi r^{*3} * \frac{1}{2}$
$v_n = \frac{4}{3}\pi *(2.05606E\text{-}4)^3 * \frac{1}{2}$ = 1.8204E-11 μm^3

3. Number of molecules of $CaCO_3$ in the nuclei formed (M):

$M = \frac{v_n}{v_{uc}} * 4$
$M = \frac{1.8204E-11}{2.2691E-22}$*4 = 3.209E11 molecules $CaCO_3$

4. Number of moles of Ca^{2+} and CO_3^{2-} in newly formed nuclei (*y*):

$y = M * N/N_A$
y = (3.209E11 * 5494.764)/ 6.022E23 = 2.928E-9 moles $CaCO_3$

5. Moles of Ca^{2+} and CO_3^{2-} in flow cell originally:

Moles of Ca^{2+} in flow cell initially (mol_{Ica}) = v_{fc} * I_{Ca}*d_{sw}
mol_{Ica} = 2.339E-7*0.01*1030 = 2.409E-6 moles

Moles of CO_3^{2-} in flow cell initially (mol_{ICO3}) = v_{fc} * I_{CO3}*d_{sw}
mol_{ICO3} = 2.339E-7*0.006927 *1030 = 1.669E-6 moles

6. Final moles of Ca^{2+} and CO_3^{2-} in flow cell:

Moles of Ca^{2+} in flow cell final (mol_{Fca}) = mol_{Ica} - y
mol_{Fca} = 2.409E-6 - 2.928E-9 = 2.406E-6 mol

Moles of CO_3^{2-} in flow cell final (mol_{FCO3}) = mol_{ICO3} - y
mol_{FCO3} = 1.669E-6 - 2.928E-9 = 1.666E-6 mol

7. Final Ω in the flow cell:

Final concentration of Ca^{2+} in the flow cell (f_{ca}) = mol_{Fca} / (v_{fc} * d_{sw})
f_{ca} = 2.406E-6 / (2.339E-7*1030) = 0.00999 mol/kg

Final concentration of CO_3^{2-} in the flow cell (f_{CO3}) = mol_{FCO3} / (v_{fc} * d_{sw})
f_{CO3} = 1.666E-6/ (2.339E-7*1030) = 0.006915 mol/kg

$$\Omega = \frac{[Ca^{2+}][CO_3^{2-}]}{k_{sp}}$$

Ω = 0.00999 * 0.006915 / 6.46E-7 = 106.9

Change in Ω due to crystal growth and nucleation

8. Aragonite growth rate at Ω = 106.37:

$R = k(\Omega - 1)^n$
$R = 2.344E\text{-}5(106.37\text{-}1)^{1.6}$ = 0.04078 mol/m^2/h = 1.133E-5 mol/m^2/s

9. Amount of aragonite added onto top and bottom slides of flow cell, using the entire surface of the slides as the maximum growth that could be occurring:

mol_{arag} = R * t * 2*a
mol_{arag} = 1.133E-5 * 3.51 * 2 * 0.0006021 = 4.788E-8 mol $CaCO_3$

10. Change in Ω overall due to both aragonite growth and nucleation:

Moles Ca final ($mol_{Ca\text{-}arag}$) = mol_{Fca} - mol_{arag}
Moles Ca final = 2.406E-6 – 4.788E-8 = 2.358E-6 moles

Moles CO3 final ($mol_{CO3\text{-}arag}$) = mol_{FCO3} - mol_{arag}
Moles CO3 final = 1.666E-6 - 4.788E-8 = 1.618E-6 moles

Final concentration of Ca^{2+} in the flow cell (f_{ca}) = $mol_{Ca\text{-}arag}$ / (v_{fc} * d_{sw})
f_{ca} = 2.358E-6 / (2.339E-7*1030) = 0.00979 mol/kg

Final concentration of CO_3^{2-} in the flow cell (f_{CO3}) = $mol_{CO3\text{-}arag}$ / (v_{fc} * d_{sw})
f_{CO3} = 1.618E-6 / (2.339E-7*1030) = 0.006716 mol/kg

$$\Omega = \frac{[Ca^{2+}][CO_3^{2-}]}{k_{sp}}$$

Ω = 0.00979 * 0.006716 / 6.46E-7 = 101.8

2.11.2 *Derivation of Nucleation Rate Equation from Classical Nucleation Theory*

The free energy of formation of a nucleus (ΔG^*) is given by the formation of a new phase on a surface as a function of the radius, r, of the nucleus under a given set of conditions. The energy is the sum of the volume and the surface area penalty terms:

$$\Delta G(r) = -\frac{4\pi r^3}{3v}\sigma + 4\pi r^2\alpha \qquad \text{(Chapter 2.6)}$$

Where v is the molecular volume of the nucleus, σ is the supersaturation term, equal to ($\ln\Omega$), and α^3 is the interfacial energy term, an energy penalty that the nucleus must pay as it is forming caused by interacting with the nucleating surface and solution. At equilibrium, the surface nucleation rate is:

$$J_n = Ae^{\Delta G^*/k_BT} \qquad \text{(Chapter 2.7)}$$

where J_n is the steady state nucleation rate, ΔG^* is the energy or thermodynamic barrier required to form a nucleus of a certain size, k_B is the Boltzmann constant, T is the temperature, and A is the kinetic constant cofactor, determined by rate limitation of molecular motion. The energy of formation of a nucleus can be defined as

$$\Delta G^* = B\alpha^3\left(\frac{k_BT}{\sigma^2}\right) \qquad \text{(Chapter 2.8)}$$

Where B is a constant that is shape- and volume- specific constant that is experimentally determined and σ^2 is the supersaturation term, equal to $(\ln\Omega)^2$. α^3 is the interfacial energy term, an energy penalty that the nucleus must pay as it is forming caused by interacting with the nucleating surface and solution. Substituting Equation 2.8 into Equation 2.7 gives the equation

$$J = Ae^{\frac{B\alpha^3}{\sigma^2}} \quad \text{(Chapter 2.9)}$$

Or this equation can be log-log transformed to be written as

$$lnJ = lnA - B\alpha^3 \frac{1}{\sigma^2} \quad \text{(Chapter 2.10)}$$

Chapter 3. QUANTITATIVELY MEASURING THE EFFECT OF SKELETAL ORGANIC MATRIX PROTEINS AND FUNCTIONAL GROUPS ON NUCLEATION

3.1 ABSTRACT

As the oceans become more acidic due to anthropogenic climate change, it will become more thermodynamically and kinetically difficult for corals to grow their calcium carbonate skeletons. There have been opposing viewpoints in the scientific community regarding the relative balance between geochemical and biological influences on control of calcification. Calcification is correlated with Ω in the coral calcifying space, suggesting that calcification kinetics are determined by the concentrations of calcium and carbonate ions locally, but is also influenced by acidic organic matrix proteins, which have been suggested to enhance or inhibit calcification and nucleation, control orientation of crystals, or select crystal polymorphs. Aragonite nucleation has been shown to be more sensitive to Ω than mineral growth under the range of Ω values that are relevant to the internal calcifying space in corals, indicating that it will be greatly affected by ocean acidification. Here we test the effects of acidic matrix proteins, protein-analogues, and functional groups on inorganic aragonite nucleation rates, determining that a peptide from the acidic domain of a Coral Acid Rich Protein (CARP1) has the ability to increase nucleation rates above $\Omega = 15$, but inhibits nucleation rates below this value. Furthermore, we find that both charge and conformation of peptide play a role in the mechanism of this effect on nucleation. From these data, we find that it is unlikely CARP1 can promote nucleation under low Ω conditions or mitigate the effects of ocean acidification.

3.1 INTRODUCTION

Coral reefs are vital but fragile ecosystems, accounting for a significant proportion of the biomass and primary productivity in the oceans. Due to changing environmental conditions, notably increases in temperature and ocean acidification caused by anthropogenic emissions of carbon dioxide, coral reefs are in decline. This carbon dioxide flux into the oceans from the atmosphere affects the carbonate system, shifting the balance of chemical speciation away from carbonate ion (CO_3^{2-}), a necessary component of coral skeletons, which are formed out of calcium carbonate as a polymorph called aragonite. The saturation state (Ω) of aragonite is a measure of the thermodynamic ability of calcium carbonate to form. Corals experience an average Ω_{SW} (Ω of seawater) of between 3-4 in today's oceans (50). Lower than 3 creates stress for corals as they form their skeletons, and if Ω_{SW} decreases to below 1, dissolution can occur. By 2100, the carbonate concentration in the ocean, and therefore the aragonite saturation state, is expected to decrease by 60%, which will significantly affect coral reefs (9). In order to fully predict the fate of corals in the oceans in the near and far future, we need to gain a greater understanding of their basic skeletal growth processes and how these processes react to environmental change.

One such process is nucleation, the first step in coral skeletal growth. Nucleation is a phase change, the deposition of calcium carbonate crystals into solid form, and it acts as the blueprint of the skeletal architecture. Nucleation, like all coral skeletal growth, is an extracellular process that occurs in a region called the calcifying space that exists between tissue and existing skeleton. The chemistry of this chamber is under some measure of control by the coral, as it is able to pump ions in and out, ultimately determining Ω_{CF} (Ω of the calcifying fluid in the calcifying space) (19). Ω_{CF} has been both indirectly and directly measured, with values found to

be ranging from 10-25, far higher than that of the surrounding seawater (22, 24–27, 51). Although the Ω_{CF} is increased above that of the external seawater, as environmental Ω_{SW} decreases, so does internal Ω_{CF} (25), showing that corals are not entirely able to buffer their internal processes from ocean acidification. Clearly corals have some measure of chemical control over Ω_{CF} and of the calcifying fluid that forms their skeleton, but as growth occurs in a live organism, they may exert control over skeletal growth in other ways too.

One important element of skeletal growth is the skeletal organic matrix (SOM), which refers to organic molecules that are associated with and embedded in the skeletons of different calcifying organisms, including corals, mollusks, and oysters. The SOM is thought to play several roles, including controlling polymorph selection, controlling crystal orientation, as a scaffold for nucleation, and as a way to increase or decrease rates of nucleation and calcification (33, 74, 75). Understanding the role of the SOM in corals through direct experiments is challenging and is an area of active research, but organic-mineral interactions are thought to control nucleation and calcification through surface energy kinetics, molecular templating, or both (37, 41, 42, 72, 76). The organic matrices across different organism types have been consistently found to be enriched with acidic amino acids, especially aspartic acid (29–31, 77). These acidic proteins are often associated with the skeleton and with nucleation specifically. However, the function and mechanism of these highly acidic proteins remains an open question.

Relatively recently, highly acidic matrix proteins were identified from three coral skeletons from the families Pocilloporidae and Acroporidae using a proteomics approach (34, 52, 53). In particular, a family of acidic SOM proteins called coral acid rich proteins (CARPs) was isolated from the skeleton of *Stylophora pistillata,* an Indo-Pacific tropical coral (35). These proteins, like organic matrix proteins found associated with the skeletons in other calcifying organisms, are

characterized by repeated acidic units. It is presumed that different CARPs have different functions, and although these proteins share acidic features, they do not have sequence homology. At least some of the CARPs appear to have arisen independently and are not from the same gene family.

Several studies have attempted to discern the location of CARPs in the skeleton and tissue, expression patterns, and effects on calcium carbonate formation. Mass et al., 2013 observed that CARPs 1-4 promoted *in vitro* calcification under low pH conditions, while assays with control peptides did not produce any crystals (35). CARPs 1 and 4 were found localized to the early mineralization zones in the skeleton, where nucleation occurs, by Mass et al., 2014, while CARPs 2 and 3 were located in the mineral growth layers in the skeleton (43). CARPs 1 and 4 were also found to be localized on newly forming crystals on *S. pistillata* protopolyps, presumably involved in nucleation (46). Gene expression for CARPs 3 and 4 was found to be upregulated in protopolyps as pCO_2 concentrations were increased, although expression for CARPs 1 and 2 was not measured in that study (47). Two studies have observed that CARP2 gene expression is upregulated during the larvae settling stage in two different coral species, while the gene expression of the other CARPs is upregulated during the skeleton formation phase of young corals (44, 45). Finally, CARP3 has been shown in two *in vitro* studies to possibly be involved in polymorph selection (48, 49).

These experiments indicate that CARPs are involved in the skeleton growing process, and that CARPs 1 and 4 specifically may be involved in nucleation in corals. CARPs may increase nucleation rates or create more favorable chemical environments for nucleation, but many questions remain, such as the role that CARPs 1 and 4 actually play in nucleation, the mechanism of how these CARPs work, and what the magnitude of their effect is.

Despite nucleation's importance to the foundation of the coral skeleton, nucleation is an understudied process in corals, both in the fundamentals of the process and the way in which nucleation interacts with the organic matrix. Multiple studies have investigated the kinetics of inorganic calcite nucleation, including measuring rates under different saturation states as well as the effects on rate of surface energy and chemical chain lengths and moieties (42, 73, 78). There have been few comparable studies done with aragonite nucleation, however.

In Chapter 2, we measured rates of inorganic aragonite nucleation using a flow cell set up and at a range of Ω values to determine a baseline of aragonite nucleation kinetics relevant to the conditions under which nucleation occurs in corals. These results indicate that aragonite nucleation is sensitive to changes in Ω, and furthermore that that sensitivity is different from the reaction of mineral growth rate to the same environmental change. Njegić Džakula et al., 2019 measured kinetic and thermodynamic parameters of *in vitro* aragonite nucleation and crystal growth in artificial seawater with increasing concentrations of SOM extracted from two coral species at starting Ω values of 11 and 5.8. They found that both nucleation and mineral growth were inhibited by the SOM present. They observed increasing induction times with increasing concentrations of SOM, but otherwise few changes to growth rates (79). They also observed that aragonite nucleation did not occur at the low Ω condition in the presence of SOM extract. These experiments were the first to measure the effects of the SOM on aragonite growth kinetics.

Although few studies have been done using aragonite, numerous studies have investigated the effects of functional groups, single amino acids, and peptides on bulk calcite, calcium carbonate formation, and calcium carbonate nucleation. Many of these studies focused on acidic amino acids and peptides due to the prevalence of these residues in OM proteins. Both experimental techniques and simulations have shown that single amino acids and oligopeptides

inhibit calcification and nucleation through stabilization of liquid calcium carbonate ionic networks, especially aspartic acid (80–85). On the other hand, Elhadj et al, 2006a, Ehadj et al., 2006b, and De Yoreo et al, 2007 used AFM to measure calcite step rates in the presence of increasing concentrations of single amino acids and oligopeptides and found that these additives can increase calcite growth at low concentrations, while inhibiting at higher concentrations (67, 86, 87). Njegić-Džakula et al., 2009 observed a similar effect for poly-lysine but saw inhibition of calcite step growth in the presence of poly-aspartic acid at all concentrations (88).

Taken together, it is clear that there is a knowledge gap regarding the impact of acidic matrix proteins and functional groups on aragonite growth at every step, especially with regard to how these moieties affect aragonite nucleation. We tested acidic, basic, and neutral polypeptides of two chain lengths for their effects on aragonite nucleation rates, densities, and induction times. In addition, we tested a peptide from the acidic domain of CARP1 and the full CARP1 protein in order to investigate further the role of the organic matrix proteins on nucleation. All experiments were run at a wide range of saturation states, including environmentally relevant conditions. This is the first study that we are aware of that quantitatively measures the effects of chemical compounds and an individual SOM protein on aragonite nucleation. Quantifying nucleation rates and densities and the sensitivity of these parameters to organic-mineral interactions will demonstrate whether the effects of SOM proteins can override saturation state and increase rates and densities under low Ω conditions. These data can provide information about whether corals are able to use the SOM to mitigate the effects of ocean acidification, as well as providing a broader understanding of the kinetics of nucleation as they may apply to corals. We find that CARP1 peptide can act to both enhance and inhibit nucleation rates at different Ω values, with the pivot point for the switch in behavior at around $\Omega = 15.2$. Above this value, nucleation is

increased, while below it is fully inhibited. This result indicates that as Ω_{SW} decreases, with a commensurate decrease in Ω_{CF}, the rate and density enhancing effects of CARP1 will become less achievable for the coral.

3.2 METHODS

3.2.1 *Aragonite Nucleation Rate Measurements*

The aragonite nucleation rates were measured in a flow cell setup documented in detail in Chapter 2. Here we briefly describe the setup. Two solutions of modified seawater, one containing Ca^{2+} and alkalinity and one containing dissolved inorganic carbon (DIC), were mixed together in spiral tubing using a microprocessor-controlled peristaltic pump at 4 mL/min. The solutions were pumped into a Warner Instruments Low Profile Parallel Plate Flow Chamber (RC-31) with laminar flow and glass slides on top and bottom. The solutions were held at a constant temperature of 25°C and continuously pumped out through the exit line of the cell. Nucleation occurred heterogeneously on both surfaces, and was monitored on the underside of the top glass slide of the flow cell. The cell was placed under a Nikon Eclipse E600 POL microscope with cross-polarized light and time-lapse images were taken throughout each experiment every 15 seconds or more frequently. Experiments lasted between 1-10 hours, depending on the Ω, which varied between 7.76-106.4. Nuclei on the glass slide were characterized by light microscopy to verify that the majority of the nuclei were aragonite, based on morphological similarity to previously measured nuclei that had been characterized by Raman spectroscopy.

3.2.2 *Organic Additives*

Organic additives were used in these experiments to test effects of different functional groups and to act as proxies for organic matrix proteins. The peptides poly-L-lysine hydrochloride (Lys30x), MW=4,900 Da (≥90%) and poly-L-aspartic acid sodium salt (PAA30x), MW=4,100 Da (≥90%) were purchased from Alamanda Polymers. The short peptides with 4 residues Asp-Asp-Asp-Asp (PAA4x) (≥97%), Lys-Lys-Lys-Lys (Lys4x) (≥95%), and Gly-Gly-Gly-Gly (Gly4x) (≥98%) were obtained from Sigma Aldrich. The CARP1 peptide that was used in this study represents the active acidic section of the protein as determined by Mass et al. 2013 and used in subsequent experiments therein (35). This peptide was synthesized by Pierce Custom Peptides with 87% purity (sequence in Supplemental Figure 3.5A). For one additional experiment we also used a separate full sequence CARP1 recombinant protein that was expressed in *E. coli* following the methods of (35) (full sequence in Supplemental Figure 3.5B).

3.2.3 *Preparation of Solutions*

The two modified seawater solutions contained NaCl and when mixed together had an ionic strength of 0.67, close to the ionic strength of seawater, which is approximately 0.7 (55). They were created for each nucleation experiment or group of experiments at a specified Ω. Solutions contained the salinity of seawater, the carbonate alkalinity, and some of the major ions of seawater, including Na^+, Cl^-, Ca^{2+}, and Mg^{2+}, but did not contain SO_4^{2-}, K^+, Sr^{2+}, Br^-, $B(OH)_3$, or F^-, any minor ions, trace metals, nutrients, or other dissolved species found in natural seawater.

Both solutions contained NaCl, and one solution contained Ca^{2+} and Mg^{2+}, added through $CaCl_2 \cdot 2H_2O$ and $MgCl_2 \cdot 6H_2O$, while the other contained sodium bicarbonate ($NaHCO_3$) and sodium hydroxide (NaOH). The concentrations of Ca^{2+} and Mg^{2+} were held constant at 0.01

mol/kg and 0.02 mol/kg, respectively. The concentration of Mg^{2+} was set at this level to avoid the formation of brucite during the experiment, which occurred at higher Mg^{2+} concentrations. The calcium solution also contained the organic additives for that experiment. The concentration of organic additive was set to match approximations of the concentration of the organic matrix in the skeleton of *S. pistillata* as determined by (35). Using this value of 0.1 μM, we calculated the concentration of acidic residues of CARP1 peptide in these experiments and then adjusted the concentrations of each peptide additive so that the concentration of charged residues was kept constant and equal to this value (Supplemental Table 3.3).

The amount of NaOH was varied to change the pH of the final solution, and therefore Ω, while DIC was held constant at 0.008 mol/kg. The amount of NaOH was adjusted to account for the impact of organic additives on pH, keeping Ω at specific values. Ω remained constant throughout the experiment because of the flow-through system replenishing the chemistry of the solutions in the cell.

3.2.4 *Calculating Nucleation Rate, Density, and Induction Time*

For each experiment, the nucleation rate was calculated by counting the number of nuclei in each image and plotting the number of nuclei versus time. When the relationship of the two is linear, it signifies steady state nucleation growth, and the slope of the line is the rate. When the nucleation rate was not constant, this is noted in the text and the maximum nucleation rate was calculated using the last several data points of growth. All rates were normalized to area. The number of nuclei in each image was calculated by hand counting images or subsections of images.

The density of nucleation was determined by hand counting nuclei on an image at the end of an experiment and dividing by the area. The density of nuclei in these images is related to, but

not the same property as, the nuclei ground density, which was a model output in Chapter 2. That parameter was calculated when the area of a surface was covered by 90%. Here the nuclei density represents a means of comparison at the end of each experiment but would not necessarily be the same as when a surface was fully covered. The induction time was determined to be when the first nucleus that was deposited was clearly visible. The beginning of each experiment (t=0) was when the first image was taken, which was directly after the solution first entered the flow cell.

The curve for each plot was fit by transforming the data so that the parameters have a linear relationship and finding the slope and intercept of that line. ln Rate has a linear relationship with $\frac{1}{(ln\ \Omega)^2}$, while ln density and ln induction times have linear relationships with $1/\Omega$. ln Density and ln induction time have a linear relationship as well.

3.3 RESULTS

The rates, densities, and induction times of aragonite nucleation at a range of Ω values were measured with the addition of various dissolved additives. Polypeptides containing acidic, basic, and neutral amino acids were used to test the effects of different functional groups on nucleation. Two chain-lengths of the acidic and basic oligopeptides were used in order to compare effects of conformation and charge density, as opposed to charge alone. A peptide from the acidic region of CARP1 was used to directly test the effects of a protein from the organic matrix of a coral on the nucleation process, with one experiment run with the recombinant full CARP1 protein to compare the effects of peptide versus protein. Baseline aragonite nucleation rates with no additives were measured in Chapter 2, and we use those measurements as a control (referenced

as inorganic hereafter). In addition, inorganic nucleation experiments with no additives were run in between trials with additives to ensure consistency of the experimental setup and conditions.

For each additive, we have plotted the log of the rate versus Ω to get a sense of the trends, as well as a log-log plot of rate versus the parameter $\frac{1}{\sigma^2}$, where $\sigma = ln\ \Omega$. This parameter comes directly from the equation for nucleation rate (Equation Equation 3.1) as described by classical nucleation theory (CNT) (15). In the classical model of growth, nucleation occurs through random movement of single particles that form a crystal once a critical size is reached. Other factors that play a role in how quickly nuclei can form are the supersaturation (Ω) and the interfacial energy between the nucleus and the solution.

$$lnJ = lnA - B\alpha^3 \frac{1}{\sigma^2} \qquad \text{(Equation 3.1)}$$

B is an experimentally determined constant that is shape and volume-specific, α^3 is the interfacial energy, and lnA is based on molecular motion and is an indicator of the maximum nucleation rate possible under given conditions.

Nucleation rates can be plotted in this log-log form to check whether CNT holds true for that set of conditions. If so, indicated by a linear relationship in the log-log plot, then the slope of that line is proportional to the interfacial energy, which can be calculated for the formation of those nuclei. It is useful to be able to classify the kinetics of these experiments as consistent with CNT or not because it provides possible mechanisms of nucleus formation and enables us to calculate properties that affect nucleation within this framework such as interfacial energy.

Using multiple linear regression with additive type and Ω as independent variables, it can be determined that there are significant statistical differences between each peptide rate as compared to the inorganic experiments alone (all p-values < 0.05, adjusted $R^2 = 0.64$). However, qualitatively the results fall into two groups: the first groups contains most of the polypeptides

(PAA4x, Lys4x, Lys30x, and Gly4x; Group 1) and the second contains the long chain acidic polypeptide (PAA30x) as well as the SOM protein CARP1 (Group 2).

The largest qualitative difference between Group 1 and Group 2 peptides is the number and size of nuclei at the end of the respective experiments (Figure 3.2B, C, and D). Group 1 nuclei were larger than Group 2 nuclei and much less dense. Group 2 nuclei were often so dense at the end of an experiment that they covered the entire slide and were not easily distinguishable from one another.

3.3.1 *Group 1 Peptide Rates*

As seen in Figure 3.1 and Table 3.1, the nucleation rates of the Group 1 polypeptides PAA4x, Lys4x, Lys30x, and Gly4x either were less than or did not differ greatly from the rates of inorganic aragonite nucleation alone. The Group 1 polypeptides all appear to follow CNT kinetics based on Figure 3.1B. We can calculate the interfacial energy term for these additives (Table 3.2). The interfacial energy is higher for each of the additives than it is for the inorganic nucleation alone, representing a relative destabilization of the nuclei surface, although this is not significant in most cases. This provides a mechanism to explain the pattern whereby the additives slightly decrease nucleation rates at lower Ω values as compared to inorganic nucleation.

3.3.2 *Group 2 Peptide Rates*

One observable difference between the Group 2 experiments (PAA30x and CARP1) and all others discussed so far is the shape of the growth curve with respect to time. For inorganic experiments and Group 1 polypeptides, nucleation rate remains at a constant steady-state value until a certain point when coverage is high and the number of nuclei levels off. In the presence of

PAA30x and CARP1, nucleation was not constant and, in most cases, did not level off, appearing to form an exponential (Figure 3.2A). In order to compare nucleation rates between experiments with the different additives, we took the maximum nucleation rate from each PAA30x and CARP1 trial, reported in Table 3.1 and seen in Figure 3.1C-F. This is reasonable for the types of questions we answer here because we are comparing maximum nucleation rate to maximum nucleation rate across each experiment. We are also most interested in the maximum nucleation rate that is caused by each additive, and especially the maximum rates as compared to inorganic experiments alone when trying to determine the capacity of organic modifiers to accelerate nucleation.

At Ω values of 28.2 and lower , the PAA30x experimental results show a complete inhibition of nucleation within the 6 hour long typical duration of our experiments (Figure 3.1C, Table 3.1). This result was dramatically different than both inorganic nucleation and the other polypeptide additives, even PAA4x. We can see that PAA30x causes nucleation rates to drop steeply below Ω values of 54.8. Using just the experiments with measurable nucleation rates to calculate slope, adding this modifier increases interfacial energy, more than doubling it from inorganic nucleation and also increases the y-intercept, which corresponds to the maximum nucleation rate. To calculate slope of the line in Figure 3.1D we use $\Omega = 28.2$ as the x-intercept. This x-intercept corresponds to the oversaturation value below which nucleation is totally inhibited. From our experiments, the x-intercept should fall between Ω values of 28.2 and 34.8. We used 28.2 as the more conservative option, although it is possible the line has a steeper slope than shown here. Because the effect of this peptide is different from that of PAA4x, this change in interfacial energy is not due simply to the presence of acidic residues alone.

In the CARP1 experiments, we can observe that the maximum nucleation rates are higher than inorganic nucleation rates at Ω values above 15.2 (Figure 3.1E) and that the CARP1 line intercepts the inorganic nucleation line around the same Ω value (Figure 3.1F). Below this Ω value, nucleation rates are predicted to be lower in the presence of CARP1 than in inorganic experiments. Similarly to PAA30x, this steep slope indicates a high interfacial energy when interpreted within a classical nucleation theory framework (Table 3.2). The 'zeros' on the y-axis represent trials in which no nuclei were ever formed. We did not average these points with the experiments at the same Ω where nucleation did occur in order to show the spread of possibilities. All points were included when calculating the slope of the line, although, similarly to PAA30x, the trial resolution is not fine enough to know exactly where the x-intercept is more exactly than between Ω values of 7.76 and 15.2. These results indicate that different energetics govern the relationships between the nuclei, the solution, and the surface in the presence of CARP1 and PAA30x than for Group 1 polypeptides, but that similar mechanisms of action could be occurring in solutions with CARP1 and PAA30x.

3.3.3 *Rate, Density, and Induction Time*

Density and rate have a strong linear correlation in the log-log plot (Supplemental Figure 3.8A) which is consistent across all experiments (p-value << 0.001, adjusted $R^2 = 0.79$). The CARP1 and PAA30x experiments extend the line beyond all other experiments but appear to be on the same line. This relationship between ln density and ln rate is expected given that rate can be written as a function of density: rate is equal to density/total time (nuclei/area/s). Density and rate have similar responses to changes in additive and Ω, with the notable exception that PAA30x does not increase rates above inorganic, but does increase densities.

There is a power relationship between density and induction time of nuclei in inorganic aragonite experiments that holds true across all polypeptide experiments, except for PAA30x (Figure 3.3), with the powers ranging from ≈-0.8 to ≈-1.8. In CARP1 and PAA30x experiments, induction times were longer and nucleation densities were relatively high in comparison to inorganic experiments at similar Ω values (Figure 3.2A-D). It is notable that although the CARP1 experiments experience both higher induction times and higher densities, these experiments maintain the power relationship between the two variables, with a power of -1.2, which is not significantly different from the experiments with other additives. These results seem to indicate a near-universal relationship between these two parameters. In Figure 3.3, Group 1 and Group 2 additives are separated in induction time and density space.

Density and induction time can also be plotted as functions of Ω (Figure 3.4A and B). There are significant differences in induction time for each polypeptide as compared to inorganic results (all p-values < 10 E -5, adjusted $R^2 = 0.82$). However, only Gly4x, PAA30x, and CARP1 exhibit significantly different densities as compared to inorganic (p-values < 0.001, adjusted $R^2 = 0.63$). There is also a clear point or threshold value on both plots where the inorganic and Group1 values become asymptotic, above $\Omega = 30$. The same threshold exists for the relationship between J and Ω as well. This is significant because the range of values where the behavior is not asymptotic encompasses the Ω values that are thought to be maintained in the calcifying fluid in corals. Below this threshold, by changing Ω, the coral can rapidly increase density and rate and decrease induction time. Above these values, the coral will get no benefit in density, rate, or induction time by changing Ω. PAA30x and CARP1 nucleation have the same relationship with Ω, but appear to translate these curves along the x-axis, so that the steep part of the curve occurs at higher Ω values. PAA30x in particular causes the curve to change rapidly at higher Ω values

than exist in corals. For CARP1, the relationship between Ω and these three parameters is very steep, where the behavior changes from complete inhibition of nucleation to nucleation with high rates and densities with very little change in Ω. The change occurs around the value of 15.2. This switch-like behavior is seen to some extent in all of the curves, but is most extreme in CARP1, which is also unique in that this switch comes in the middle of the range of Ω_{CF}.

3.3.4 *CARP1 Protein*

Finally, we performed one nucleation growth rate experiment with the recombinant CARP1 protein. Due to limited material, only one experiment was possible at a high Ω value of 106.4 to check the form of growth as a function of time and to compare the nucleation parameters to experiments with the CARP1 fragment. The growth form of the experiment was linear, as opposed to the exponential-like growth observed during CARP1 peptide experiments (Supplemental Figure 3.7). Qualitatively, nuclei were larger than in CARP1 peptide experiments (Supplemental Figure 3.7). The rate was higher than inorganic experiments at the same Ω, but lower than CARP1 peptide, as was the density, and the induction time was similar to CARP1 peptide. This result does not confirm the effects of CARP1 peptide, but as only one experiment was run, more work is needed to further test the differences between peptide and protein.

3.4 DISCUSSION

3.4.1 *Polypeptide and CARP1 Rates*

After testing the effects of different functional groups on the nucleation process, it was clear that, despite variability between experiments, Group 1 peptides tend to decrease nucleation rates as compared to inorganic or have no effect, rather than cause an increase in rate. Group 2 peptides inhibit nucleation below threshold values, and in the case of CARP1, can elevate

nucleation rates above that threshold. Functional group identity cannot explain all of the differences between these additives, as poly aspartic acid results in very different growth effects depending on chain lengths (PAA4x vs PAA30x). Chain length and functional group act together to decrease nucleation, and secondary or tertiary structure are likely playing a role. Our findings are consistent with the molecular dynamic simulation results from Finney et al., 2020, that show that longer chain length oligopeptides inhibit nucleation more strongly at the same concentration due to strengthening a network of ionic bonds in solution.

Our results also provide evidence that none of these functional groups or peptides alone can counteract the effects of ocean acidification, and that neither coral growth processes nor human engineering efforts can utilize these functional groups in that manner. This seems self-evident for Group 1 peptides. For Group 2 peptides, PAA30x inhibits nucleation for the entire range of Ω_{CF}. CARP1 has the most nuanced result, as it can elevate rates above $\Omega = 15.2$. This leaves the window of Ω_{CF} values from approximately 15.2 to 25 for the coral to elevate rates. However, the effects of ocean acidification make it increasingly difficult for corals to elevate their Ω_{CF} values to the higher end of the range. It is possible that the Ω_{CF} will shift to below this threshold point entirely. As ocean acidification shifts Ω_{CF} to lower values, and therefore nucleation rates decrease, it becomes increasingly unlikely that corals can use CARP1 to elevate nucleation rates.

Another consideration is the role of PAA4x, PAA30x, or poly-aspartic acid molecules of varying chain lengths as an experimental analog for acidic SOM proteins and their effects on aragonite nucleation. This is a common practice, but the differences in effects between PAA30x and PAA4x, as well as PAA30x and CARP1 peptide indicate that poly-aspartic acid is a complicated stand-in for the SOM. From our experiments, we can conclude that polypeptides that are too short will not act convincingly as analogs of CARP1, or likely of other SOM

proteins, and indeed may not have any effect at all, on aragonite nucleation. Further experiments are needed using mixed chain length polypeptides and longer chain PAA to determine if longer chain lengths would result in even more inhibition.

PAA30x inhibits nucleation in the entire range of Ω_{CF}, so care should also be taken when using it as an SOM analog, as organic-mineral interactions in corals necessarily occur under conditions of $\Omega_{CF.}$ PAA30x differs from CARP1 in this regard, which only inhibits nucleation in part of the Ω_{CF} range. However, despite the fact that rates were different between PAA30x and CARP1, there is some evidence that the PAA30x experiments have a similar relationship between induction time and density (Figure 3.3). Although not conclusive, this does indicate that PAA30x may, at high Ω values where nucleation does occur, have similar behaviors and mechanisms to CARP1. Another argument in favor of the relationship between the two is that both cause exponential-like nucleation rates. We will further discuss what the possible shared mechanisms may be below.

Although the additives tested here do not increase nucleation rates, these functional groups may potentially act as a valuable tool to allow corals to decrease or inhibit nucleation in a controlled way. The organic matrix and by extension these functional groups could give the coral the ability to mediate the extent and pace of growth of the skeleton, controlling where and how fast to nucleate, and just as importantly, when not to nucleate. In what would otherwise be a purely thermodynamically driven process, these molecules could provide the coral with the ability to make decisions about where and when to expend energy, whether it be on growth or some other important internal process. Although corals cannot use these molecules to accelerate nucleation rates, they already have the means to do so by ion pumping to increase Ω in the

calcifying space. Together, these parameters may allow corals some means of control on nucleation.

3.4.2 *Expanding on Group 2 Nucleation*

The CARP1 and PAA30x nucleation experiments had markedly different results than any of the other polypeptide additives. Quantitatively and qualitatively, it can be seen that smaller, denser nuclei appear after longer induction times in these experiments (Figure 3.2C and D, Supplemental Figure 3.6), which is consistent with the result of Picker et al., 2012, who saw smaller and more dense crystals when studying the deposition of calcium carbonate in the presence of aspartic acid, as opposed to with no additive (82). One contributing factor is that it is likely that CARP1 and PAA30x are inhibiting mineral growth. It has been observed in multiple studies that oligopeptides inhibit calcite and aragonite mineral growth by adsorbing onto the growing edge and blocking new molecule addition, especially above specific concentrations (67, 76, 79, 84, 86, 88). This is consistent with our experiments because it would explain why smaller nuclei are observed than in inorganic trials. It also might provide an explanation for the higher density of nuclei observed. Under inorganic nucleation conditions, larger nuclei are preferentially formed over many smaller nuclei. The opposite happens under CARP1 and PAA30x conditions as nuclei are unable to grow larger at any significant pace. Therefore, it is energetically more favorable to form new nuclei rather than to grow existing ones, and many more nuclei can be deposited in places where mineral growth would be occurring instead.

Another marked difference between Group 1 and Group 2 nucleation is the growth curve with respect to time. We compared maximum growth rates between different groups in order to quantitatively measure the extent to which organic-mineral interactions may override Ω. However, it is worth considering what non-steady state growth in the presence of Group 2

additives would mean in corals. Figure 3.2A shows that these experiments have much slower growth rates to start out with than inorganic nucleation does. One caveat for calculating maximum nucleation rates is that for the PAA30x and CARP1 trials, the maximum nucleation rates observed may not be the maximum that would occur given a longer timeframe. The observed curves appear to fit an exponential function, but it is clear that in live corals, nucleation would not be left unchecked to deposit at a rate approaching infinity. What is less clear is if the shape of this curve would approximate a sigmoid in our experiments, or if it would functionally become a sigmoid due to an external forcing factor in corals. For example, after a certain amount of time or deposition occurs, the coral could apply either a kinetic or biological check on nucleation, either by stopping production of the SOM protein like CARP1, producing another molecule that inhibits nucleation, or by letting Ω decrease in the calcifying space through ion depletion. Given how dense the nuclei are at the end of CARP1 experiments, it is unclear how much longer the coral would need to increase growth to achieve the desired result. The maximum nucleation rates calculated provide evidence that CARP1 can increase nucleation rates above inorganic nucleation, but only at the end of each experiment.

3.4.3 *Models of Growth*

An open question concerns the model of growth of nucleation in our study, especially in the presence of CARP1 and PAA30x. Models of growth that are widely accepted in calcium carbonate and biomineralization systems include CNT, crystallization by particle attachment, through prenucleation clusters, by first forming or depositing an amorphous precursor, through oriented attachment, or some combination of the above (89). For the inorganic experiments and all additives besides CARP1 and PAA30x, we reference CNT as the simplest explanation of a model that fits the results observed. However, due to the non-constant growth during CARP1 and

PAA30x trials, it is likely that non-classical pathways of growth are occurring. Deposition of stable amorphous forms were not observed in any trial, but otherwise our study does not allow us to elucidate pathways further. It is important to note that for each of the CARP1 and PAA30x trials, nucleation rates were considerably slower than inorganic nucleation for most of the experiment, and it was only at high Ω that these rates increased to above those of inorganic nucleation. Here we used the CNT framework to get an estimate of interfacial energy in the CARP1 and PAA30x trials and as a means to compare the results of experiments with all additives, while acknowledging that the assumptions of CNT may not hold in CARP1 and PAA30x experiments. Thus, there are wider error bars around those estimates. It is interesting to note that when investigating the effects of the SOM on the aragonite growth in (79), they saw similar kinetic curves for growth when SOM was present and when it was not, which they interpreted to mean that the growth kinetics were not changing. Differences in experimental set up may play a role, as their experiments did not maintain constant Ω, which creates a necessary end point to the nucleation process. Differences between the effects of the entire SOM and one peptide component of it also obviously are in effect.

One benefit of the CNT model is that it will be easy to compare inorganic results to nucleation measurements in live corals. If and when nucleation rates in corals can be measured, it will be a logical next step to be able to compare both the growth curves and the other inorganic data to tease apart mechanisms in live corals.

3.4.4 *Implications for Corals*

The main question that we sought to answer was whether CARP1, or other additives, would be able to create a more beneficial chemical environment for nucleation at low Ω values. Despite high maximum nucleation rates observed for CARP1, there is evidence that this form of growth

would not assist nucleation at lower Ω values. We observe a switch-like behavior in CARP1 with regards to rate and density around Ω = 15.2. The inhibitive effects of these peptides corroborate the results of (79), who observed aragonite nucleation inhibition and long induction times in the presence of organic matter isolated from the skeleton of two coral species. Their experiments were run at Ω values of approximately 11 and 5.8.

In the case of CARP1, nucleation is enhanced to greater than inorganic values in the range of Ω values where nucleation is switched on. For CARP1, therefore, there is a potentially important two-fold inhibition-enhancement functionality. This functionality is able to exist under today's environmental conditions in the ocean with presumed ability of corals to increase Ω_{CF} to greater than 20. However, as oceanic pH decreases, the upper range of Ω_{CF} accessible to the coral will shrink. It is possible that the maximum value of Ω_{CF} in the ocean of the future will be 15.2 or lower, in which case the enhancement ability, and the switch-like capability of the protein, will be rendered ineffective.

The threshold value of where this switch occurs is important for understanding this protein functionality. It is possible that the intersection of the CARP1 and inorganic nucleation rate lines in Figure 3.1F occurs at a lower Ω than 15.2, given the paucity of data at these values. However, we also observed an experiment at Ω=15.2 in which nucleation did not occur, in contrast to the experiment that had maximum growth rates similar to inorganic nucleation. It is not clear what accounts for the differences in these two experiments, but one possibility is that this Ω is close to the threshold value of where CARP1 starts to cause inhibition and beyond which inhibition always occurs. At such a value, slight changes in experimental conditions could cause a different state of growth and push the experiment towards inhibition or not. This observation indicates that 15.2 is likely to be close to the intersection point.

In the 'switched-on' region of Ω values, CARP1 and PAA30x trials resulted in dense nucleation, and, in the case of CARP1, increased maximum nucleation rates as well. In addition to the benefits of increased rates, there are likely advantages for the coral to try to achieve increased nucleation density as well: it is intuitive, although still speculative, that a more nuclei dense skeleton would be stronger and more able to withstand stress. In addition, in Chapter 2, we found that nuclei density is related to an increase in horizontal extension rate. However, the long induction times and slow initial growth rates provide a tradeoff that means the coral needs to decide carefully about how to manage growth even in these switched-on regions of Ω. From Figure 3.3A and Figure 3.4A we can see that the density at the end of the CARP1 Ω = 15.2 experiment is within the range of the densities at the end of inorganic Ω = 15.2 experiments. The time it takes to achieve the final density in this experiment is about 20 times longer than in the inorganic experiments. By that measure, CARP1 nucleation is considerably slower than inorganic nucleation at this Ω, even though the calculated rates are similar (Figure 3.1E), because the induction time is significantly greater for the CARP1 trial under these conditions. At higher Ω values than 15.2, but still within the range of Ω_{CF}, the tradeoff between induction time and density becomes more and more beneficial. As pH in the ocean lowers, and the maximum value of Ω_{CF} decreases, it is possible that the coral will still be able to access the 'nucleation on' portion of Ω_{CF}. However, the tradeoff that will have to be made for higher rates and densities will become less advantageous.

Along those same lines, it is clear that CARP1 provides a more beneficial density and rate versus induction time tradeoff than PAA30x (Figure 3.4A and B). PAA30x experiments have higher induction times than CARP1 trials at the same Ω, but don't cause as great an increase in density or rate as CARP1. In Figure 3.4A and B, we can see that the steep change in induction

time and density for PAA30x come at Ω values greater than 30, which are thought to be less likely to be found in the calcifying fluid. In contrast, CARP1 results on those same plots have steep slopes between 15 and 30, which overlaps with the predicted calcifying fluid Ω. Although the two may be acting with similar mechanisms, CARP1 is clearly more optimized for coral growth than PAA30x.

Despite the fact that CARP1 likely does not elevate nucleation rates at low Ω values, the fact that this intersection point exists could be a very useful tool for corals if it occurs in their calcifying space. As discussed previously, there are many scenarios where having the ability to "turn off" nucleation would be beneficial to the coral. CARPs and other additives, in conjunction with Ω, potentially give corals a mechanism for even more control: both the ability to increase rate and density of nucleation and the ability to slow down and inhibit nucleation using the same molecule. By adjusting the chemical environment, they can affect the function of the protein, and create a physiological switch to control growth processes.

3.4.5 *Mechanisms of Growth*

There are several mechanisms at play that could account for the long induction times observed in CARP1 and PAA30x experiments. As discussed, the experimental set up used in this work is not readily able to differentiate between non-classical forms of nucleation, so any definitive claim about the kinetics of formation in our study would be speculative. It is possible that the addition of CARP1 and PAA30x fully inhibits aragonite nucleation across all Ω values, and the smaller, denser nuclei that we observe are representative of a new phase, such as ACC. Although morphologically these nuclei look very similar to the aragonite nuclei observed in inorganic experiments, we were not able to more directly ascertain the identity of these nuclei using methods such as Raman spectroscopy or SEM. However, while we cannot rule out this

possibility, it ultimately does not change the impact of the switch-like behavior of CARP1. Even if a new phase, such as ACC, is formed, this polymorph is still inhibited at low Ω values, indicating that the change in phase would not promote nucleation in an acidifying ocean. Here we discuss one possibility of the dynamics at play that fit the observations, but multiple growth models could fit our data.

One consideration when thinking about mechanisms of growth is the interactions of additives with the ions in solution before and during when deposition occurs. These interactions may be the cause of non-classical growth effects by promoting and stabilizing ion clusters in solution. Multiple studies have shown that acidic amino acids and peptides strengthen and stabilize the calcium carbonate ionic networks in solution before nucleation occurs (80, 82, 85). Although the mechanism of how these additives act is not fully known, it is thought that the more fully solvated charged residues there are in a particular area, the more the soluble ions are stabilized. Additionally, the conformation and stereochemistry of the molecule is also thought to be important, as this conformation can allow the additive to better adsorb onto calcium carbonate ionic networks. This stabilization of dissolved species is shown to increase induction time and inhibit nucleation, as it becomes much more energetically favorable to remain in solution (80, 90).

A related factor is the interfacial energy that must be overcome in order to form a new nucleus. Based on Figure 3.1D and F and Table 3.2, PAA30x and CARP1 both raise the interfacial energy of the nucleation process. The stabilization of the dissolved ions could be related to this interfacial energy increase – if the solution is in an energetically stable form, then breaking those bonds to form and maintain nuclei would take more energy and inhibit nucleation at lower Ω values. Although we've mentioned the non-classical pathways to growth that trials

with these two additives may be taking, interfacial energy is undoubtedly still playing a role in nucleation.

Previous studies corroborate these mechanisms with their observation that non-acidic amino acids and peptides also caused slight changes to the nucleation process, notably inhibition, through the same mechanisms (79, 80, 82). Glycine, for example, was shown to have an effect on the solubility of calcium carbonate particles, possibly by joining into the ionic lattice of the crystal (82), and Finney et al., 2020 found that tetramers of arginine, glycine, and aspartic acid all affected the ionic networks in solution (80). In our work we observed that Lys4x, Lys30x, and Gly4x all had slightly lower nucleation rates and slightly higher interfacial energies than inorganic nucleation alone, which would agree with the results of these studies.

One remaining detail is accounting for the difference in nucleation caused by PAA30x and CARP1. These differences we attribute in part to the secondary structure of the peptides. The experimental solutions were made so that the concentration of total acidic residues was the same between them, so it is not due to differences in the concentration of functional groups present to interact with dissolved ions. However, as mentioned, additive conformation is theorized to play just as much of a role in impacting nucleation as charge and polarity. CARP1 is predicted to have several subsections with α-helices but also to have a high proportion of disordered regions (35, 91). PAA30x, on the other hand, is predicted to be completely disordered (91). While CARP1 is predicted to be fully solvated, perhaps its more ordered structure is not able to form as many bonds and strengthen the ionic network of the solution as much as PAA30x. More work is needed to understand CARP1's secondary structure in solution and the interactions with calcium carbonate ions to fully explain the differences in results between the two peptides.

3.4.6 *CARP1 Protein*

Only one trial was run with CARP1 protein, and this trial showed characteristics of both Group 1 and Group 2. If we view Group1 and Group 2 growth as two ends of a spectrum, CARP1 protein nuclei qualitatively looks more Group 1 results, but its numeric values for the three properties discussed fall in between inorganic and CARP1 peptide values. While this one trial is by no means conclusive of the behavior of CARP1 protein, it does indicate that there may be some differences in using the peptide versus the protein to predict the behavior of SOM proteins. One major difference is the predicted secondary and tertiary structures. While CARP1 peptide is thought to be mostly disordered and fully solvated, CARP1 protein is predicted to have alternating ordered (α-helix) and disordered regions as well as buried residues, which could account for differences seen between the two (91). Due to differences in size, there necessarily will be a difference in tertiary structure as well. For instance, CARP1 protein contains an EF-hand like domain which is not present in the peptide, which may bind Ca^{2+}, and may therefore play an additional role in calcification which warrants further exploration.

3.4.7 *Induction Time and Density*

There are consistent relationships between induction time, density, Ω, and rate across all experiments conducted. The fact that these relationships are consistent regardless of the additive indicates that they may be fundamental to the nucleation process, and as such could provide valuable information about nucleation in corals. When considering induction time versus Ω, one factor to notice is that additives only serve to increase induction time as compared to inorganic (Figure 3.4B), with PAA30x causing the greatest increase. Since induction time is one indicator of inhibition, this is another demonstration that additives cause inhibition overall.

Comparing Figure 3.4A and Figure 3.8B, we can determine that the increase in density from CARP1 is greater than the increase in rate in the same experiment as compared to inorganic experiments. This observation may indicate that gains in density are the true benefit of CARP1 for a coral, rather than gains in rate. In Chapter 2, we found that nucleation density is a result of the balance between nucleation rate and crystal growth rate at a given Ω. The Chapter 3 data support this find, given that Group 2 peptides have significantly higher densities than Group 1 peptides, and there is evidence that crystal growth is inhibited when Group 2 peptides are present.

Density is important because it is the only parameter of the ones considered that leaves a record in corals. If we can measure nucleation density, it is possible we could then make estimates of other parameters, and get information about the conditions under which the coral was living and growing in the past. The correlation between density and rate (Supplemental Figure 3.8A), for instance, could be used to make estimates of rate and put boundaries on possible additives or Ω values at the time of deposition. The model output results from Chapter 2 show that as density increases, so does extension over the range of Ω_{CF}, validating that density can be used as a predictive parameter from the coral skeleton. Further inquiry into how density and other growth parameters vary in live corals will be needed to test whether these relationships hold true beyond inorganic studies.

3.4.8 *Concentration Effects*

Additive concentration is an important parameter that in this study was held constant with regards to the number of charged functional groups throughout all polypeptide experiments and equal to the acidic residues in CARP1 peptide. We did some preliminary testing of concentration effects, testing dilute CARP1 peptide and more concentrated PAA4x (Supplemental Table 3.4).

In the dilute CARP1 experiments (0.1x), the exponential form of growth did not occur – instead, steady state linear growth was observed, similar to inorganic experiments. The rate and density were very similar to inorganic results. The induction time was high, which was the only similarity to the other CARP1 trials. This shows that there is some threshold concentration of peptide or protein needed in order to cause most of the CARP1 effects. The PAA4x experiments with 2x and 10x greater concentrations of PAA4x showed no change in results.

Njegic Dzakula et al. 2019 observed greater inhibition of both aragonite nucleation and calcification with increasing concentration of SOM extract. The concentration used in this study was on the low end of the range investigated by (79). This is the only previous work we know of that tested SOM protein concentration on aragonite nucleation and growth. According to work done by (67, 86, 88) lower concentrations of oligopeptides caused an increase in calcite step growth, but higher concentrations caused inhibition. Although the concentration of additives used in this study was within the range of peptide concentration that increased calcification seen in those studies, we see no evidence of the same effect in aragonite. It is possible that higher concentrations of CARP1 would cause more inhibition of aragonite and therefore create higher maximum nucleation rates than observed in our study. However, another effect could be greater inhibition of nucleation, as observed by (79). One possibility is that a change in concentrations could shift the Ω threshold value of the switch-like behavior of CARP1. Increasing the concentration seems more likely to shift the switch point to higher Ωs, and a decrease in concentration could conceivably shift the point to lower Ω values. However, our experimental results at low concentration show that there is a minimum concentration needed to achieve enhancing effects of CARP1 at all.

Because our study was focused on aragonite rather than calcite, and on nucleation rather than calcification, the range under which each of these additives is active in affecting both nucleation and calcification needs to be further investigated. Furthermore, the range that is plausible in living corals and the overlap with the active range of these peptides will need to be determined. It is likely that concentration of additives will have a significant effect on the nucleation process and as a parameter could be another tool that corals could use to control nucleation internally.

3.5 CONCLUSION

We tested the effects of acidic, neutral, and basic polypeptides on nucleation and none of these groups can increase aragonite nucleation rates under environmentally relevant Ω conditions. Although CARP1 can increase density and nucleation rate at Ω values of 15.2 and greater, it comes at the cost of greater induction times and slow initial growth, and it is unlikely that this peptide can increase nucleation rates significantly for low Ω values. However, CARP1 in conjunction with Ω may act as a useful physiological switch for corals to control their growth processes. The value of this switch-like behavior in corals is predicted to decrease with increasing ocean acidification. The relationships observed here between nucleation rate, density, induction time, and Ω may serve as a fundamental baseline of the properties of inorganic aragonite nucleation to help elucidate mechanisms of *in vivo* nucleation in corals. Furthermore, the relationships between these parameters and density may indicate that information about growth processes can be obtained from fossil coral skeletons, although further exploration is needed of variation in live corals.

3.6 ACKNOWLEDGEMENTS

The authors acknowledge and thank J. Burke and R. Hoffman for CARP1 expression and purification; D. Anderson, T. Ugrai, S. Bergstrom, and K. Hall for lab assistance.

3.7 TABLES

Table 3.5. Rate, Density, and Induction Time Values for all Additive Trials*

Additive	Omega	Induction Time (s)	Density (# nuclei/mm^2)	ln J (nuclei/m^2/s)
Gly4x	106.4	300	537.40	15.28
Gly4x	106.4	300	90.78	13.28
Gly4x	106.4	150	347.37	14.42
Gly4x	106.4	495	52.05	12.31
Gly4x	15.2	1500	6.05	7.10
Gly4x	15.2	585	152.51	12.59
Gly4x	7.8	1500	13.31	8.82
Gly4x	7.8	1500	6.05	6.74
Lys4x	106.4	225	970.71	14.66
Lys4x	106.4	225	626.97	14.99
Lys4x	15.2	840	859.36	12.35
Lys4x	15.2	720	229.97	11.55
Lys4x	15.2	1605	13.31	7.44
Lys4x	7.8	3480	7.26	5.49
Lys4x	7.8	1500	23.00	6.18
Lys30x	106.4	195	334.06	12.89
Lys30x	106.4	150	1050.59	12.08
Lys30x	15.2	750	26.63	9.68
Lys30x	15.2	450	81.09	10.96
Lys30x	7.8	1500	15.73	8.91
Lys30x	7.8	3810	14.52	7.10
Lys30x	7.8	1350	9.68	7.63
PAA4x	91.4	195	1175.26	14.44
PAA4x	91.4	225	65.36	13.29
PAA4x	91.4	180	39.94	11.17
PAA4x	91.4	105	2843.14	16.55
PAA4x	91.4	165	169.45	13.17
PAA4x	91.4	240	503.51	14.13
PAA4x	15.2	885	190.03	12.14
PAA4x	15.2	1125	42.36	12.80
PAA4x	15.2	735	152.51	12.43
PAA4x	15.2	1125	354.64	12.24
PAA4x	15.2	435	939.24	13.33
PAA4x	12.9	795	55.68	10.31
PAA4x	12.9	1140	42.36	9.78
PAA4x	12.9	1500	13.31	9.49
PAA4x	10.1	750	23.00	8.82
PAA4x	10.1	1125	8.47	6.99
PAA4x	10.1	1590	12.10	9.00
PAA4x	10.1	1740	23.00	8.86
PAA4x	10.1	1950	16.95	10.39
PAA4x	10.1	2310	6.05	7.36
PAA4x	8.8	1980	302.59	11.98
PAA4x	8.8	3660	3.63	6.99
PAA4x	8.8	1860	76.25	10.12
PAA4x	8.8	1365	750.42	13.53
PAA4x	8.8	765	11712.66	16.45
PAA4x	8.8	1620	23.00	8.77
PAA4x	8.8	1320	65.36	9.41
PAA4x	7.8	2550	76.25	10.09
PAA4x	7.8	4500	21.79	9.31
PAA4x	7.8	2400	6.05	8.29
PAA4x	7.8	1890	158.56	11.28
PAA4x	7.8	1605	674.17	12.58
PAA4x	7.8	2415	261.44	11.36
PAA4x	7.8	4560	2.42	6.41
PAA30x	106.4	300	8660.13	15.09
PAA30x	106.4	1155	4866.86	15.19
PAA30x	54.8	2445	53288.55	15.99
PAA30x	41.3	3000	68.99	8.77
PAA30x	41.3	9000	4156.38	13.23
PAA30x	41.3	6000	11119.58	13.52
PAA30x	34.8	9000	77.46	8.97

PAA30x	34.8	7500	4307.67	13.43
PAA30x	28.2	NA	NA	0
PAA30x	28.2	NA	NA	0
PAA30x	15.2	NA	NA	0
PAA30x	7.8	NA	NA	0
PAA30x	7.8	NA	NA	0
CARP1	106.4	240	28951.83	19.35
CARP1	106.4	540	86202.19	18.08
CARP1	41.3	345	44965.52	17.46
CARP1	41.3	450	57610.75	19.75
CARP1	28.2	1440	41594.05	17.65
CARP1	28.2	1425	12420.35	18.22
CARP1	19.8	945	3838.52	14.13
CARP1	19.8	885	24451.71	15.78
CARP1	15.2	7485	630.61	11.53
CARP1 protein	106.4	345	981.60	15.87

*Inorganic data is in Chapter 2

Table 3.6. Interfacial Energy Values for each Additive

Additive	**IE (mJ/m2)**	**ln A (nuclei/m^2/s)**
Inorganic	6.74	15.38
Gly4x	7.27	14.83
Lys4x	8.32	16.89
Lys30x	7.51	14.38
PAA4x	6.48	14.24
PAA30x	15.66	32.56
CARP1	11.18	25.10

3.8 FIGURES

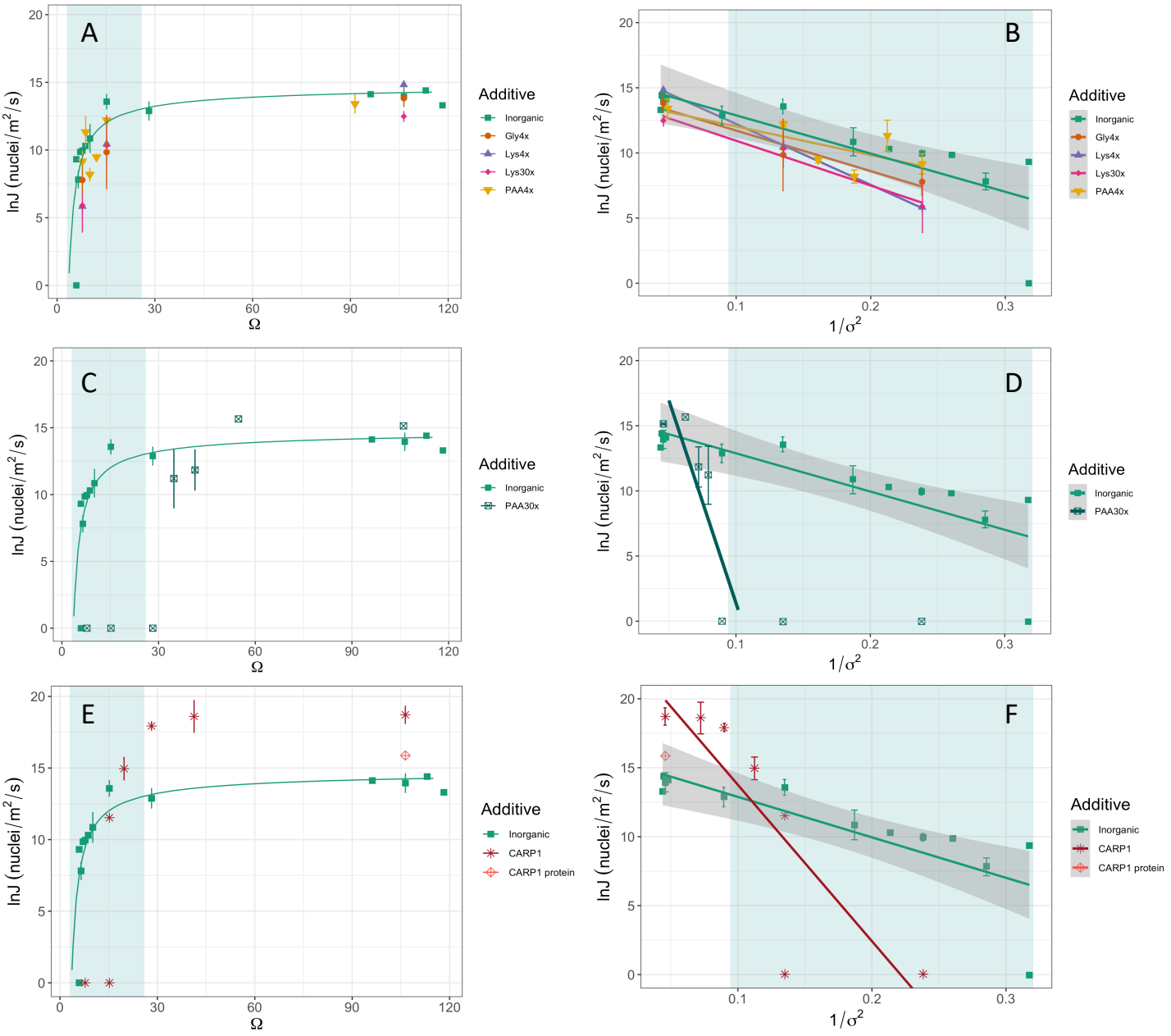

Figure 3.1. Nucleation rate plots of ln J versus Ω (A, C, E) and ln J versus $^{1}/_{\sigma^{2}}$ (B, D, F). All plots show inorganic nucleation rates with the exponential and linear fits for reference. In plots A and B, additives Gly4x, Lys4x, Lys30x, and PAA4x are shown to have similar values to inorganic nucleation. In plots C and D, PAA30x shows complete inhibition of nucleation at Ω values of 28.2 and below, with a steep line in D. The true x-intercept in D, where nucleation is completely inhibited, falls between 28.2 and 34.8. Plots C and D show a similar trend for CARP1 peptide. Rates are elevated above inorganic nucleation above Ω = 15.2 and inhibited below. In all plots, experiments that showed no nucleation are represented by 'zeros' on the x-axis. The shaded blue region represents Ω values found in the coral calcifying space.

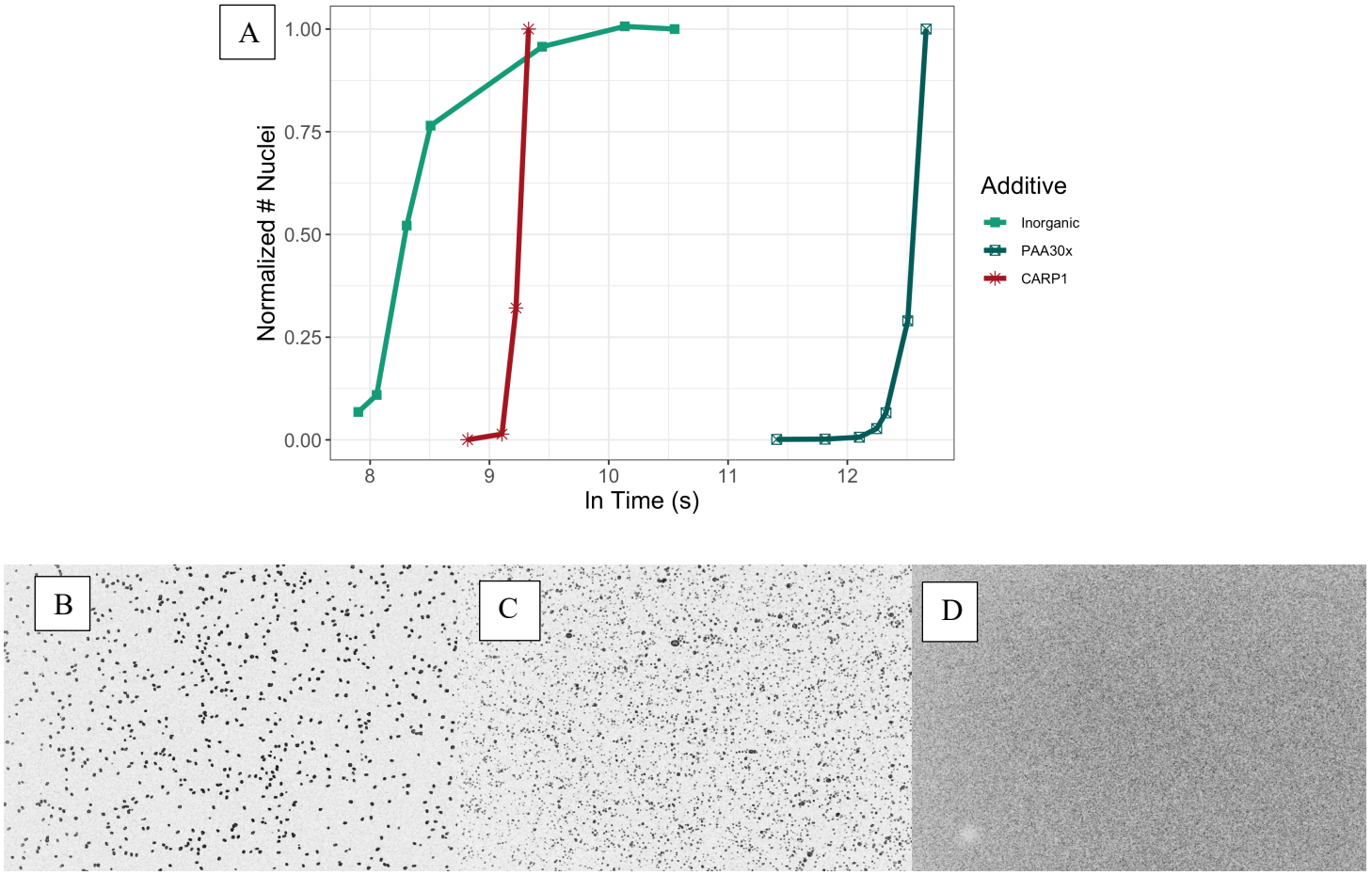

Figure 3.2. (A) Representative rate plots of nucleation experiments normalized to total number of nuclei in individual experiments. Note the log scale on the x-axis. Microscope images of nucleation during experiments with (B) inorganic nucleation, (C) PAA30x, and (D) CARP1 peptide. In each experiment, $\Omega = 106.37$ and the timepoint is at the end of the experiment. Dark spots indicate nuclei. In (D), the nuclei are so dense they are covering the entire image and the lighter background color is not visible.

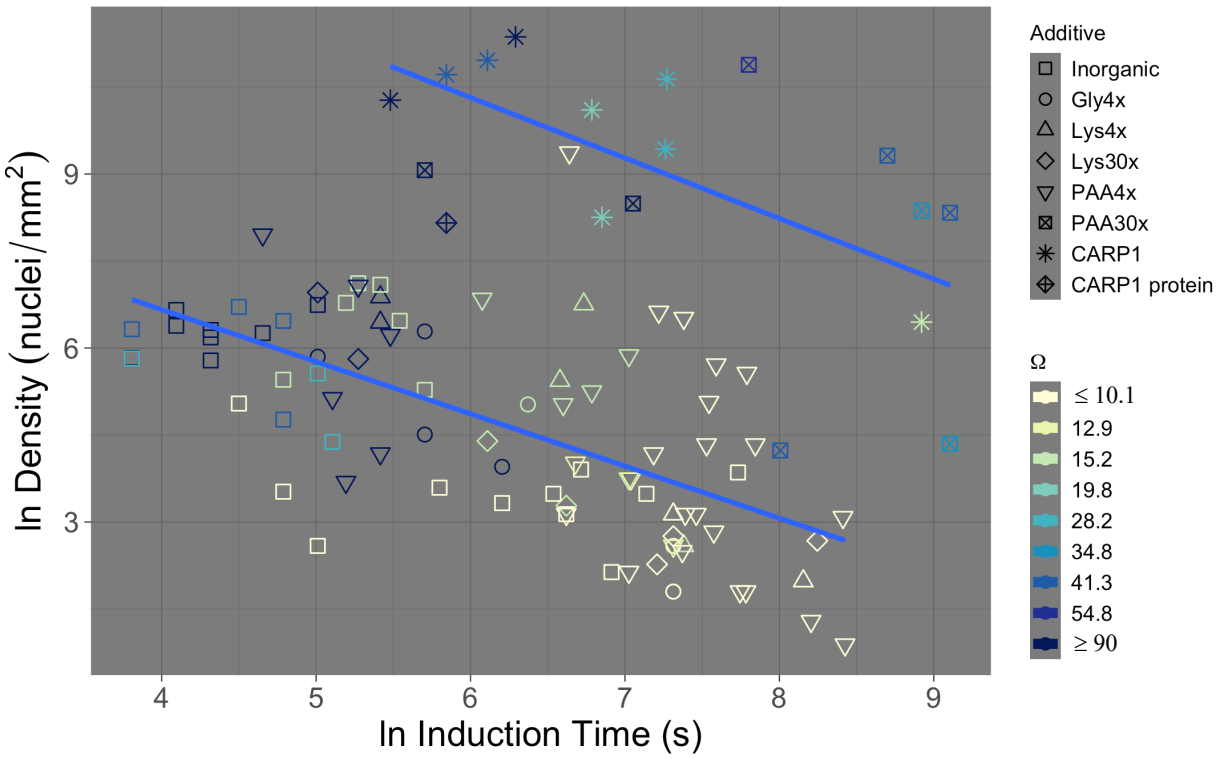

Figure 3.3. The relationship of ln induction time and ln density is shown. The color scale represents Ω, but note that the scale is not linear. In addition, Ω values of 10.1 or lower and 90 or higher have been binned together. The date fall into two groups: the bigger contains inorganic, Gly4x, Lys4x, Lys30x, PAA4x, and CARP1 protein nucleation, while the other group contains PAA30x and CARP1. These data points are translated towards higher induction times and densities. The blue lines are lines of best fit for inorganic nuclei (bottom, slope = -0.46) and CARP1 and PAA30x (top, slope = -0.36).

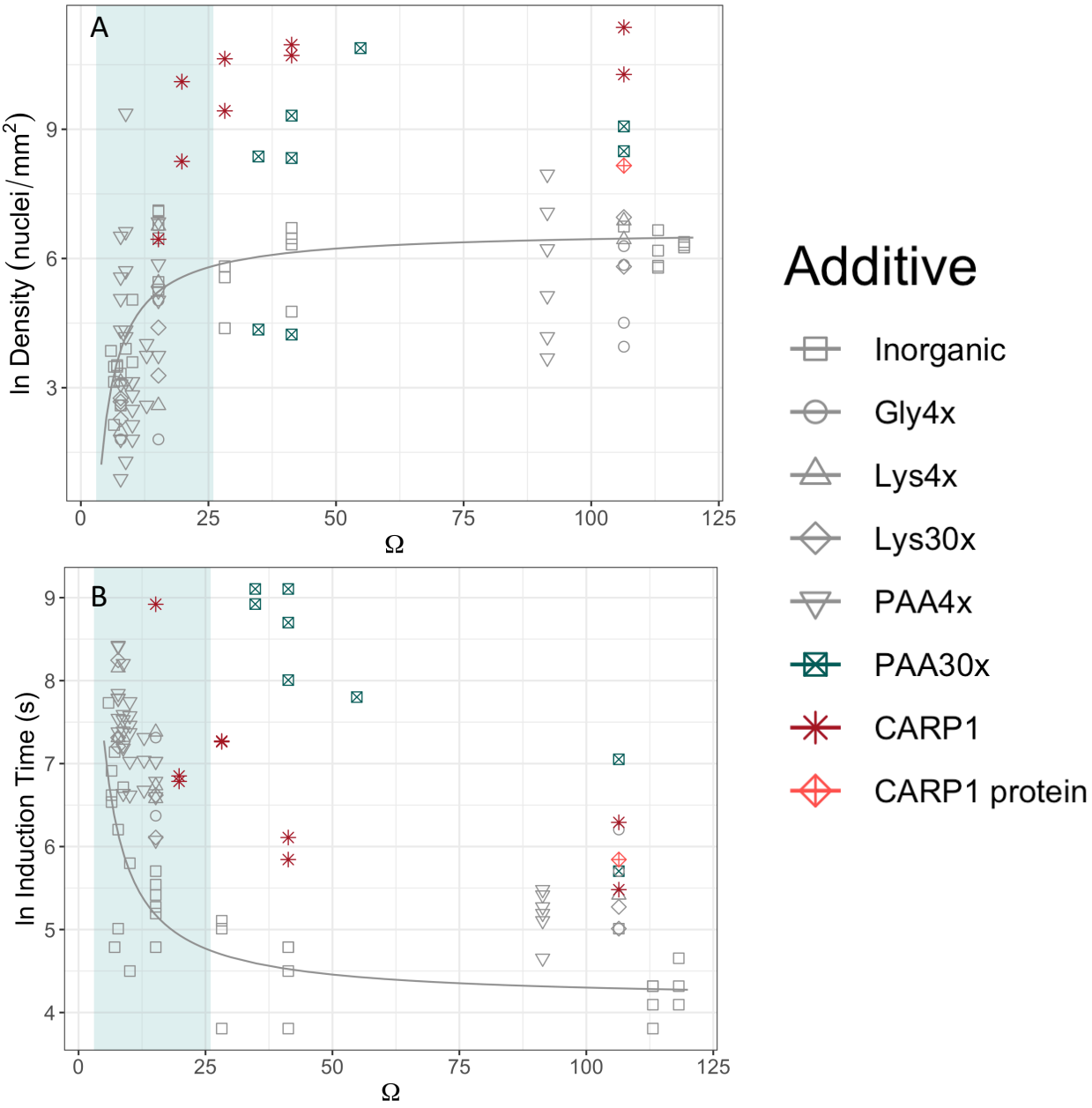

Figure 3.4. Plots showing ln density (A) and ln induction time (B) region of Ω values that are likely to be found in the calcifying fluid in corals. PAA30x and CARP1 values are shown to highlight that they have both higher densities and higher induction time across the range of Ω values. These additives have the same curve shapes as inorganic nucleation (gray lines), but have steeper slopes in the region relevant to corals (CARP1) or are completely inhibited in the region relevant to corals (PAA30x). All other additives have similar values to the inorganic line.

3.9 SUPPLEMENTAL TABLES

Table 3.7. Concentration of Additives in Trial Solutions

Additive	Concentration (μM)
Gly4x	2.825
Lys4x	2.825
Lys30x	0.377
PAA4x	2.825
PAA30x	0.377
CARP1 peptide	0.1
CARP1 protein	0.1

Table 3.8. Experimental Results for Trials Testing Additive Concentration Effects

Additive	Concentration Relative to Main Experiments	Ω	Induction Time (s)	Density (nuclei/m^2)	Ln J (nuclei/m^2/s)
PAA4x*	10x	15.2	1125	354.64	12.24
PAA4x*	10x	15.2	435	939.24	13.33
PAA4x*	10x	7.8	4500	21.79	9.31
PAA4x*	10x	7.8	2400	6.05	8.29
PAA4x*	2x	15.2	1125	42.36	12.80
PAA4x*	2x	15.2	735	152.51	12.43
PAA4x*	2x	7.8	1605	674.17	12.58
PAA4x*	2x	7.8	2415	261.44	11.36
PAA4x*	2x	7.8	4560	2.42	6.41
CARP1	.1x	106.4	540	1972.89	14.98
CARP1	.1x	106.4	450	265.07	14.18

*Means that experimental results were included in figures in main paper

3.10 SUPPLEMENTAL FIGURES

A.

TEGDHLKPGHSEDEHDEDEHDEEMADHADEQNPADEEETEDEEKDDDKM

EDDSDDDEEDESQGDDEGEDENDQSHLEHDAFLGD

B.

MFHSWWMTLLILGSTVSFVFTEGDHLKPGHSEDEHDEDEHDEEMADHAD

EQNPADEEETEDEEKDDDKMEDDSDDDEEDESQGDDEGEDENDQSHLEH

DAFLGDNYTEFKGLSPEDAKTKLAQLIKDEVDLNKDGVLTEDEIRQRFHV

TTKEYRKKEVMETMKQHDEDKDGKVSWEEFKKGHFSDDGKDEDAKEQ

MKEDEEKFKFADEDGDGKLDLEEYMAFYHPGDNPRMTEFTIEDSLKKHD

KDKDGQVSKKEFLATFSDVNDDAKEEMEKDFNNNFDKDKNGRLNKEEM

KSWLFPDDDFSTEEPKTLIKEADEDKDGKLTMDEIMKNYKVFIEDEPEDSS

HDEL

Figure 3.5. CARP1 peptide (A) and full protein (B) sequences, with the peptide sequence highlighted in the full protein sequence (35).

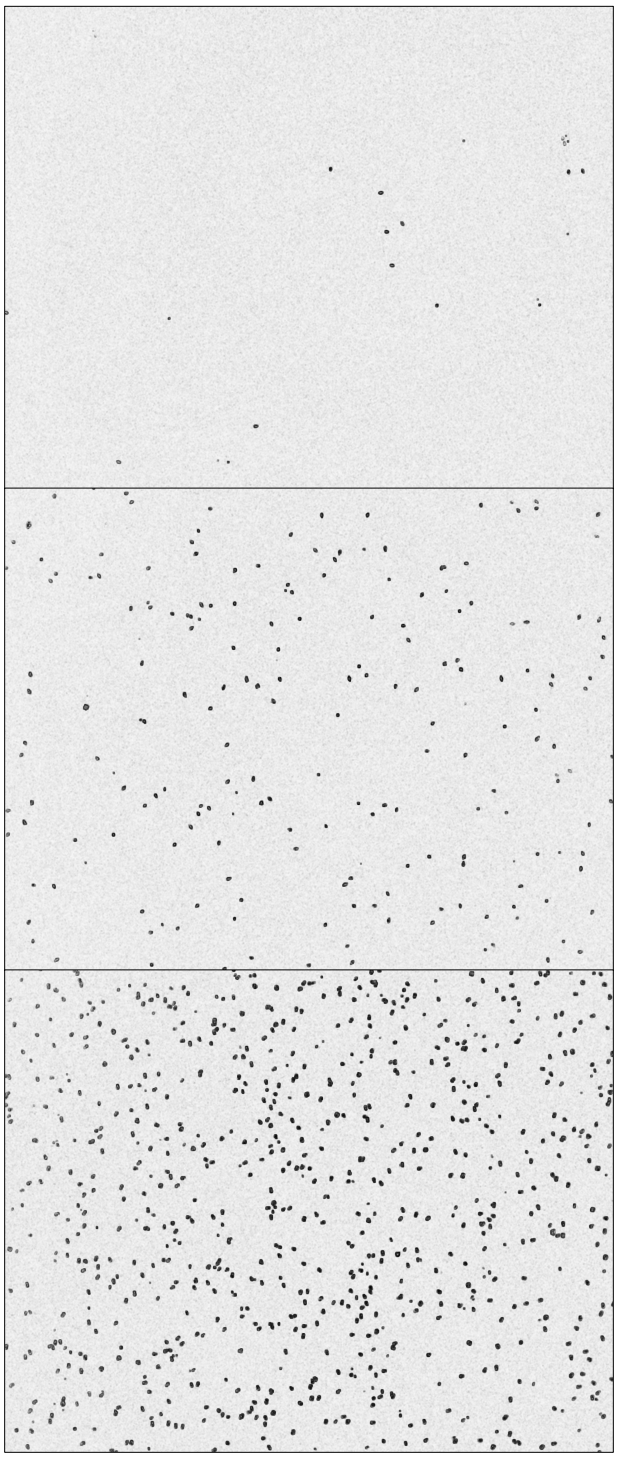

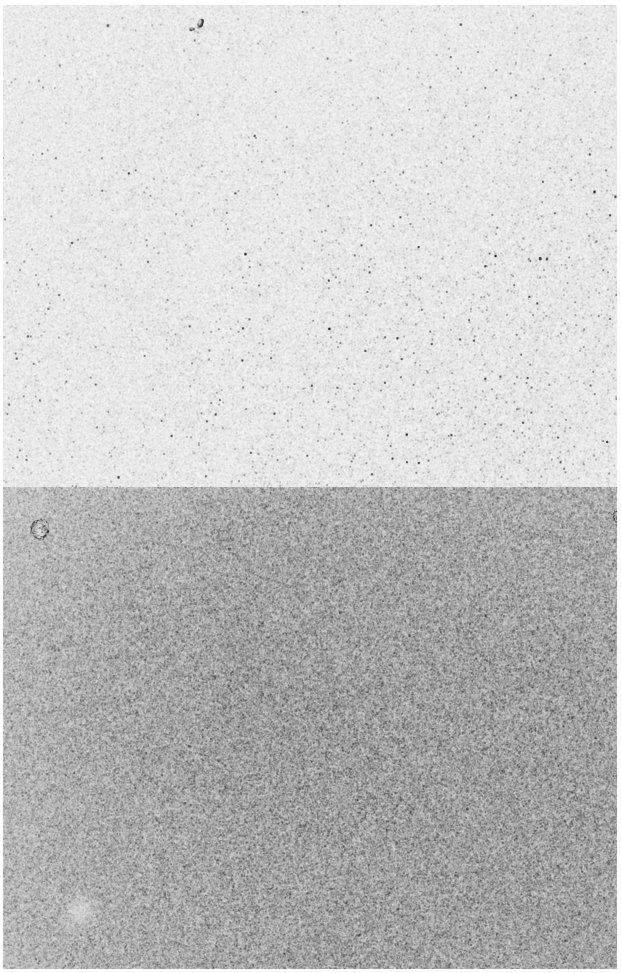

Figure 3.6. Microscope images of nuclei at the end of inorganic experiments at Ω values of (A) 7.76, (B) 15.2, and (C) 106.4. Images from experiments with the additive CARP1 at Ω values of (D) 19.6 and (E) 106.4. Dark spots are nuclei. For CARP1 experiments, nuclei are smaller and denser. There are so many nuclei in E that they cover the image entirely.

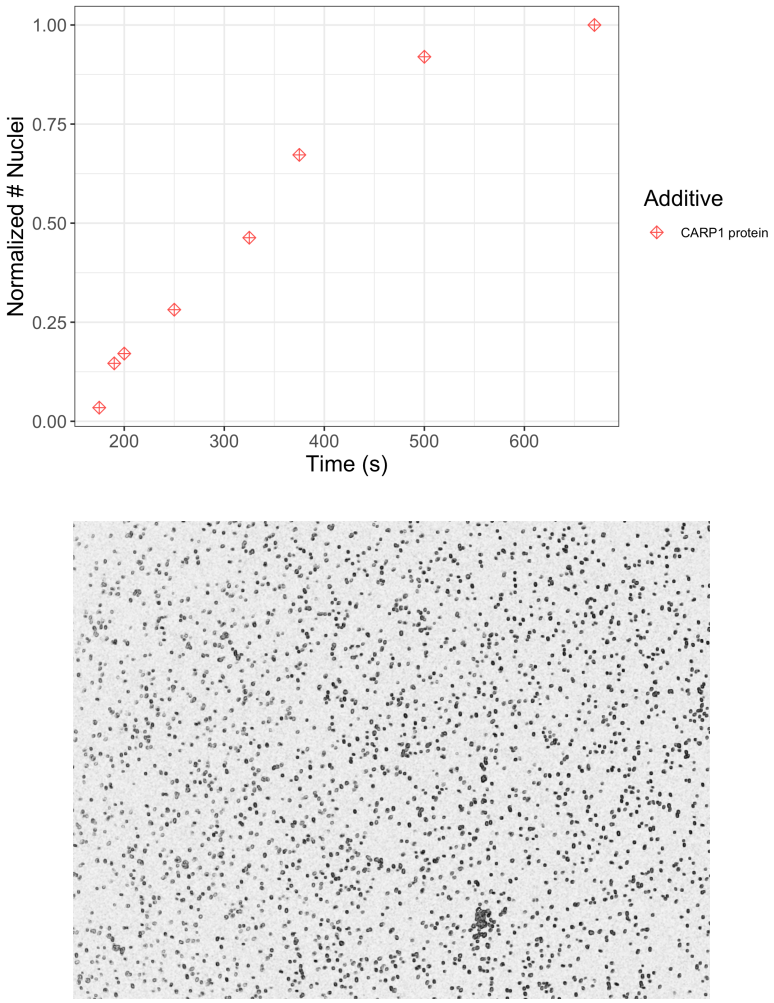

Figure 3.7. Growth curve with time for CARP1 protein. Nucleation is linear with time. As compared with growth curves for CARP1 peptide and inorganic nucleation (Figure 3.2A), this growth curve has a similar shape to inorganic nucleation.

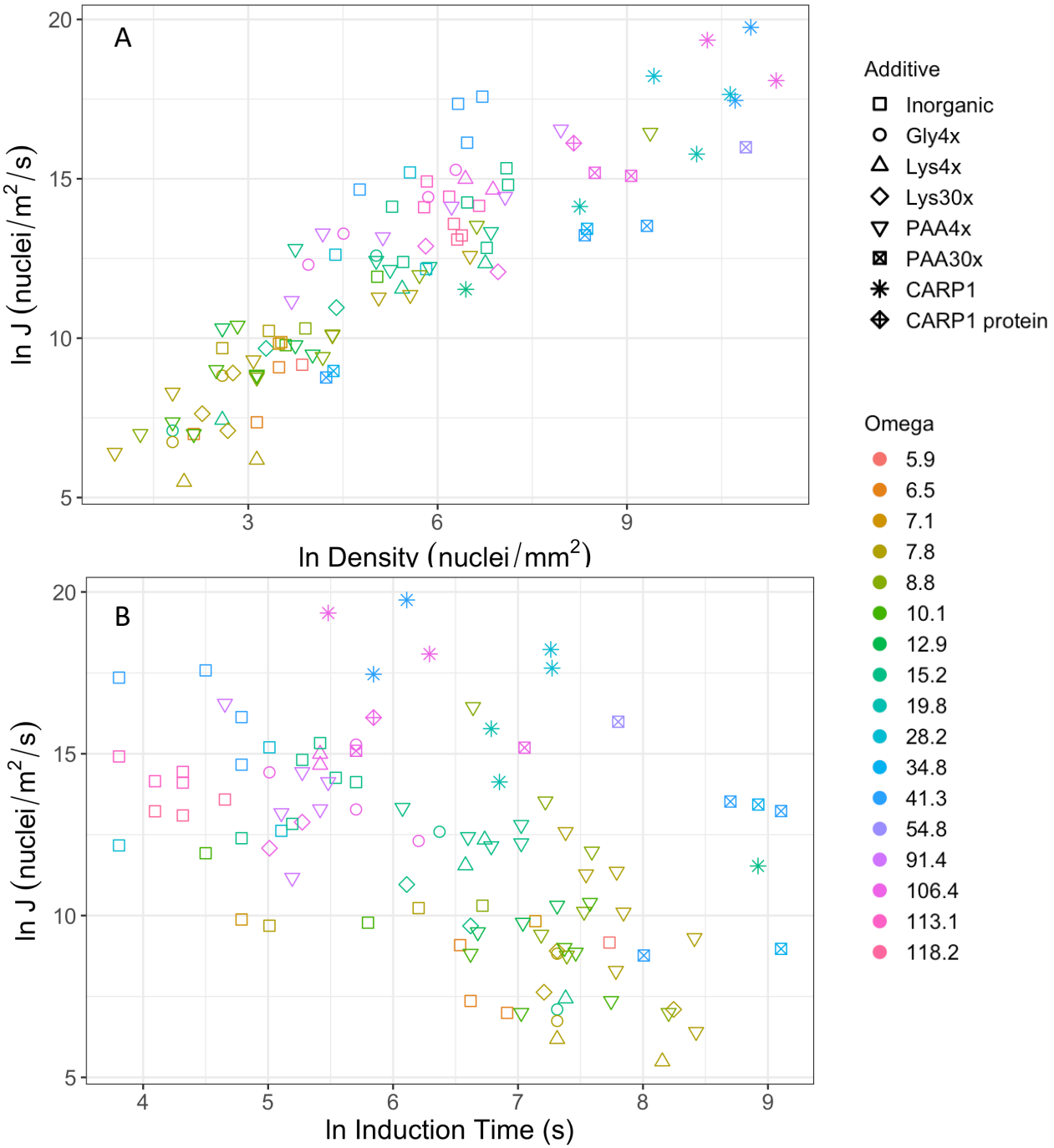

Figure 3.8. Plots showing the relationship of ln J with ln density (A) and induction time (B). The color represents Ω - note that the scale is not linear. The linear relationship between ln density and ln J is expected given that nucleation rate is a function of density. The relationship between ln induction time and ln J has similar patterns to the relationship between ln induction time and ln density. The CARP1 and PAA30x values are separated in space from all other data points (higher induction times and higher rates), but the difference is not as great as for the density and induction time plot.

Chapter 4. $^{2}H/^{1}H$ FRACTIONATION IN MICROALGAL LIPIDS FROM THE NORTH PACIFIC OCEAN: GROWTH RATE AND IRRADIANCE EFFECTS

4.1 ABSTRACT

[1]The hydrogen isotope ratio ($^{2}H/^{1}H$) of microalgal lipids has become a useful tool for reconstructing hydrologic conditions in the geologic past from marine and lacustrine sediments. Culture studies have shown that, in addition to the $^{2}H/^{1}H$ ratio of growth water, parameters such as salinity, growth rate, and irradiance, can have a large effect on lipid $^{2}H/^{1}H$ ratios. But aside from salinity, these effects have not been well studied in the field. In this work, hydrogen isotope fractionation relative to growth water was measured in four algal lipids - $C_{37:3}$ and $C_{37:2}$ methyl alkenones, (3β,4α,5α,22*E*)-4,23-Dimethylergost-22-en-3-ol (dinosterol), and 24-methylcholesta-5,22E-dien-3β-ol (brassicasterol) – in the upper water column of two North Pacific Ocean locations. By comparing lipid $^{2}H/^{1}H$ variations as a function of depth at tropical Station ALOHA (22°45'N, 158°00'W) and mid-latitude Gyre (41°30'N, 132°00'W in the Transition Zone) it was possible to evaluate the H isotope effects of nutrient limitation and irradiance on natural phytoplankton populations by comparing measured fractionation factors (α_{lipid}) with those derived from laboratory-based empirical relationships. Significant distinctions were observed between the inferred causes of H isotope fractionation in different algal lipids at the two locations. At Station Aloha, $^{2}H/^{1}H$ fractionation in coccolithophorid-derived alkenones was primarily caused by

[1] A version of this chapter has been published as M. Wolfshorndl, R. Danford, and J.P. Sachs. $^{2}H/^{1}H$ fractionation in microalgal lipids from the North Pacific Ocean: Growth rate and irradiance effects. Geochimica et Cosmochimica Acta, 246, 2019.

nutrient-limited growth, while at Gyre it was caused by light limitation. Distinctions were less clear for the two sterols. $^{2}H/^{1}H$ fractionation in dinosterol was possibly influenced by nutrient-limited growth or light limitation at greater depths at both stations, while $^{2}H/^{1}H$ fractionation in brassicasterol matched values expected for nutrient-limited growth at both locations. Although systematic trends with depth in α_{lipid} on the order of 10-30‰ were observed for each lipid, inter-day variability was some 3-7‰ depending on the lipid and site, and the magnitude of α_{lipid} changes observed in the field were much less than those expected based on culture studies. This implies that the effects of nutrient and light limitation on natural phytoplankton populations in the ocean may not have a large influence on hydroclimate reconstructions based on $^{2}H/^{1}H$ ratios of microalgal lipids in marine sediments.

4.1 INTRODUCTION

The stable hydrogen isotope ratio ($^{2}H/^{1}H$) in microalgal lipids has become a useful tool for reconstructing hydrologic conditions in the geologic past because this proxy can be used globally – in high and low latitudes, marine and continental settings—most anywhere microalgae occur (92–101). Lipids produced by phytoplankton reflect the $^{2}H/^{1}H$ ratio of environmental water in a near perfect relationship (102, 103). The hydrogen isotopic composition of environmental water is in turn linked to the hydrologic cycle, influenced by the relative amounts of rainfall and evaporation that occur (104–106). Isotope notation expresses this ratio relative to a standard as:

$$\delta^{2}H_{lipid}=[(^{2}H/^{1}H)_{lipid}/(^{2}H/^{1}H)_{standard}-1]*1000 \qquad \text{(Equation 4.1)}$$

where $(^{2}H/^{1}H)_{standard}$ is the Vienna Standard Mean Ocean Water value. The relationship between the $^{2}H/^{1}H$ ratio in the lipid and that of the water in which the algae grew is expressed as the apparent fractionation factor:

$$\alpha_{lipid}=(^{2}H/^{1}H)_{lipid}/(^{2}H/^{1}H)_{water} \qquad \text{(Equation 4.2)}$$

Lipids and other biosynthetic products are typically depleted in ^{2}H relative to environmental water owing to normal isotope effects associated with enzyme-mediated reactions (107). Because different organisms can impart varying amounts of $^{2}H/^{1}H$ fractionation to the same biosynthetic product under similar growth conditions (103), well-constrained paleoclimate interpretations are usually derived from source-specific lipids.

Recently, multiple culture and field studies have demonstrated a systematic linear increase in α_{lipid} (increase in $\delta^{2}H_{lipid}$) of 1 to 2 ‰ ppt^{-1} in the lipids from phytoplankton as salinity increases (108–115). While this provides the foundation for reconstructing paleosalinity, other parameters can change the $\delta^{2}H$ value of algal lipids, independent of salinity and $\delta^{2}H_{water}$. For example, culture studies have demonstrated α_{lipid} effects caused by temperature (116–118), growth phase (108, 117), growth rate (113, 118–120), and irradiance (121, 122) in a variety of microalgal taxa.

Growth rate and irradiance, in particular, have been shown to exert a large influence on $\delta^{2}H_{lipid}$, but have not been widely studied, particularly in the field. We present $\delta^{2}H$ data from four microalgal lipids in the euphotic zone at two North Pacific Ocean locations to examine the effects of growth rate and irradiance on $\delta^{2}H_{lipid}$. The four lipid compounds we target are the $C_{37:3}$ and $C_{37:2}$ methyl alkenones, (3β,4α,5α,22*E*)-4,23-Dimethylergost-22-en-3-ol (dinosterol), and 24-methylcholesta-5,22E-dien-3β-ol (brassicasterol). C_{37} alkenones are long chain ketones with varying degrees of unsaturation that are known to be produced exclusively by several members of the division Prymnesiophyta, and in the open ocean, almost exclusively by the coccolithophores *Emiliania huxleyi* and *Gephyrocapsa oceanica* (123–125), making them a near species-specific biomarker. Dinosterol is a compound produced in large amounts by many species of dinoflagellates, but is unusual in other marine phytoplankton (126–128), and is therefore reasonably considered a taxon-specific biomarker where dinoflagellates are known to occur.

Brassicasterol is produced by a number of species of diatoms, in particularly high amounts by pennate diatoms (129), some species of dinoflagellates, and is the major sterol produced by several members of the Prymnesiophyta, including *E. huxleyi* (127, 130). It has been shown to be produced in several other taxa as well and is therefore a general marine algal indicator.

C_{37} alkenones have been particularly well studied in culture because of their source specificity and their widespread use in the $U^{k'}_{37}$ sea surface temperature (SST) proxy (c.f., Prahl and Wakeham, 1987), based on the abundance ratio of di- and tri-unsaturated varieties. Alkenone δ^2H measured from *E. huxleyi* grown in continuous culture under N-limited conditions displayed a negative correlation with growth rate of between 25 and 55‰ $(d^{-1})^{-1}$ (119). All growth rate measurements reported here are in units of specific growth rate, rather than division rate, regardless of how they were originally reported. Batch culture measurements of alkenone δ^2H from *E. huxleyi* and *G. oceanica* where temperature and salinity were putatively controlling growth rate indicated an even greater sensitivity of ~58‰$(d^{-1})^{-1}$ and ~144‰$(d^{-1})^{-1}$, respectively for the two species (113).

Furthermore, a batch culture study with *E. huxleyi* by van der Meer et al. (2015), in which irradiance levels controlled growth rate, showed a positive correlation between irradiance and $\delta^2H_{alkenone}$ of 0.2 ‰ per µmol photons m^{-2} s^{-1} at sub-saturating light (less than 100 or 200 µmol photons m^{-2} s^{-1}, hereafter µmol m^{-2} s^{-1}) (121). Above those irradiance levels no change in fractionation occurred (up to 600 µmol m^{-2} s^{-1}). with cultures grown in a 16:8 hour light:dark cycle. Thus, the two drivers of $^2H/^1H$ fractionation that have been observed in culture studies – (1) growth rate limited by nutrients, temperature and salinity, and (2) irradiance level or growth rate controlled by irradiance level – cause opposing $^2H/^1H$ fractionation effects in the same lipids (alkenones) produced by the same species. The ultimate driver of H isotope fractionation in both cases must be biosynthetic in origin, with several possible mechanisms discussed below. But

neither empirical observations nor the theory of isotope-physiology in microalgae are sufficiently advanced to explain and quantify these effects fully.

There have been fewer culture studies investigating the impacts of growth rate and irradiance on fractionation imparted to other microalgal lipids, such as sterols. Zhang et al. (2009) observed greater $^{2}H/^{1}H$ fractionation (lower α_{lipid} values) at higher growth rates in a sterol from the marine diatom *Thalassiosira pseudonana* grown in continuous culture under nutrient-limited vs nutrient-replete conditions (118). In continuous cultures with the same species and sterol, Sachs and Kawka (2015) also observed greater $^{2}H/^{1}H$ fractionation (lower α_{lipid} values) with increased growth rate, amounting to ~29 ‰ $(d^{-1})^{-1}$. In continuous cultures with *E. huxleyi* the sensitivity was even greater, amounting to 63‰ $(d^{-1})^{-1}$ for brassicasterol (119). Thus, as with alkenones, though few in number, all studies to date indicate that α_{lipid} in sterols decreases ($\delta^{2}H_{lipid}$ decreases) as nutrient-controlled growth rate increases in microalgae. There is at present no data from culture studies on the effects of growth rate limited by temperature or salinity on sterol $^{2}H/^{1}H$ fractionation.

The one study reporting on H isotope effects associated with light, in lipids other than alkenones, found different responses for sterols, as compared to fatty acids and phytol (122). In that experiment, six continuous cultures of *T. pseudonana* were maintained at constant growth rate while these cultures were grown at different sub-saturating irradiance levels. The cultures were grown in 24 hour light, with all irradiance levels below 50 µmol m^{-2} s^{-1}, and were limited by the amount of nitrogen. α_{lipid} and $\delta^{2}H$ values increased with irradiance in phytol and the $C_{14:0}$ fatty acid (by 1.1‰ (µmol m^{-2} $s^{-1})^{-1}$ and by 0.3‰ (µmol m^{-2} $s^{-1})^{-1}$, respectively), but decreased (by 0.8‰ (µmol m^{-2} $s^{-1})^{-1}$) in the sterol 24-methyl-cholesta-5,24(28)-dien-3-ol (122).

The culture studies by van der Meer et al. (2015) and Sachs et al. (2017), while the only ones yet published on the effects of irradiance on $^{2}H/^{1}H$ fractionation in algal lipids, differed

fundamentally in their approach. The study by Sachs et al. (2017) maintained constant growth rates across and during all treatments, so any measured effect on α_{lipid} could reasonably be attributed to photon flux alone. The study by van der Meer et al. (2015), however, used irradiance to control growth rate, making it impossible to isolate the effect of photon flux from the effect of (light-limited) growth-rate. Consequently, we refer henceforth to both the direct effect of photon flux and light-limitation on α_{lipid} using the terms "irradiance" [effect on growth] or "light limitation" [of growth].

More broadly, phytoplankton growth rates can be influenced by several factors in lab and field experiments. As discussed in Müller et al. (2017), nutrient control of growth can occur either via nutrient-starvation, as in batch cultures that capture the transition to the stationary phase of growth, or via nutrient-limitation, as in chemostats that maintain a constant supply of a limiting nutrient to cells growing exponentially--the majority of growth rate experiments cited here (132). Other parameters can also control growth, such as the experiments of Schouten et al. (2006), which used temperature and salinity. The aim of the present study was to compare the effects of growth rate on $^{2}H/^{1}H$ fractionation in algal lipids in the field to experimental results from culture in an attempt to decipher whether irradiance or nutrient limitation was controlling phytoplankton growth in the euphotic zones of two North Pacific locations. Based on available culture data the term "growth rate" in this study will imply nutrient-limited growth rate (as in the chemostat experiments in Sachs et al. (2015)), and phytoplankton at the field sites will be assumed to be in exponential growth. Their $\delta^{2}H_{lipid}$ values will only be compared to studies in which growth rate was also exponential and controlled through nutrient limitation, to exclude obfuscating effects of growth phase and other controls on growth rate.

A single prior study by Wolhowe et al. (2015) reported on the role that light and growth rate may play in determining microalgal δ^2H_{lipid} values in the field (120). That study looked exclusively at alkenones, and found that there was a correlation between decreased α_{lipid} and decreasing irradiance level below ~100 μmol m^{-2} s^{-1}. They found no correlation between fractionation and alkenone-producer specific growth rate as measured through uptake of ^{13}C into alkenones during 24-hour incubations. However, they did not eliminate growth rate as a possible control on α_{lipid}, suggesting in an alternative hypothesis that a 24-hour growth rate estimate is not applicable to an alkenone lipid pool that has a turnover time of days rather than hours. The study, therefore, left open the question of whether light or growth rate is ultimately controlling alkenone α_{lipid} in that setting.

The biosynthetic mechanisms underlying H isotope fractionation in phytoplankton are still being investigated, but certain fundamental concepts have become relatively well accepted. It is generally known that hydrogen in algal lipids is sourced from the cofactor nicotinamide adenine dinucleotide phosphate (NADPH), produced through both photosynthesis and the metabolic oxidative pentose phosphate (OPP) pathway, and from intracellular water. The reduction of $NADP^+$ to NADPH during photosynthesis results in a molecule highly depleted in ^2H, while OPP produced NADPH is relatively enriched in ^2H (133). Intracellular water is even more enriched compared to NADPH from either source because it is assumed to have nearly the same δ^2H as the environmental water. The δ^2H_{lipid} value is therefore a product of mixing of these three different sources of hydrogen. Explanations for the depletion of ^2H at higher growth rates conclude that more hydrogen is sourced from photosynthetic NADPH under higher growth conditions because it is more depleted in ^2H, while more OPP-derived NADPH is included in lipid synthesis during low growth conditions (111, 114, 119, 134).

In the case of irradiance, the explanations are more complicated because, from the existing culture studies, alkenones and sterols have opposite fractionation responses to irradiance level, as opposed to growth rate-driven fractionation, which appears to have a universal response across different lipids. Sachs et al. (2017) discussed the mechanisms of light effects on δ^2H_{lipid} in chemostat cultures of the diatom *T. pseudonana*. For sterols, which displayed a decrease in δ^2H as irradiance increased, they invoked the two pathways of sterol production, the methylerythritol phosphate (MEP) pathway in the chloroplast and the mevalonic acid (MVA) pathway in the cytosol, which have different fractionation effects. They hypothesized that the relative contribution of the MEP pathway increases as light increases, while the MVA pathway contributions decreases, causing the observed $^2H/^1H$ fractionation response. While Sachs et al. (2017) cultured a diatom that did not produce alkenones (i.e., only certain prymnesiophytes produce alkenones), they did measure an increase in the δ^2H value of the C14:0 fatty acid (myristic acid) as irradiance increased, the same response observed in alkenones from batch-cultured *E. huxleyi* by van der Meer et al. (2015). Fatty acids are synthesized along the acetogenic pathway in cells, the same as alkenones, so a biosynthetic source of fractionation would theoretically apply to both lipids. Sachs et al. (2017) attributed this fractionation response to changing intracellular sources of pyruvate, an intermediate in metabolic pathways that is incorporated into acetogenic lipids, as irradiance levels varied, and the likelihood that different pools of pyruvate have different δ^2H values. Additional culture studies are needed before a comprehensive theory to explain irradiance effects on $^2H/^1H$ fractionation in algal lipids is possible.

Given our rudimentary knowledge of the effects of light and growth rate on α_{lipid} in microalgae, and the small number of laboratory studies aimed at addressing these effects, we sought to evaluate the role that both light and growth rate played in setting δ^2H values of a

variety of microalgal lipids within the euphotic zone at two oceanographically distinct locations in the North Pacific Ocean--Station ALOHA north of Oahu, Hawaii (hereafter called "Aloha") and in the transition zone at 42°N in the Northeast Pacific (hereafter called "Gyre"). These two sites were selected based on the supposition that they represented algal growth under both light- and nutrient-limiting conditions at Aloha (135) as opposed to just light-limiting conditions at Gyre, and the likelihood that neither temperature nor salinity would cause significant α_{lipid} changes in the water column. Previous work at Gyre concluded that irradiance was the predominant factor influencing growth rate of alkenone-producing algae (136). By measuring the δ^2H value of water, alkenones, dinosterol, and brassicasterol, and quantifying lipid-specific growth rates for each compound with a ^{13}C-labeling approach (136, 137), we sought to determine the extent to which the H-isotope fractionation effects associated with light and growth rate differences in cultured microalgae were observed in the field. We found that trends with depth in the water column for all lipids could be explained by one or both of nutrient-limited growth rate or light limited effects, but the magnitude of changes were comparable to inter-day variability at each depth and were smaller than the predicted fractionation changes measured in culture studies.

4.2 METHODS

4.2.1 *Site Descriptions*

Samples for this study were collected at two Pacific Ocean sites: Gyre (41°30'N, 132°00'W) in the Northeastern Pacific Ocean and the Hawaii Ocean Time-Series (HOT) Station ALOHA (22°45'N, 158°00'W) (Supplementary Figure 6). This study evaluated suspended particles, water,

and hydrographic properties measured with a CTD (conductivity temperature depth) instrument from February 25 and 27, 2012 at Aloha, and July 18 and 20, 2012 at Gyre.

The Gyre site is located in the transition zone between the California Current coastal system, the central North Pacific oligotrophic gyre, and the Subarctic Domain (Hickey, 1979). The California Current is an eastern boundary current that carries cold, low-salinity water south into the tropical Pacific, and Northerly winds along the coast provide consistent upwelling and subsequent nutrient-enriched waters, particularly in summer north of 40°N (138, 139). This is in stark contrast to the nutrient-deficient surface waters of the North Pacific gyre. The surface water north of 40°N is typically of subarctic origin, characterized by low temperature and salinity (140). Based on a measured salinity of 32.8 during sample collection the site was just within the Subarctic Domain from a physical oceanography perspective (141). The average chlorophyll concentration during the cruise was 0.19 µg/L, just below the 0.2 µg/L chlorophyll concentration limit defined by Polovina et al. (2001) for the Transition Zone Chlorophyll Front (142), a biological definition.

Transition-zone phytoplankton communities have been shown to be diverse and distinct in behavior from communities in surrounding zones (143), but have been poorly characterized on a species or taxa level. Since the Gyre site is influenced by the Subarctic Domain, which has a better documented plankton assemblage than the transition zone, we describe that here. The phytoplankton community composition at Ocean Station Papa in the subarctic Pacific (50°N, 145°W) has been well documented to the taxonomic level (144), indicating no systematic changes of taxa with depth (145). The nanophytoplankton community has been described at the species level at a line between 125°30.0 W and 145°W at between 48 and 50°N and in the entire basin of the subarctic North Pacific by Taylor and Waters, (1982). While they observed that diatoms are the dominant taxa across the basin, particularly in the Western region, flagellates and

coccolithophores predominate the biomass at the station closest to the Gyre site at 130 °W. *E. huxleyi* was the dominant coccolithophore measured at all depths across all stations in their study (146). Further supporting their assessment, the coccolithophore assemblage has been described along five east-west and north-south transects in the north and central Pacific, indicating that at 40°N, and in the subarctic zone in general, *E. huxleyi* is the predominant species throughout the euphotic zone (147, 148).

The Station Aloha Pacific site has been documented extensively through the Hawaii Ocean Time-series (e.g. (149)). Historically the site, as representative of the North Pacific oligotrophic gyre, is nutrient-limited, with nitrate concentrations below detection levels in the surface layer (149). There is a deep chlorophyll maximum layer (DCML) at or just above the nutricline, usually at around 100-120 m (149). Phytoplankton vertical assemblage has been well described for the central North Pacific (150, 151), and has been compared to the phytoplankton assemblage at Station Aloha (152), showing that there is statistically little or no difference between the sites. There is a vertical shift in phytoplankton composition in the euphotic zone that is dominated by two groups, in the surface and deep euphotic zone, with the transition occurring between 100-135 m (152). Characterization of nano- and microphytoplankton at this site (taxa >5 μm) indicates that the largest ecologically distinct group of phytoplankton found primarily above 90 m is made up of coccolithophores, and the group found primarily below 100 m is made up of diatoms and distinct species of coccolithophores. A dinoflagellate species is associated with the shallow group, and the main difference between the two groups is the relative predominance of diatoms and coccolithophores (150). The coccolithophore community with depth at Aloha has also been described in multiple studies, indicating a vertical shift in dominant species with depth, but with

E. huxleyi present at all euphotic zone depths, and little representation of *G. oceanica* (135, 137, 153).

4.2.2 *Large Volume Filtration Samples*

The Gyre (15-20 July 2012, *R/V Point Sur*) and Aloha (23-27 February 2012, *R/V Thompson* Cruise 276) cruises sampled suspended particulate matter throughout the euphotic zone at depths of 15, 25, 35, 45, 55, and 65; and 10, 25, 50, 70, 95, and 120 meters respectively. Sampling protocols were adapted from those described in Prahl et al. (2005).

Suspended particulate matter from each depth was collected onto pre-combusted 142 mm i.d. Whatman GF/F filters with a 0.7 μm nominal pore diameter from water that was brought to the surface by Niskin bottles on the CTD-rosette. Three to five large-volume filtrations (LVF) were conducted continuously from 09:00 to 22:00 each day. Conductivity, temperature, dissolved oxygen, fluorescence, and photosynthetically active radiation (PAR) measurements were performed with a CTD (Sea-Bird Electronics) during each hydrocast. CTD data was analyzed with Sea-Bird Electronics Data Processing software.

4.2.3 *^{13}C Incubation*

Seawater from each depth was collected before dawn each day and incubated in situ for 24 hr with ^{13}C-labeled $NaHCO_3$ in order to determine the growth rate of phytoplankton communities, according to the method of (136). Aliquots of seawater from each depth were treated with $HgCl_2$ at a concentration of 0.00167 mol/L for subsequent measurement of the $\delta^{13}C$ value of natural (unlabeled) DIC. 100 L of water from each depth was inoculated with ^{13}C-labeled sodium bicarbonate ($NaHCO_3$) to attain a $\delta^{13}C_{DIC}$ value of ~200‰. The bottles were placed at the corresponding depth of collection just before sunrise on a free-floating array. After 24 hr, the

bottles were collected, immediately treated with $HgCl_2$ to halt biological activity, and filtered through Whatman GF/F filters. Filters were stored at -20°C until processing.

4.2.4 *δ^2H_{water} Measurements*

Water samples collected from the filtrate of the LVF samples were analyzed using a Picarro L2130-I Isotopic Liquid Water Analyzer (Picarro, Inc., Santa Clara, CA) in high precision mode. Each sample was measured six times, with the first three measurements discarded to avoid memory effects, and normalized to Vienna Standard Mean Ocean Water (VSMOW) using three in-house lab standards with δ^2H_{water} values of -4.28 ± 0.18‰, -54.54 ± 0.11‰, and -105.49 ± 0.32‰. The last three corrected measurements were averaged, and the uncertainty reported as the standard error of those measurements.

4.2.5 *Lipid Purification*

Filters were freeze-dried for 24 hours and cut into small fragments of approximately 0.5 x 2 cm. Lipids were extracted with an accelerated solvent extractor (ASE-200, Dionex Corp., Sunnyvale, CA, USA) at 1500 psi and 100°C for three five-minute cycles with a 9:1 mixture of dichloromethane (DCM) to methanol (MeOH) yielding a total lipid extract (TLE). Solvent was evaporated from the TLE under a stream of nitrogen using a Turbovap system (Caliper, Hopkinton, MA, USA).

The TLE was saponified with 1N KOH at 70°C for 5-12 hours. The lipids were then extracted with hexane at pH 2. The saponified TLE was separated into neutral, acid, and polar fractions using hand packed solid phase extraction (SPE) columns containing 0.5 g 5% aminopropyl silica gel (Supelco/Sigma Alrich, St. Louis, MO, USA, 45 μm, 60 Å, Part #5-7205). The neutral

compounds were eluted in 8 mL of a 3:1 mixture of DCM to isopropyl alcohol (IPA). Acids were eluted using 8 mL 5% acetic acid in diethyl ether. The polar fraction was eluted with 6 mL MeOH. A combination of silica gel columns and High Performance Liquid Chromatography (HPLC) was used to isolate alkenones and sterols from the neutral fraction. Fatty acids were methylated by dissolving the samples in a solution of 1 mL hexane and 2 mL 10:1 MeOH:acetyl chloride and heated for 12 hr at 60°C followed by liquid-liquid extraction with hexane before further analysis. A pthalic acid standard of known isotopic composition (δ^2H = -95.5 ± 2.2‰, $\delta^{13}C$ = -11.5 ± 0.1‰, Dr. Arndt Schimmelmann, Indiana University) was methylated in identical fashion to determine the isotopic composition of the methylating agent.

Hand packed SPE columns containing 1 g 5% deactivated silica gel (EMD Chemicals, Rockland, MA, USA, 35-75 μm, 60 Å) were used to separate the neutral fractions collected from the aminopropyl columns into hydrocarbon, ketone/ester, alcohol, and polar fractions. Hydrocarbons were eluted with 6 mL hexane, ketones and esters were eluted with 6 mL 1:1 hexane:DCM, alcohols were eluted with 8 mL 4:1 hexane:ethyl acetate (EtoAc), and polar compounds were eluted with 6 mL MeOH. Midway through the study, the methods were streamlined and the silica gel purification step was removed, allowing for HPLC purification of the neutral fraction directly after aminopropyl-based separations. Half of the Gyre samples and all of the Aloha samples were purified using this simpler method.

Reverse-phase (C18) HPLC was used to purify alkenones, brassicasterol, and dinosterol from the neutral aminopropyl gel fractions and alcohol silica gel fractions, as described in Nelson and Sachs, (2013). Prior to HPLC, samples were acetylated with 20 μL pyridine and 20 μL acetic anhydride with a known δ^2H and $\delta^{13}C$ value for 30 min at 70°C. HPLC purifications were conducted with an Agilent 1100 HPLC-MSD using a 4.6 mm ID C_{18} column (Agilent, ZORBAX

Eclipse XDB, Santa Clara, CA). The solvent gradient started with 5:95 MeOH:acetonitrile (ACN) from 0-10 minutes, then was ramped up to 5:10:85 MeOH:EtOAc:ACN from 10-20 minutes, and this mixture was maintained until 65 minutes. The solvent mixture was then changed to 100% EtOAc from 65-75 minutes, held from 75-85 minutes, and then changed to 5:95 MeOH:ACN from 85-95 minutes. The column was re-equilibrated with the initial solvent mixture (5:95 MeOH:ACN) from 95-105 mins. Brassicasterol eluted from 28-33.5 minutes, dinosterol eluted from 46-54.5 minutes, and the alkenones eluted from 68-86 minutes.

4.2.6 *Lipid Identification and Quantification*

Compounds were identified with gas chromatography-mass spectrometry (GC-MS) using an Agilent 6890N GC connected to an Agilent 5975 inert mass selective detector equipped with an Agilent VF-17ms column (60 m × 0.32 mm × 0.25 μm; Agilent Tech., Santa Clara, CA) and subsequently quantified with gas chromatography-flame ionization detection (GC-FID) using an Agilent 6890N GC equipped with a programmable temperature vaporization inlet operated in splitless mode with helium carrier gas at 1.6 mL/min onto either a DB-5 ms capillary column (60 m × 0.32 mm × 0.25 μm; Agilent Tech., Santa Clara, CA) or an Agilent VF-17ms column. Compounds were identified by comparing mass spectral and retention time information to those of laboratory standards**.** Lipid abundances were determined by comparing peak areas on GC-FID to that of a 5-**α**-cholestane internal standard with a known mass added to each sample prior to GC-FID analysis.

Dinosterol and brassicasterol were identified and measured in samples at both locations. At Gyre, the primary C_{37} alkenone, and the only one for which δ^2H data were obtainable, was the tri-unsaturated methyl ketone, $C_{37:3}$. At Aloha, the primary alkenone, and the only one for which δ^2H

data were obtainable, was the di-unsaturated methyl ketone, $C_{37:2}$. The α values for each lipid in both locations will hereafter be called α_{Dino}, α_{Brass}, and α_{Alk}. The term α_{Alk} will be used for both Aloha and Gyre samples, referring to either $C_{37:2}$ or $C_{37:3}$, depending on the location.

4.2.7 *Isotope Ratio Mass Spectrometry*

δ^2H values were measured for all lipid samples by gas chromatography-isotope ratio mass spectrometry (GC-IRMS) using a Thermo Delta V Plus IRMS and Thermo Trace GC Ultra, as described in Sachs et al. (2017). In brief, samples were injected in splitless mode at 325°C using helium carrier gas at 1.5 mL/min. For the sterol fractions, the GC was equipped with a VF-17ms capillary column (60 m × 0.32 mm × 0.25 μm). For the alkenone fractions, the GC was equipped with a VF-200ms column (60 m x 0.25 mm x 0.25 μm; Agilent Tech., Santa Clara, CA). Compounds eluting from the GC were pyrolized in a 1400°C ceramic reactor to convert all hydrogen to H_2 prior to introduction to the MS. The H3+ factor was measured prior to every sample sequence and was stable and less than 5.

$\delta^{13}C$ isotope ratios for the ^{13}C-inoculated samples were measured using a separate Thermo Delta V Plus IRMS and Thermo Trace 1310 gas chromatograph. The same GC columns were used for the same compounds on the $\delta^{13}C$ instrument as for δ^2H analysis. After eluting from the GC, samples were combusted into CO_2 gas in a Thermo GC IsoLink II Conversion Unit and transferred to the IRMS using the Thermo ConFlo IV Interface (Thermo Scientific, Waltham, MA). For sterols, the column temperature was held at 120°C for 1 minute, ramped up to 260°C at 20°C per minute, increased to 310°C at 1°C per minute, raised to 325°C at 20°C per minute, and finally held at 325°C for 5 minutes. For fatty acids and alkenones, the initial temperature was 50°C, then the

temperature was increased to 100°C at 20°C per minute, then raised to 240°C at 2°C per minute, and held at 240°C for 15 minutes.

For both instruments, external and internal standards of known hydrogen and carbon isotopic composition, including C_{26}, C_{32}, and C_{38} normal alkanes, were used to normalize measured δ^2H or $\delta^{13}C$ values (standards supplied by Arndt Schimmelmann, Indiana University, Bloomington, IN). δ^2H peak areas less than 12 V s were not considered due to size-dependent δ^2H effects (155), nor were $\delta^{13}C$ peak areas less than 10 V s (or analyte masses less than 40 ng). δ^2H and $\delta^{13}C$ values for acetylated (alcohols) and methylated (acids) lipids were corrected for added C and H via mass balance calculations. Analytical uncertainty of $\delta^{13}C$ values was calculated as the standard error of three replicate injections of a sample.

4.2.8 *Error Analysis of Lipid δ^2H*

Analytical uncertainty of δ^2H values was calculated as the standard error of three replicate injections of a sample. In cases where sample was limited, only one or two injections were performed, in which case the average analytical error for the sample, 5‰, was applied.

Another source of uncertainty resulted from temporal variability, since lipid samples were analyzed from three time points throughout the day. The weighted average, based on the amount of lipids produced at each time point, was calculated to obtain a value for each LVF on each day for each lipid. The temporal uncertainty in lipid δ^2H values averaged 3‰ for $C_{37:3}$ alkenone, 3‰ for dinosterol, and 4‰ for brassicasterol at Gyre. At Aloha, the average temporal uncertainty was 3‰ for dinosterol and 7‰ for brassicasterol. The $C_{37:2}$ samples from different time points from Aloha were combined before analysis, so only analytical uncertainty is reported. The overall uncertainty for other lipids, combining both analytical uncertainty and temporal variability, was

calculated using a Monte Carlo simulation, and propagated through the calculation of α values for each day.

4.2.9 *Growth Rate Estimates*

Lipid-specific growth rates were determined using the ^{13}C-labeling method of Prahl et al. (2005) and Popp et al. (2006a) that was designed to determine growth rates of alkenone-producing microalgae. Further details of the method are reported in Wolhowe et al. (2014) and Wolhowe et al. (2015). Briefly, suspended particles from ^{13}C-incubated seawater arrays were processed as described above for lipid δ^2H analyses. $\delta^{13}C$ measurements were performed on C_{37} alkenones, dinosterol, brassicasterol, $C_{14:0}$ fatty acids, and $C_{16:0}$ fatty acids. Alkalinity and pH measurements of seawater from the incubation bottles were performed to determine the concentration of CO_2 (aq), in order to eventually determine the mole fraction of ^{13}C in CO_2 (aq), which is the F_{DIC} term in Equation 4.3, below (Supplementary Table 2). Alkalinity was measured with a Dosimat auto-titrator electrode and pH was measured using a colorimetric Sunburst AFT-pH sensor. Internal lab standards and Certified Reference Materials (CRMs) were used as calibration standards for both alkalinity and pH measurements. $\delta^{13}C$ of DIC (Supplementary Table 3) was measured by the Stable Isotope Laboratory at the College of Earth, Ocean, and Atmospheric Sciences, Oregon State University by continuous-flow mass spectrometry with a precision of ±0.15‰ using the GasBench-DeltaV system as detailed in Torres et al. (2005). Lipid-specific growth rates were calculated as described by Popp et al. (2006a) and Wolhowe et al. (2015) using Equation 4.3

$$\mu' = \frac{1}{T} \ln \left(\frac{F_{DIC} - F}{F_{DIC} - F_0}\right) \qquad \text{(Equation 4.3)}$$

where μ' equals the specific growth rate, T is time (24 hr), F_{DIC} is the mole fraction of ^{13}C in DIC (CO_2 (aq)), F equals the mole fraction of ^{13}C in alkenones after incubation, and F_0 equals the mole

fraction of ^{13}C in alkenones before incubation. From this equation, $\mu_{C37:2}$ and $\mu_{C37:3}$ were calculated from C_{37} alkenones at Aloha and Gyre, respectively.

Equation 4.3 was also used to determine lipid-specific growth rates for phytoplankton producers of dinosterol, brassicasterol, $C_{16:0}$ fatty acid, and $C_{14:0}$ fatty acid. Popp et al, (2006a) developed and validated this method specifically for alkenone-producing phytoplankton. Although the same culture validation has yet to be done for sterols and fatty acids, the basic assumptions of the method hold for other lipids, namely that the uptake of a tracer into a lipid product is proportional to the uptake of a tracer into the bulk carbon of the single-celled organism, which is proportional to growth of the cell over a period of time. Because no culture-based validations of the method have been performed for lipids other than alkenones, and phytoplankton taxa other than alkenone-producers, we use the growth rate determinations from non-alkenone lipids as estimates only, to determine growth rate trends in the lipid-producing taxa through the euphotic zone, rather than accurate, quantitative measures of in situ growth rates.

4.2.10 *Predicted α Values*

The extent to which euphotic zone δ^2H_{lipid} values at the two North Pacific locations could be attributed to irradiance or nutrient-limited growth rate effects was evaluated by comparing measured α_{lipid} values with those predicted from the continuous culture studies by Sachs and Kawka (2015) and Sachs et al. (2017), and the batch culture study by van der Meer et al. (2015). Growth rates in the former experiments were maintained at constant values by keeping the dilution rate of media with a nitrate-to-phosphate molar ratio of 2 constant. They can therefore be considered N-limited rather than nutrient-starved. The two studies exploring irradiance effects, as stated, did so by either holding growth rates constant during and across treatments (Sachs et al.

(2017), or allowing growth rate to vary as a function of irradiance (van der Meer et al. (2015)). Although these models are not perfect matches for the environmental circumstances of the LVF collections, these measured relationships are the most relevant to the field conditions and the most useful for evaluating the effects of irradiance and growth rate on $^{2}H/^{1}H$ fractionation in algal lipids.

Specifically, the predicted response of α_{Alk} to irradiance (Equation 4.4) was adapted from the linear relationship between α_{Alk} and irradiance below 200 μmol m^{-2} s^{-1} in van der Meer et al. (2015). At water depths where PAR values exceeded 200 μmol m^{-2} s^{-1} , this relationship would presumably not be valid. However, at these saturating irradiances, there would be no expected effect on α_{Alk}, as found by Van der meer et al. (2015). This predicted response of α_{Alk} to irradiance is hereafter referred to as PI - α_{Alk}. The input for Equation 4.4 is noon PAR on the day samples were collected. The predicted H isotope response of dinosterol and brassicasterol to irradiance (Equation 4.5) was adapted from the diatom (*T. pseudonana*) sterol results in Sachs et al. (2017). These values are referred to as PI – α_{Dino} and PI – α_{Brass}. The input for this equation is noon PAR on the day of each LVF.

$$PI - \alpha_{Alkenone} = 0.00025 * PAR + 0.76 \quad \text{(Equation 4.4)}$$

$$PI - \alpha_{sterol} = -0.0008 * PAR + 0.768 \quad \text{(Equation 4.5)}$$

The predicted H isotope response of alkenones to nutrient-limited growth rate (Equations 4.6 and 4.7 for $C_{37:2}$ and $C_{37:3}$ alkenones, respectively) is from Sachs & Kawka (2015; with the units changed to d^{-1} (specific growth rate) from div d^{-1} (division rate)) (119). These predicted nutrient-limited-growth-rate alpha values are referred to hereafter as PN - $\alpha_{Alk.}$ The growth rate estimate input for this equation was $\mu_{C37:2}$ at Gyre (where both $C_{37:2}$ and $C_{37:3}$ were present) based on Popp et al. (2006a)'s work showing that growth rate estimates based on ^{13}C-labeling of the $C_{37:2}$ alkenone are more accurate than those based on $C_{37:3}$ alkenone.

$$PN - \alpha_{C37:2} = -0.025 * \mu_{C37:2}/ln(2) + 0.80 \quad \text{(Equation 4.6)}$$

$$PN - \alpha_{C37:3} = -0.038 * \mu_{C37:2}/ln(2) + 0.82 \quad \text{(Equation 4.7)}$$

The predicted H isotope response of dinosterol and brassicasterol to nutrient-limited growth rate (Equation 4.8) was taken from Sachs and Kawka (2015; with growth rate units expressed in d^{-1}), assuming that the results for brassicasterol from *E. huxleyi* are representative of other sterols and other taxa. These values will be referred to as PN – α_{Dino} and PN – α_{Brass}. The growth rate inputs for Equation 4.8 are μ_{Dino} and μ_{Brass} for Gyre, and μ_{C16} for Aloha.

$$PN - \alpha_{sterol} = -0.044 * \mu_{sterol\ or\ C16}/ln(2) + 0.73 \quad \text{(Equation 4.8)}$$

4.3 RESULTS

4.3.1 *Hydrography*

A complete list of oceanographic parameters averaged from multiple CTD casts spanning each suspended particle collection period is provided in Table 1 and Supplementary Tables 4 and 5. During February 2012 sampling at Aloha, SST averaged 23-23.5°C and the surface mixed layer (SML) depth occurred between 70-95 m using the fixed temperature criterion of Δ0.5°C (158). At Gyre during July 2012 sampling, SST averaged 14-15°C, the SML depth occurred at 30-35 m, and a DCML occurred at 55 m.

4.3.2 *Lipid Concentrations*

$C_{16:0}$ and $C_{14:0}$ fatty acid concentrations were correlated (R^2=0.97, $p<0.001$), as were brassicasterol and dinosterol concentrations (R^2=0.96, $p<0.001$). Brassicasterol and dinosterol concentrations were each correlated with $C_{37:2}$ alkenone concentrations (brassicasterol: R^2=0.85,

$p<0.001$ and dinosterol: $R^2=0.75$, $p<0.001$). Fatty acid concentrations were not correlated with those of other lipids.

At Gyre, alkenones reached concentration maxima (between 5.43-8.05 µg/L for $C_{37:2}$ and 13.37-24.64 µg/L for $C_{37:3}$) in the DCML (at 45 and 55 m), and minima (0.67-0.85 µg/L for $C_{37:2}$ and 1.72-5.30 µg/L for $C_{37:3}$) in the surface chlorophyll maximum layer (at 25 m). During LVF 1, both brassicasterol and dinosterol concentrations reached maxima at 35 m (19.6 µg/L and 9.36 µg/L, respectively) in the surface chlorophyll maximum layer and minima at 25 m (2.92 µg/L and0.95 µg/L, respectively). During LVF 2, the maxima for both lipids occurred at 25 m (brassicasterol: 20.8 µg/L and dinosterol: 10.2 µg/L) and the minima occurred at 35 and 65 m (brassicasterol: 4.74-4.95 µg/L and dinosterol: 2.11-2.42 µg/L). There was a second concentration maximum at 55 m in the DCML during LVF 2 for both lipids. The fatty acids had by far the highest concentrations in the water column, with $C_{14:0}$ having the highest overall concentrations. $C_{16:0}$ and $C_{14:0}$ fatty acids had maxima at and above the surface chlorophyll maximum at 15-25 m (20.8-28.7 µg/L and 55.5-85.7 µg/L, respectively) and a second, greater maximima at 65 m below the DCML (42.1-55.5 µg/L and 117-119 µg/L, respectively). The lowest concentrations were at 35 m for both lipids, where lipid concentrations were not detectable in most LVFs. $C_{37:3}$ and $C_{37:2}$ concentrations were well correlated at all depths ($R^2=0.92$, $p<0.001$), as were $C_{16:0}$ and $C_{14:0}$ fatty acids ($R^2=0.94$, $p<0.001$) and brassicasterol and dinosterol sterol concentrations ($R^2=0.98$, $p<0.001$). No other lipid pairs were correlated at the Gyre site.

At Aloha, concentrations of $C_{37:2}$ alkenone, brassicasterol, and dinosterol were highest in the top 10-25 m (2.03-3.23 µg/L, 7.23-9.03 µg/L, 3.42-4.09 µg/L, respectively), and decreased approximately linearly with depth below 25 m (Supplementary Table 4.6 and Figure 4.1). Previous studies (135, 137) indicated a C_{37} alkenone maximum at or just below the SML, which is consistent

with our finding. Concentration minima for these three lipids occurred at 120 m (0.17-0.31 µg/L, 1.27-2.82 µg/L, 0.46-1.35 µg/L, respectively). Fatty acids displayed a different pattern, with high concentrations at shallowest depths ($C_{16:0}$: 4.96-16.5 µg/L and $C_{14:0}$: 1.85-12.6 µg/L) and secondary maxima at 120 m (LVF 1, $C_{16:0}$: 4.15 µg/L and $C_{14:0}$: 2.01 µg/L) and 70 m (LVF 2, C16:0: 7.39 µg/L and $C_{14:0}$: 4.90 µg/L). LVF 1 had minimum concentrations at 25 and 50 m ($C_{16:0}$: 0.47-0.67 µg/L and $C_{14:0}$: 0.16-0.32 µg/L), while LVF 2 had minima at 50 and 120 m ($C_{16:0}$: 0.40-0.90 µg/L and $C_{14:0}$: 0.17-0.23 µg/L). $C_{16:0}$ fatty acid had the highest concentrations overall.

4.3.3 *Lipid δ^2H values*

Alkenone δ^2H values

At Gyre, there was a clear distinction between α_{Alk} values in the mixed layer to a depth of ~30 m, and values below it. In the mixed layer, there was little change in α_{Alk}, while below it, α_{Alk} decreased linearly from 0.789 to 0.766 between 35 m and 65 m in LVF 1 (R^2=0.95, P=0.0254, n=4) and from 0.776 to 0.755 in LVF 2 (R^2=0.71, P=0.157, n=4) (Supplementary Table 4.9 and Figure 4.2g). This resulted from decreases in δ^2H of -215 to -238‰ and -227 to -248‰, respectively (Supplementary Table 4.7, Figure 4.2a). At Aloha, α_{Alk} and δ^2H_{Alk} averaged 0.815±0.005 (Supplementary Table 4.10, Figure 4.2h) and -184±4.5‰ (Supplementary Table 4.8, Figure 4.2b) throughout the water column, respectively, with no discernible trend.

Dinosterol δ^2H values

At Gyre, there is again an evident distinction between those samples collected in the mixed layer and those collected below it. From 45 m to 65 m, α_{Dino} values increased linearly with depth from 0.711to 0.720 in LVF 1 (R^2>0.99, P=0.047, n=3) and 0.707 to 0.718 in LVF 2 (R^2=0.92, P=0.18, n=3) (Supplementary Table 4.9, Figure 4.2g), while δ^2H values increased from -293 to -

284‰ and from -296 to -284‰, respectively (Supplementary Table 4.7, Figure 4.2c). However, for these data below the mixed layer, the error bars are large enough that it is not clear if the values are distinct.

At Station Aloha, α_{Dino} went from 0.708 at 10 m to 0.708 at 95 m for LVF 1 and from 0.701 at 10 m to 0.709 at 120 m in LVF 2 (Supplementary Table 4.10, Figure 4.2h). The δ^2H values ranged from -292 to -289‰ and -297 to -289‰, respectively (Supplementary Table 4.8, Figure 4.2d). For LVF 1, from 25-95 m there was an increase in α_{Dino} from 0.697 to 0.708, (R^2=0.99, P=0.004 , n=4). In LVF 2, there is a general increase in α_{Dino} with depth, but the error bars are overlapping, obscuring any trends.

Brassicasterol δ^2H values

At Gyre, α_{Brass} again has a distinction between the samples collected within and below the mixed layer (Figure 4.2g). Below the mixed layer, from 45-65 m, α_{Brass} was invariant at 0.733 for LVF 1 and between 0.734 and 0.724 for LVF 2, with the associated δ^2H_{Brass} values between -270 and -271‰, and between -270 and-279‰, respectively (Supplementary Tables 4.7 and 4.9, Figure 4.2c). There was no change in α_{Brass} below the mixed layer for LVF 1, but for LVF 2 there was a decrease with depth (R^2=0.88, P=0.036, n=3), however the error bars overlap for these three points.

At Aloha, α_{Brass} decreased non-uniformly from 0.722 at 10 m to 0.714 at 120 m in LVF 1, and from 0.711 at 10 m to 0.709 at 120 m in LVF 2 (Supplementary Table 4.10, Figure 4.2h). The associated δ^2H values declined from -278 to -287‰ and -282 to -290‰, respectively (Supplementary Table 4.8, Figure 4.2d). The slight decrease in α_{Brass} observed with depth in each LVF was not statistically significant.

Influence of time-of-day on δ^2H_{lipid}

While significant variance in specific lipid δ^2H value was measured over the course of a single day at a defined depth (>10‰, Supplementary Tables 4.11 and 4.12), no systematic dependence of $\delta^2H/^1H$ fractionation on the time collected during the daylight hours was observed in any lipid (Figure 4.2a-d). Previous studies have provided evidence that different taxa of algae collectively divide at night and undergo synchronized diel cycles of metabolic and biochemical activity (159–163). It was considered that if growth rate and internal biochemical factors had a large influence on α_{lipid}, that a systematic pattern of fractionation throughout the day corresponding to growth stage or metabolic activity might emerge. However, no evidence of such a pattern emerged, indicating that either biochemical changes occurring due to synchronized diel activity happen on faster timescales than those measured in this study or that external controls on biochemical activity had a greater influence on α_{lipid} than internally regulated activity. In the subsequent analysis, all samples collected on a single day were combined.

4.3.4 *Growth Rates*

Growth rate values for all lipids

At Gyre, $C_{37:2}$ alkenone, $C_{16:0}$ fatty acid, $C_{14:0}$ fatty acid, and brassicasterol all exhibited higher $\delta^{13}C$ values in ^{13}C-incubated samples than in non-incubated samples. The $\delta^{13}C$ difference between the two was greatest at shallower depths, and decreased to near zero at the deepest depths (Supplementary Tables 4.13 and 4.14, Figure 4.3). The implied decrease in growth rates with depth at Gyre is in agreement with the results of Popp et al. (2006a), who reported a decrease in ^{13}C-derived growth rate with depth in alkenone-producing microalgae at that location.

^{13}C-derived growth rates (Supplementary Table 4.15) from $C_{37:2}$ (μ_{Alk}) at Gyre declined from 0.099-0.318 d^{-1} at 15 m to 0.007-0.087 d^{-1} at 65 m (Figure 4.4e), while those from $C_{16:0}$ (μ_{C16})

declined from 0.062 – 0.113 d^{-1} at 15 m to 0.000 – 0.010 d^{-1} at 55-65 m (Figure 4.4c), and those from $C_{14:0}$ (μ_{C14}) declined from 0.139 – 0.198 d^{-1} at 15 m to -0.006 - 0.065 d^{-1} at 55 - 65 m (Figure 4.4a). Negative estimated growth rates are an artifact of the comparison of labeled incubation to unlabeled water column lipid compounds, and mean essentially zero growth. $C_{14:0}$ estimated growth rates were generally higher than those estimated from $C_{16:0}$, which would be consistent with faster labeling kinetics and turnover times of $C_{14:0}$, and with $C_{14:0}$ being a precursor to $C_{16:0}$ during synthesis. ^{13}C-derived growth rates from brassicasterol (μ_{Brass}) declined from 0.080 – 0.109 d^{-1} at 15 m to 0.006 – 0.018 d^{-1} at 55 m (Figure 4.4g).

$\delta^{13}C$ of dinosterol at Gyre did not follow the same pattern. ^{13}C-incubated samples had $\delta^{13}C$ values that were only marginally higher than unincubated samples at all depths (Figure 4.3h and 4.5h). ^{13}C-derived growth rates from dinosterol (μ_{Dino}) ranged from 0.004 - 0.024 d^{-1} at 15 m to 0.007 – 0.021 d^{-1} at 55 m (Supplementary Table 15), implying little or no dinosterol production during the course of the two 24-hr periods. The implied differences in growth rate between dinosterol-producers and producers of other lipids at Gyre is significant, but perhaps not unexpected. Some evidence from culture studies exists showing that dinoflagellates grow more slowly than other eukaryotic phytoplankton of similar size (164). Since comprehensive information on which dinoflagellate species might be producing dinosterol at this particular location is unavailable, it can only be speculated that this is the reason for the difference observed in the uptake of $DI^{13}C$.

At Aloha, $\delta^{13}C$ values of ^{13}C-incubated samples were always higher than in non-incubated samples, indicating production of all measured lipids during the 24-hr incubations (Supplementary Table 4.16, Figure 4.3). For $C_{37:2}$ alkenones, there was little variation in ^{13}C uptake with depth (Figure 4.3f), and correspondingly no trend in the growth rate of alkenone-producers, with μ_{Alk}

ranging from 0.014 to 0.064 d^{-1} (Supplementary Table 4.17, Figure 4.4f). On the contrary, ^{13}C uptake into $C_{14:0}$ and $C_{16:0}$ fatty acids decreased with depth, resulting in values of μ_{C14} that declined from 0.232 – 0.301 at 10 m to 0.130 – 0.179 d^{-1} at 95 - 120 m (Figure 4.3b and 4.5b), and values of μ_{C16} that declined from 0.109 – 0.132 at 10 m to 0.015 – 0.044 d^{-1} at 95 - 120 m (Figure 4.3d and 4.5d).

Whereas ^{13}C-derived growth rates from alkenones were lower at Aloha than at Gyre (Figure 4.4e vs Figure 4.4f), those from $C_{14:0}$ and $C_{16:0}$ fatty acids were higher at Aloha (Figure 4.4a and c vs. Figure 4.4b and d).

Correlation between growth rates and irradiance levels

At Gyre, the ^{13}C-derived growth rates from brassicasterol, $C_{14:0}$ fatty acid, and $C_{16:0}$ fatty acid were correlated with noon PAR values at depths greater than 35 m (representing PAR values below 300 μmol m^{-2} s^{-1}) during both LVFs. The R-squared values were above 0.9 in all three cases (n=3 for each): for brassicasterol, LVF 1: 0.998 and LVF 2: 0.97, for $C_{14:0}$ fatty acid, LVF 1: 0.96 and LVF 2: 0.96, and for $C_{16:0}$ fatty acid, LVF 1: 0.95 and LVF 2: 0.98. ^{13}C-derived growth rates from dinosterol were not correlated with PAR for either LVF. ^{13}C-derived growth rates from alkenones collected in LVF 2 were correlated with PAR at 45 m and below (R^2=0.91), but had a low correlation in LVF 1 (R^2=0.56).

At Aloha, the ^{13}C-derived growth rates from $C_{37:2}$, $C_{14:0}$ fatty acid, and $C_{16:0}$ fatty acid showed no relationship with noon PAR values for either LVF.

4.4 DISCUSSION

4.4.1 *Growth Effect of Irradiance and Nutrient-Limited Growth on $\delta^2H_{alkenone}$*

It was expected that at Gyre, alkenone-producing organisms would be primarily light-limited, rather than nutrient-limited, based on the study by Popp et al. (2006a), in which a linear relationship between growth rate and irradiance was observed below saturating light levels (136). The correlation between growth rate and noon PAR in LVFs 1 and 2 bear this out, although LVF 1 has a weaker correlation. Whereas at Aloha, alkenone-producers were hypothesized to be limited by nutrients owing to the nutrient-impoverished status of that oligotrophic subtropical gyre location (149), and by nutrients and light in the lower part of the euphotic zone. There was no correlation observed between growth rates and noon PAR at this site, providing evidence for this assertion. Because nutrient limitation (higher α_{Alk}) (119, 120) and light limitation (lower α_{Alk} below saturating light levels of 100-200 μmol m^{-2} s^{-1}) (121) have been shown to cause opposing changes in α_{alk}, we sought to discern which of those conditions characterized alkenone producers in the water columns at Aloha and Gyre from measurements of α_{alk}.

At Gyre, daily average α_{alk} values for the $C_{37:3}$ alkenone decreased below 35 m (Figure 4.2g). These values were compared to those predicted for irradiance-driven (PI-α_{Alk}) and nutrient-limited-growth-rate-driven (PN-α_{Alk}) in Figure 4.5a. Positively correlated and similar absolute values between PI-α_{Alk} and α_{Alk} values (LVF 1: R^2=0.99, P<0.001; LVF 2: R^2=0.94, P=0.028) support the interpretation of an irradiance-driven fractionation effect below the mixed layer. Predicted PI-α_{Alk} values are based on work by Van der Meer et al. (2015), who reported a ~40‰ decrease in δ^2H_{Alk} (i.e., α_{Alk} =0.04) with increasing light up to 200 μmol m^{-2} s^{-1}. At Gyre, δ^2H_{Alk} changes of ~20-22‰ below the mixed layer occurred (Figure 4.2a). For comparison, δ^2H_{Alk} changes of only 1-3‰ (i.e., PN-α_{Alk} =0.001-0.003) are predicted if nutrient-limitation of growth

rate were the primary driver of δ^2H_{Alk} changes below the mixed layer at Gyre (Figure 4.5a). Because irradiance at depths shallower than 35 m exceeded 200 μmol m^{-2} s^{-1}, and was therefore above the level at which α_{Alk} was sensitive to irradiance in Van der Meer et al. (2015), and likely exceeded saturating irradiance for *E. huxleyi* (136), covariance between PI-α_{Alk} and measured α_{Alk} is not expected from 15-25 m. Because growth rate and irradiance were correlated during at least one LVF, it is possible that depth-related α_{Alk} changes resulted from growth rate changes caused by light-limitation rather than just photon flux. This distinction is necessary because, unlike in the chemostat study by Sachs et al. (2017), which kept growth rate constant across different light treatments, Van der Meer et al. (2015) employed batch cultures that did not control growth rate in the different light treatments. Because the Sachs et al. (2017) study was performed with a (non-alkenone-producing) diatom, predicted α values for alkenones as a function of irradiance are derived from the Van der Meer et al. (2015) study, which was performed with *E. huxleyi*.

At Aloha, α_{Alk} values were nearly identical to those predicted for growth limitation by nutrients (PN-α_{Alk}), both nearly constant with depth (0.815 +/- 0.005 for α_{Alk} and 0.818 +/- 0.001 for PN-α_{Alk}) (Figure 4.5b). This is consistent with Aloha's oligotrophic setting and the low ^{13}C-derived growth rates throughout the water column, which were all <0.1 d^{-1} (Figure 4.4f). Such low growth rates would not be expected to cause measurable changes in α_{Alk}, which has a sensitivity to nutrient-limited growth rate of 25‰ d^{-1} (Eqn. 4; Sachs & Kawka, 2015). Although irradiance decreased with depth (Table 4.1), predicted fractionation factors from light limitation (PI-α_{Alk}) differed substantially from measured α_{Alk} values (Figure 4.5b). Thus, all evidence points to nutrient-limited growth rate as the primary influence on α_{Alk} values at Aloha.

4.4.2 *Effect of Irradiance and Nutrient-Limited Growth on δ^2H_{sterol}*

As with alkenones, higher growth rates lower α (increase $^2H/^1H$ fractionation) in sterols from continuous cultures of both *E. huxleyi* and *T. pseudonana* when nutrients were used to limit growth (119). Unlike for alkenones, though, α also decreases (greater $^2H/^1H$ fractionation) in sterols from *T. pseudonana* in response to increased irradiance (119). However, because the predicted changes in α_{sterol} resulting from the measured range of irradiances (PI-α_{sterol}) at both Gyre and Aloha far exceeds those expected for the measured range of nutrient-limited growth rates (PN-α_{sterol}), the two influences can potentially be discerned.

^{13}C-derived growth rate estimates from sterols at Gyre decreased with depth for brassicasterol (Figure 4.4g) and were very low (<0.02 d^{-1}) and statistically invariant for dinosterol (Figure 4.4h). At Aloha, ^{13}C-based growth rate estimates for sterols were not obtained, but would be expected to have decreased or been invariant with depth based on the ^{13}C-derived growth rates for alkenones (Figure 4.4f) and $C_{14:0}$ (Figure 4.4b) and $C_{16:0}$ (Figure 4.4d) fatty acids at that site.

4.4.2.1 Dinosterol

Gyre

At Gyre, α_{Dino} increased with depth below the mixed layer at 35 m significantly during LVF 1 (LVF 1: R^2>0.99, P=0.047, n=3, LVF 2: R^2=0.92, P=0.18, n=3), and both LVFs combined: R^2=0.78, P=0.013, n=6, a trend that could be explained by either light limitation or nutrient limitation of growth rate (Figure 4.5e). Considering the latter first, ^{13}C-derived growth rates for dinosterol were all very low (<0.02 d^{-1}) and trendless with depth (Figure 4.4h), unlike those for four other lipids (brassicasterol (Figure 4.4g), $C_{37:2}$ alkenone (Figure 4.4e), $C_{14:0}$ (Figure 4.4a), and $C_{16:0}$ (Figure 4.4b)). The small range of ^{13}C-μ_{Dino} values results in a maximum predicted

range for α_{Dino} in response to nutrient limitation of growth (PN-α_{Dino}) of <1‰ (Figure 4.5e), substantially smaller than the observed 9-11‰ increase in δ^2H_{Dino} below the mixed layer (Figure 4.2b, g). This assumes that the H isotope fractionation response for dinosterol is similar to that for sterols produced by *E. huxleyi* and *T. pseudonana*, the only two taxa for which published α_{sterol} data exist (119). Given a factor of two range in the sensitivity (i.e., (-29 to -63 ‰ d^{-1}) of α_{sterol} to nutrient-limited growth rate changes in the two taxa (and sterols) from that study, absolute values of PN-α_{Dino} cannot be known with confidence. But depth-related trends in α_{sterol} are still informative if the sign of the fractionation response is the same as observed in the two taxa for which experimental data exist. Thus, a lack of trend in both PN-α_{Dino} and α_{Dino} in the upper 45 m is consistent with nutrient limited growth of dinosterol producers. However, below the mixed layer, where α_{Dino} increases some 10‰ while PN-α_{Dino} remains nearly constant, light limitation is a viable explanation. The ^{13}C derived growth rates for dinosterol had no relationship to noon PAR values, indicating that growth rate was not primarily light limited. Therefore, any effect of irradiance on α_{Dino} is through photon flux.

It is also worth noting that the error bars for the data points in this set are large enough to overlap and possibly obscure any trend in the water column. If there is truly no trend in α_{Dino} in the water column, that would point to a nutrient-limited growth rate control of fractionation for the reasons stated above. One reason the error bars are so large, however, is because they incorporate both analytical error and temporal variability, which wouldn't usually be measured in samples that are representative of longer time periods. Nevertheless, the large error bars do not preclude a light-limited trend in the water column at Gyre. In other data from this study where error bars overlap, such as Aloha brassicasterol, there is not otherwise a measured trend in the water column. In addition, for brassicasterol and alkenones, the α values can be compared more

directly to predicted values based on culture experiments since those same lipids were investigated. This necessarily makes interpretation of the α_{Dino} values the least well constrained.

Both the predicted (PI-α_{Dino}) and measured values of α_{Dino} increased with depth below the mixed layer, supporting the possibility that light limitation of dinosterol producers influenced their H isotopic composition (Figure 4.5e). However, the increase in the predicted value of PI-α_{Dino} (45-77‰) was about 5-fold larger than that for α_{Dino} (9-11‰), implying one of several possibilities. One is that the α_{Dino} response to light may be smaller for dinosterol than for *T. pseudonana*-produced 24-methyl-cholesta-5,24(28)-dien-3-ol) – the sterol for which the calibrated response to light is derived (-0.8‰ (μmol m^{-2} s^{-1})$^{-1}$; Eqn. 3 (Sachs et al., 2017)). Another is that both light and nutrient-limitation may have impacted α_{Dino}. A third is that our rudimentary knowledge of the factors controlling H isotope fractionation in phytoplankton is inadequate to fully explain the observations. Finally, heterotrophic dinoflagellates can be a significant source of dinosterol (165), and dinosterol produced by these organisms would be expected to be ^{2}H-enriched compared to that from photoautotrophic dinoflagellates (166). Any change in the community composition of dinosterol producers within the water column has the potential to impact the α_{Dino} trends observed in the water column.

Aloha

At Aloha, α_{Dino} values increased with depth in LVF 1, the trend predicted for both nutrient (PN-α_{Dino}) and light (PI-α_{Dino}) limitation of growth, although the trend is obscured in LVF 2 given the large error bars (Figure 4.5f). The lower absolute values of measured versus predicted α_{Dino} may be due to the fact that no culture-based H-isotopic calibration studies have been published yet with a dinoflagellate, so the diatom and coccolithophorid-based calibrations may not be representative. A further uncertainty is the lack of measured ^{13}C-derived growth rates

from dinosterol at Aloha. Nevertheless, the trend in α_{Dino}, particularly the increase at depth, is consistent with both nutrient and light limitation. Despite these limitations, a nutrient-limited growth rate response of α_{Dino} seems plausible at this location given the similar muted trends in both α_{Dino} and PN-α_{Dino}, compared to that predicted for PI-α_{Dino} (which exceeds 100‰ at irradiances <200 μmol m^{-2} s^{-1}) and the observation that Aloha is a permanently oligotrophic location (Figure 4.5f). A change from nutrient-limited growth rate control at the shallowest depths to light limited control at greater depths is a possibility, given the uniform increase in α_{Dino} (^{2}H-enrichment) that reached 8‰ at irradiances <200 μmol.

4.4.2.2 Brassicasterol

Gyre

Throughout the water column at Gyre α_{Brass} values were close to those predicted for nutrient-limited growth, and except at 45 and 55 m, were distinct from those expected in response to light limitation (Figure 4.5c). As the model for PN-α_{Brass} is based on brassicasterol from a continuous culture of *E. huxleyi,* the values of α_{Brass} and PN-α_{Brass} are directly comparable (119). Although brassicasterol is produced by *E. huxleyi* and other coccolithophores, the trend with depth in α_{Brass} differs from that of α_{alk} (i.e., compare Figure 4.5c to Figure 4.5a), which may be attributable to the fact that brassicasterol has multiple phytoplankton sources while alkenones are likely overwhelmingly produced by just two prymnesiophyte species in the open ocean (*E. huxleyi* and *G. oceanica* (167–169)). However, while not following the same trend, α_{Alk} and α_{Brass} are correlated at all depths across both datasets (R^2=0.70; p=0.0009, n=12), while α_{Brass} and α_{Dino} are not correlated at any depths. While not conclusive, this analysis supports the possibility that *E. huxleyi* was a predominant producer of brassicasterol at Gyre. If that were the case, it remains unexplained why depth variations in α_{Brass} do not follow PI-α_{Brass}, while α_{Alk} and PI-α_{Alk} do track

one another (at irradiance levels below 200 μmol m^{-2} s^{-1}) (Figure 4.5a, c). One possibility is that coccolithophores do not display the same $^{2}H/^{1}H$ fractionation response to light as diatoms such as *T. pseudonana*. A further consideration is that the ^{13}C-derived growth rates for brassicasterol were correlated with PAR values during both collections. However, PI-α_{Brass} is based on a chemostat culture study where irradiance was limiting and growth rate was held constant (Sachs et al., 2017). It is possible that light limited growth rate causes a different magnitude change in α_{lipid} than irradiance alone, and that effect has not yet been measured in sterols.

It also cannot be ignored that, as the least source-specific lipid in this study, brassicasterol is known to be produced by such diverse taxa as coccolithophores, diatoms, dinoflagellates, and cyanobacteria, among others (127, 129, 170). While some brassicasterol producers may have been nutrient-limited, others may have been light-limited, and the measured values of α_{Brass} likely reflect this diversity of responses. Furthermore, the phytoplankton assemblage at Gyre may change with depth (146), potentially altering the relative proportions of PI-α_{Brass} and PN-α_{Brass} that contribute to measured α_{Brass} values. Taylor and Waters (1982) reported high abundances of the dinoflagellate *Gymnodinium simplex* at depths below 50 m and high abundances of the coccolithophore *E. huxleyi* above that depth. Brassicasterol comprised 53% of the sterols produced by cultured *Gymnodinium simplex* and 98% of the sterols produced by *E. huxleyi* (130). It should be noted however that the Taylor and Waters (1982) study consisted of two transects across the basin, with each station being occupied twice, and only on one transect was the vertical zonation of the phytoplankton community observed. Nevertheless, if vertical zonation of brassicasterol-producing phytoplankton is common in the Gyre region it could account for α_{Brass} changes there. Because the same lipid produced by different phytoplankton taxa can have $\delta^{2}H$ values that differ by up to 100‰ (103), the ~10‰ change in $\delta^{2}H_{Brass}$ measured

in this study could have resulted from a gradual shift in the phytoplankton community from one brassicasterol producer to another.

Aloha

As at Gyre, α_{Brass} values tracked those expected for nutrient limitation better than those expected for light limitation, spanning a range of 13‰ (Figure 4.5d). This compared to a predicted range of 6‰ for nutrient limitation (PN-α_{Brass}), and 150‰ for light limitation (PI-α_{Brass}). Furthermore, from 10-70 m the values of PN-α_{Brass} and α_{Brass} were statistically the same (Figure 4.5d). Again, this is noteworthy because the model for PN-α_{Brass} is based on brassicasterol from a continuous culture of *E. huxleyi* (119). Although it is unclear which species are producing brassicasterol in the water column, *E. huxleyi*, common at Aloha (135, 137, 153), was likely one of those species.

At the two deepest depths (100 and 120 m) α_{Brass} values were lower than those predicted for nutrient-limited growth, and much lower than predicted for light-limitation of growth (Figure 4.5d). This could be related to the shift in phytoplankton community structure that is known to occur at ~100 m at Aloha, from coccolithophore dominance above that depth to diatom predominance below (150–152).

4.4.3 *Salinity and Temperature Effects*

The effect of salinity on δ^2H fractionation has been well documented in both laboratory and field experiments that indicate an increase in lipid δ^2H of 1-2‰ per unit increase in salinity (111, 114). At both Aloha and Gyre there was a salinity change of less than 1 with depth (Table 1), implying that any measurable changes in lipid δ^2H values were unlikely to have been caused by salinity variations. The effect of temperature on δ^2H is less well studied, but may be in the range

of -2 to -8‰ $°C^{-1}$ (113, 117, 118, 171). One would therefore expect to see an increase in lipid α and δ^2H values as temperatures decrease with increasing water depth. At Aloha there was less than 1° C variation in temperature through the water column (Table 1). At Gyre, there was a change of ~4° C throughout the euphotic zone. At neither location was there a systematic increase in α and δ^2H with depth throughout the water column, certainly not as large as the 8-32‰ that would be expected if temperature were the primary influence on lipid δ^2H values at Gyre. As with salinity, it is concluded that temperature cannot be the primary cause of H isotopic changes with depth at either location.

4.4.4 *Measuring Producer-Specific Growth Rates*

^{13}C-derived growth rates from different lipids did not always display the same patterns between the two study sites, such as relative rate differences derived from alkenones (higher at Gyre) and those derived from fatty acids (higher at Aloha). Since $C_{14:0}$ and $C_{16:0}$ fatty acids are produced by all phytoplankton, the growth rate estimates from these lipids are non-specific community growth rates. The relative difference between growth rates of specific populations, such as alkenone-producers, and the general phytoplankton community at each location speaks to the usefulness of measuring biomarker-producer specific growth rates. One caveat, however, is that the different environmental and biochemical factors that cause organisms to produce certain lipids at specific times, i.e. fatty acids as opposed to alkenones, are also likely to have played a role in the different growth rates measured at each site.

4.4.5 *Implications for δ^2H Paleoproxy*

Due to the large changes in δ^2H_{lipid} that are possible in response to irradiance and nutrient limited growth rate variations it is important to consider how these parameters may influence

paleoenvironmental reconstructions based on δ^2H_{lipid}. While this study found that δ^2H_{lipid} values in the euphotic zone at two North Pacific locations can span up to a ~35‰ range, and that this range can be attributed to one or both irradiance and nutrient-limited growth rate variations, in most instances the depth variation in δ^2H was not much larger than one or both the inter-day range at a single depth, or the analytical uncertainty associated with measuring δ^2H_{lipid}. Thus it may be that the large effects that irradiance and nutrient-limitation of growth can have in laboratory culture studies may not be realized in the field, and particularly not in sediment-based δ^2H reconstructions. Additional field-based measurements of δ^2H_{lipid} alongside growth rate and irradiance measurements should be conducted in order to confirm this. Studies measuring δ^2H_{lipid} of rapidly growing phytoplankton during a bloom might be useful, as lipids from these organisms are likely to end up in sediments.

The large variability in δ^2H_{lipid} over a single day, in a seemingly random pattern, could be a cause for concern for studies such as this one attempting to validate culture studies in the field. The collection time could play a large role in the results obtained, and even studies in the same location might obtain different results if they sampled at different times of the day. Continuous sampling over an entire day is one way to circumvent any such bias.

Given that there were measurable differences in δ^2H_{lipid} from the top of the euphotic zone to the bottom, another important consideration for paleoceanographic applications of δ^2H_{lipid} pertains to the water depth at which lipids that become buried in sediments were synthesized. Sedimentary δ^2H_{lipid} values might be interpreted differently if it were known, for example, that a narrow depth range was the primary contributor of a particular lipid, as opposed to each water depth contributing equally to the sedimenting flux. TO investigate this further, future studies might systematically compare δ^2H_{lipid} in the water column to surface-sediment values.

4.5 CONCLUSIONS

Hydrogen isotope values of four microalgal lipids were measured through the euphotic zone at two North Pacific locations to assess the potential effects of light and nutrient-limited growth on $^{2}H/^{1}H$ signatures in phytoplankton lipid biomarkers. For alkenones, a distinction between nutrient-limited growth rate effects at Station Aloha, and irradiance effects at Gyre emerged based on the hydrogen isotope response to light and nutrient limited growth in cultured phytoplankton. In the case of dinosterol, α values could be attributed to nutrient limitation or light limitation in the lower euphotic zone, but the amplitude of change was smaller than predicted from culture experiments. For brassicasterol, α values at both locations were consistent with nutrient limitation of growth, varying within narrow ranges compared to those predicted for irradiance effects.

Although the measured variations in $\delta^{2}H_{lipid}$ were attributed to one or both irradiance and nutrient-limited growth rate, the magnitude of these changes was smaller than expected based on culture studies. The inter-day range at a single depth was of the same order of magnitude as the inter-water-column range in most instances for all three lipids, leading to the conclusion that the large effects of irradiance and nutrient-limited growth rate from culture studies may not be realized in the field, and thus may not influence paleoceanographic reconstructions from sediments. The $\delta^{2}H_{lipid}$ variability that occurred throughout the day in the water column warrants further study, as does the water depth from which sedimentary lipids derive, as that is ultimately what is being measured in paleoceanographic reconstructions.

4.6 ACKNOWLEDGEMENTS

This material is based upon work supported by the National Science Foundation under Grant No. OCE-1027079 (JPS) and GRFP DGE-1265082 (MPW). We would like to thank Brian Popp for instructing us on his technique for ^{13}C incubations and generously lending us his *in situ* phytoplankton incubation equipment. We also thank the captain and crew of the *R/V Thomas G. Thompson* and the *R/V Point Sur* for facilitating the two successful research cruises during which the samples reported on here were collected. We are grateful to A. Maloney, J. Richey, S. N. Ladd, D. Nelson, I. Bystrom, N. Wallsgrove, C. Hannides, M. Widlansky, E. Norton, M. Siple, E. Porter, C. Lyons, C. Wardell, R. D'Jay, L. Sandwick, J. Huynh, K. Simans, and T. Johnson for their shipboard assistance collecting samples, and to A. Gothmann for assistance with pH measurements, and I. Bolden for help with alkalinity measurements. Conversations with M. Wolhowe improved this manuscript. We thank three anonymous reviewers and Associate Editor Ann Pearson for their comments that substantially improved this manuscript.

4.7 TABLES

Table 4.1 Characteristics of Each Site

Day/LVF	Depth	Salinity	Temperature (°C)	Noon PAR (µmol photons m^{-2} s^{-1})
Aloha				
1	10	35.21	23.47	656.38
1	25	35.21	23.47	533.45
1	50	35.22	23.44	177.51
1	70	35.30	23.28	67.86
1	95	35.40	23.04	18.94
1	120	35.39	22.83	9.07
2	10	35.22	23.52	417.43
2	25	35.22	23.51	184.56
2	50	35.24	23.46	80.54
2	70	35.34	23.20	35.60
2	95	35.41	23.00	15.08
2	120	35.38	22.68	4.77
Gyre				
1	15	32.88	14.50	613.89
1	25	32.88	14.50	383.14
1	35	32.86	14.50	242.76
1	45	32.84	12.50	126.76
1	55	32.84	11.70	61.20
1	65	32.84	11.00	30.68
2	15	32.87	14.50	485.31
2	25	32.86	14.50	286.44
2	35	32.87	12.50	159.83
2	45	32.87	12.00	69.08
2	55	32.86	11.00	26.39
2	65	32.85	10.70	12.67

4.8 FIGURES

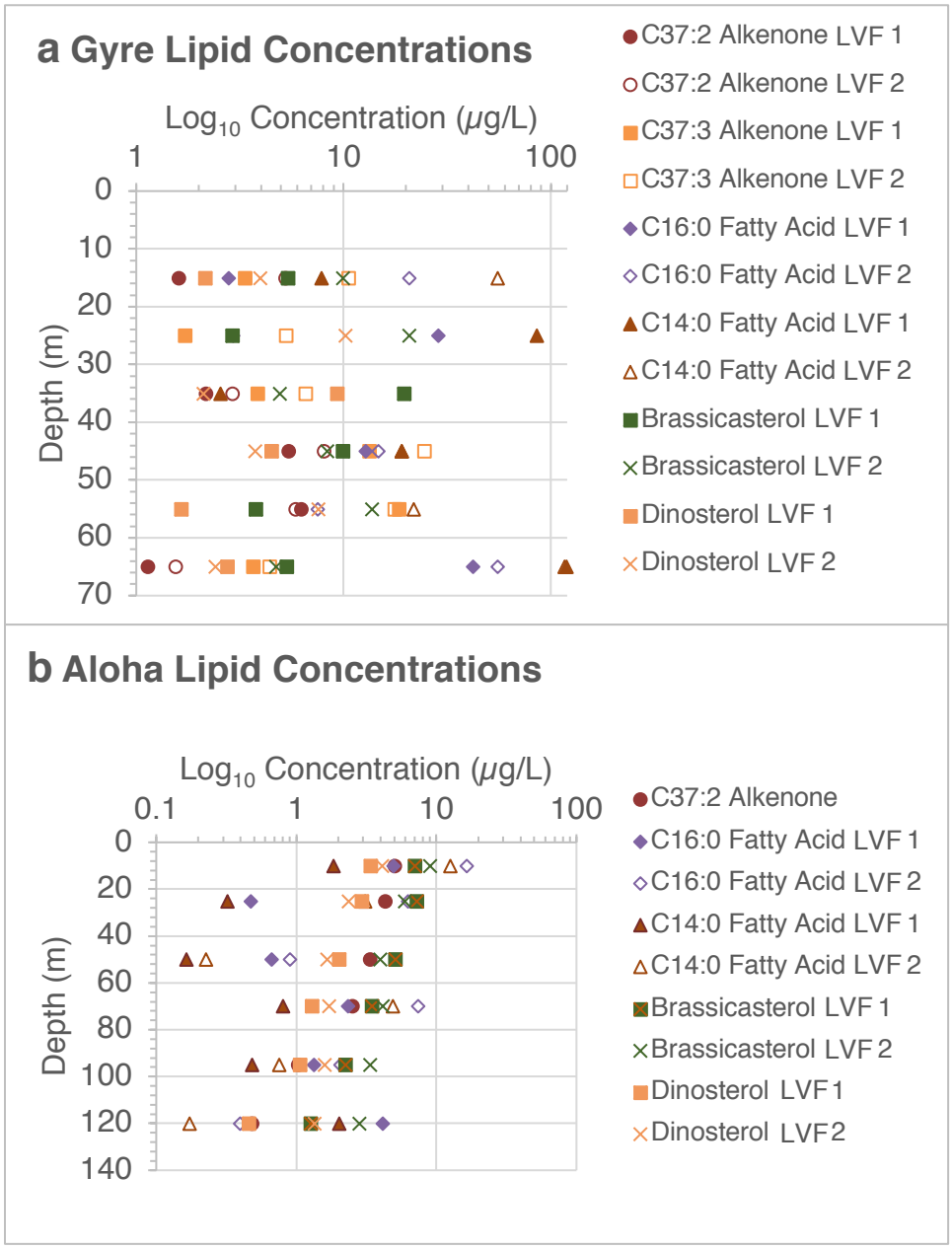

Figure 4.1. (a) Gyre and (b) Aloha lipid concentrations for $C_{37:2}$ and $C_{37:3}$ alkenones, $C_{16:0}$ and $C_{14:0}$ fatty acids, brassicasterol, and dinosterol. Closed circles represent LVF 1 collections and open circles represent LVF 2 collections.

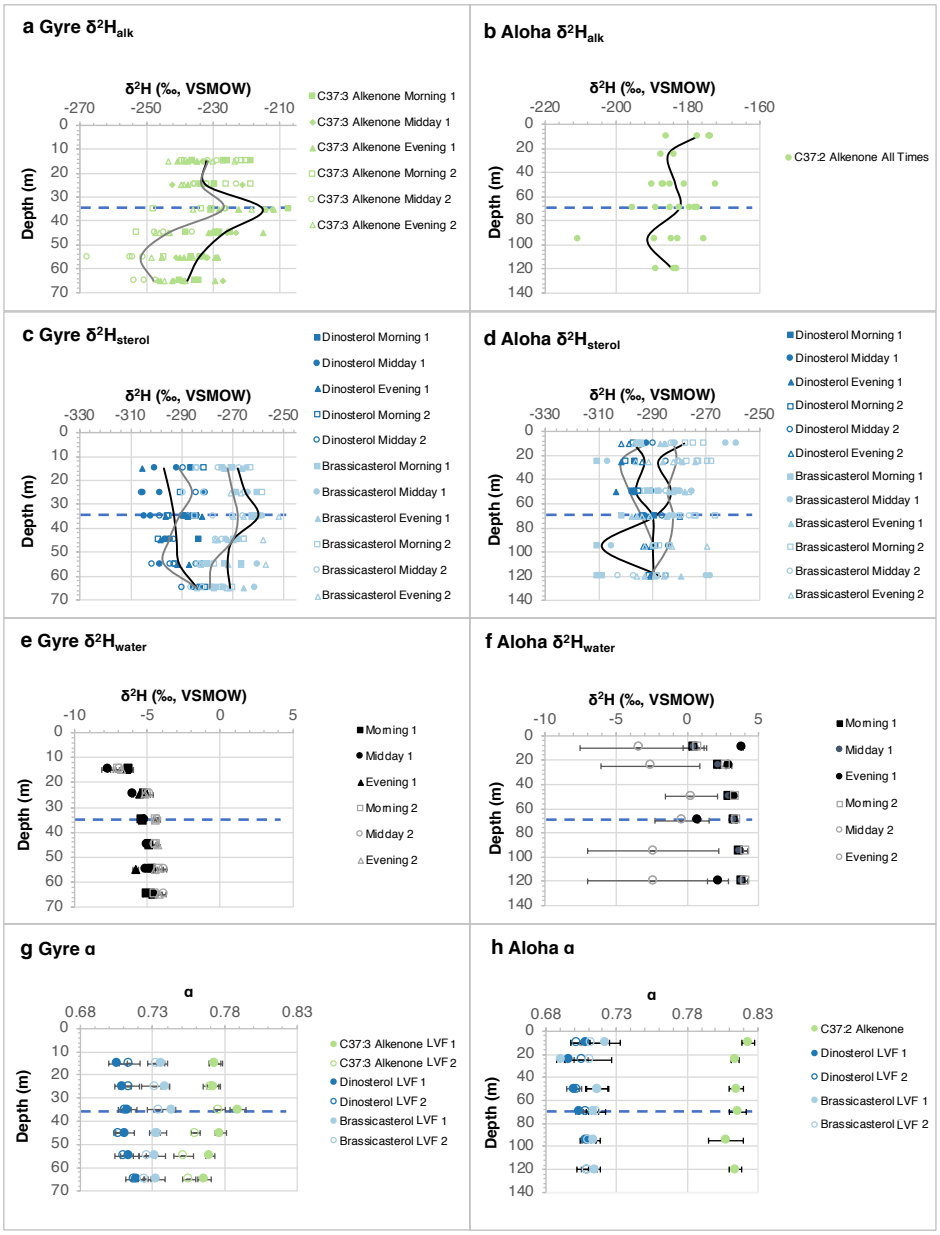

Figure 4.2. (a) Gyre δ^2H and (b) Aloha δ^2H values of $C_{37:3}$ and $C_{37:2}$ alkenones, and (c) Gyre δ^2H and (d) Aloha δ^2H values of brassicasterol (light blue), and dinosterol (dark blue). Measurements are from morning (squares), midday (circles), and evening (triangles), or averaged values from two LVF data sets (LVF 1 filled in markers and LVF 2 outlined markers). Black lines (LVF 1) and gray lines (LVF 2) are averaged values of each LVF dataset. Uncertainties for measurements in (a)-(d) can be found in Supplementary Tables 4.6 and 4.7, since placing error bars on each data point would have made the plot too difficult to read. (e) Gyre and (f) Aloha surface water δ^2H values were measured corresponding to each lipid collection. (g) Gyre α and (h) Aloha α values of $C_{37:3}$ and $C_{37:2}$ alkenones (green), brassicasterol (light blue), and dinosterol (dark blue) from two LVF data sets (LVF 1 filled in markers and LVF 2 outlined markers). The dotted line marks the mixed layer at each site (35 m at Gyre and 70 m at Aloha).

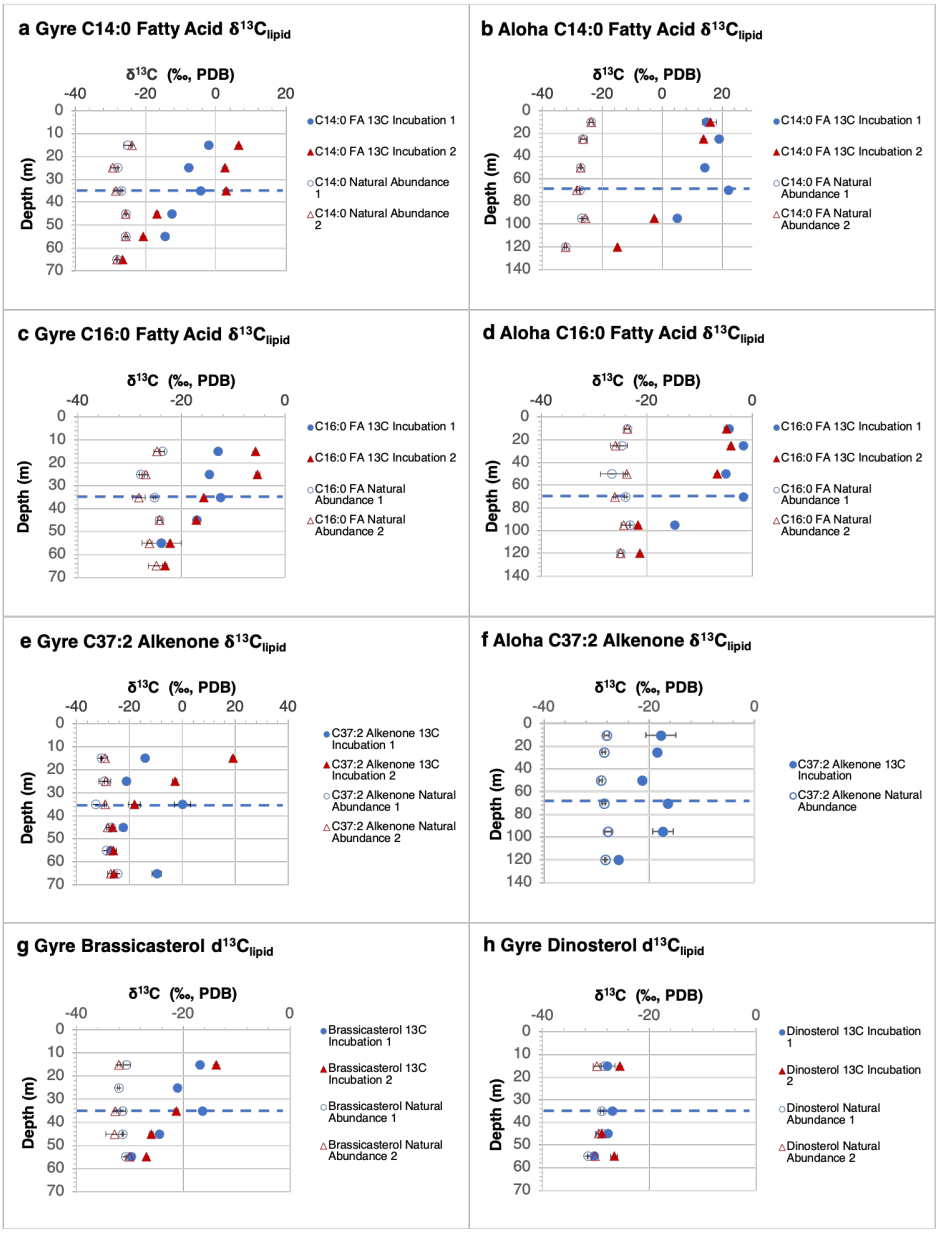

Figure 4.3. Incubation (filled in markers) and natural abundance from LVF (outlined markers) $\delta^{13}C$ values of Gyre lipids C14:0 fatty acid (a), C16:0 fatty acid (c), $C_{37:2}$ alkenone (e), brassicasterol (g), and dinosterol (h), and Aloha C14:0 fatty acids (b), C16:0 fatty acids (d), and $C_{37:2}$ alkenones (f). ^{13}C incubation $\delta^{13}C$ values are clearly enriched compared to the natural abundance samples, indicating growth of the producing organisms. The exception is the Gyre Dinosterol $\delta^{13}C$ values, which show no difference between incubation and natural abundance samples. The dotted line marks the mixed layer at each site (35 m at Gyre and 70 m at Aloha).

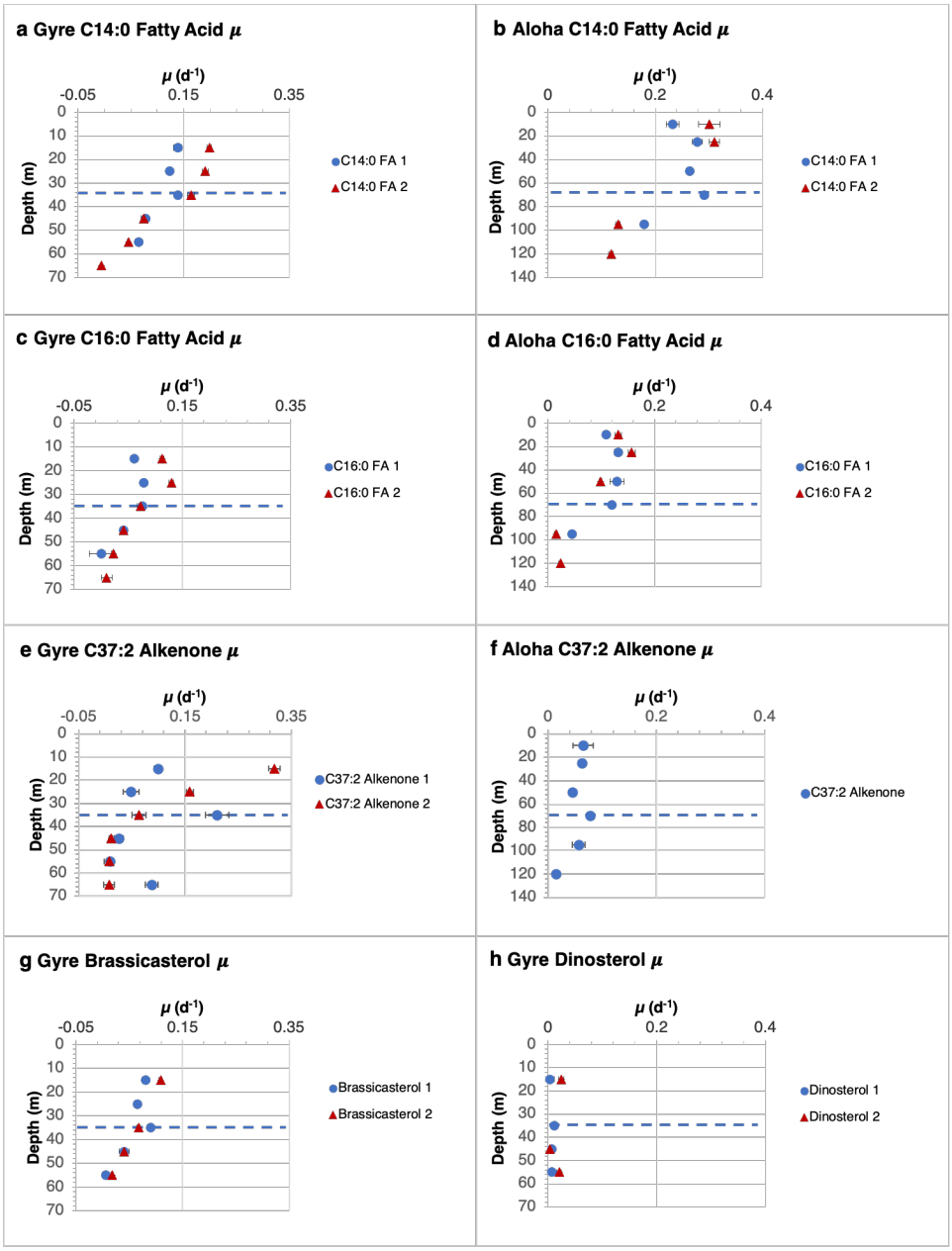

Figure 4.4. Estimated growth rates of Gyre C14:0 fatty acid (a), C16:0 fatty acid (c), $C_{37:2}$ alkenones (e), brassicasterol (g), and dinosterol (Hh, and Aloha C14:0 fatty acid (b), C16:0 fatty acid (d), and $C_{37:2}$ alkenones (f) from Incubation 1 (circles) and Incubation 2 (triangles). In each case, the growth rates decrease with depth with the exception of dinosterol producers. The dotted line marks the mixed layer at each site (35 m at Gyre and 70 m at Aloha).

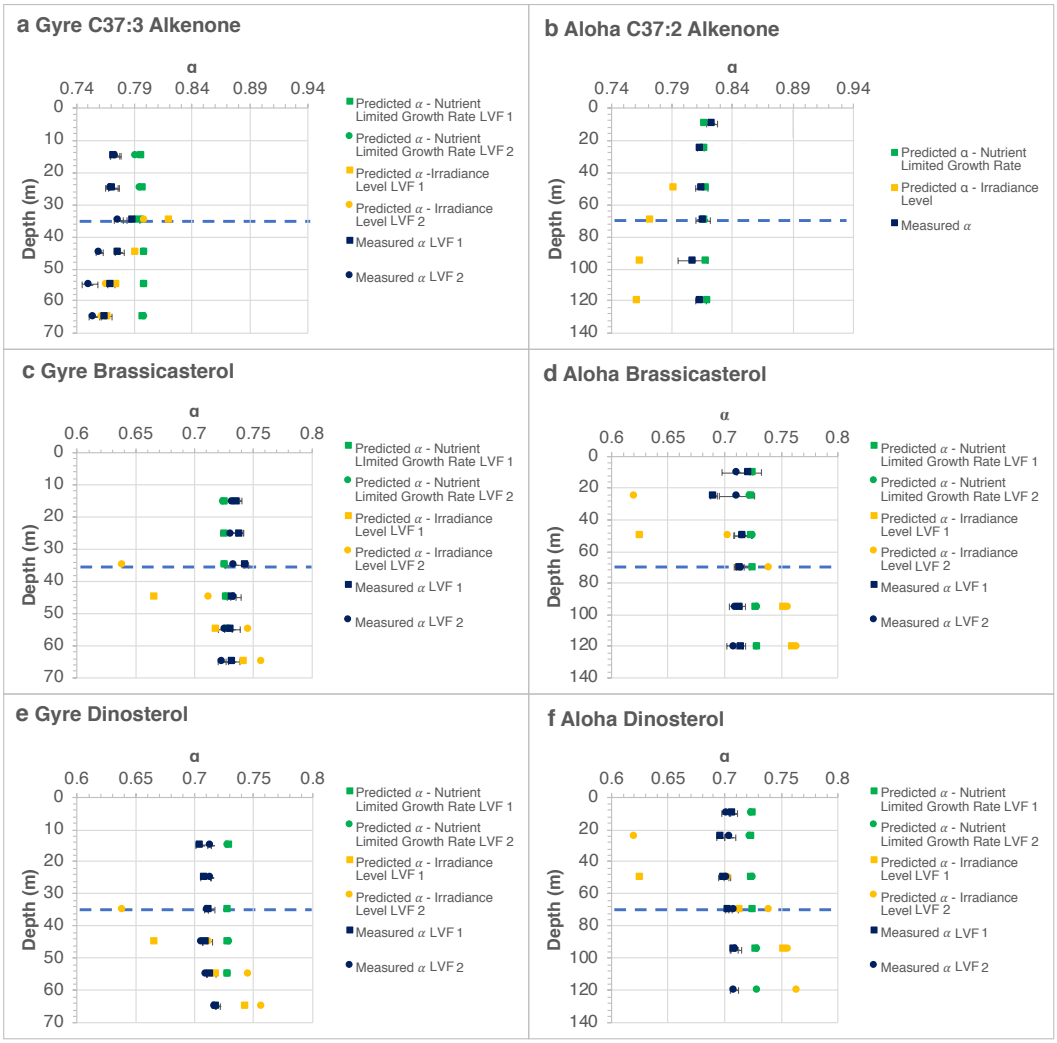

Figure 4.5. α values of (a) Gyre $C_{37:3}$ alkenones, (b) Aloha $C_{37:2}$ alkenones, (c) Gyre brassicasterol, (d) Aloha brassicasterol, (e) Gyre dinosterol, (f) Aloha dinosterol compared to model values of nutrient-limited growth rate α (PN-α, green) and irradiance level growth rate α (PI-α, yellow) for measured α (black) from LVF 1 (squares) and LVF 2 (circles). The dotted line marks the mixed layer at each site (35 m at Gyre and 70 m at Aloha).

4.9 SUPPLEMENTAL TABLES

Table 4.2 Carbonate Chemistry Parameters

Depth	Alkalinity (μmol/kg)	pH	TCO_2 (μmol/kg)	HCO_3 (μmol/kg)	CO_3 (μmol/kg)	CO_2 (μmol/kg)
Gyre						
15	2209.62	8.18	1986.05	1815.11	157.91	13.03
25	2220.92	8.15	1997.44	1826.06	158.22	13.16
35	2243.15	8.16	2015.93	1842.13	160.81	12.98
45	2199.25	8.16	1973.79	1803.56	157.78	12.45
55	2247.04	8.15	2021.31	1849.43	159.06	12.81
65	2188.43	8.11	1986.08	1829.54	142.66	13.88
Aloha						
10	2360.35	8.28	2032.35	1796.30	228.53	10.52
25	2425.32	8.29	2087.35	1837.40	239.45	10.50
50	2374.92	8.28	2044.53	1801.62	232.52	10.39
70	2372.00	8.29	2039.50	1795.61	233.64	10.24
95	2392.60	8.29	2053.97	1805.63	238.19	10.16
120	2411.42	8.24	2106.41	1877.14	217.25	12.03

Alkalinity and pH were measured and the other carbonate chemistry parameters were calculated using CO2SYS (172), in order to obtain CO_2 (aq), which was used for the growth rate calculations. The total pH scale was used for pH calibrations.

Table 4.3 $\delta^{13}C_{DIC}$ of Carbonate Chemistry Parameters

Day	Depth (m)	Natural Abundance $\delta^{13}C_{DIC}$ (‰)	Incubation $\delta^{13}C_{DIC}$ (‰)	Natural Abundance $\delta^{13}C_{CO2(aq)}$ (‰)	Incubation $\delta^{13}C_{CO2(aq)}$ (‰)
Gyre					
1	15	1.46	182.40	-7.91	171.34
1	25	1.41	179.15	-7.96	168.12
1	35	1.41	178.13	-7.96	167.11
1	45	1.42	179.90	-8.13	168.64
1	55	1.34	181.78	-8.28	170.42
1	65	1.20	180.08	-8.49	168.65
2	15	1.43	182.17	-7.94	171.12
2	25	1.42	181.03	-7.95	169.98
2	35	1.39	181.42	-8.15	170.16
2	45	1.42	179.16	-8.18	167.86
2	55	1.28	180.69	-8.40	169.26
2	65	1.16	167.26	-8.56	155.93
Aloha					
1	10	0.99	189.48	-7.57	179.02
1	25	0.88	190.63	-7.68	180.44
1	50	0.87	181.43	-7.69	171.32
1	70	0.82	200.41	-7.76	190.11
1	95	0.74	198.48	-7.85	188.18
1	120	0.78	197.23	-7.83	186.93
2	10	0.83	155.80	-7.73	145.68
2	25	0.95	153.31	-7.61	143.45
2	50	0.82	185.55	-7.74	175.40
2	70	0.77	140.25	-7.81	130.47
2	95	0.75	191.71	-7.85	181.47
2	120	0.74	161.35	-7.87	151.36

$\delta^{13}C_{DIC}$ of both natural abundance seawater and incubation samples was measured in order to obtain the $\delta^{13}C$ values of natural abundance and incubation CO_2 (aq), a parameter in Equation 4.3.

Table 4.4 Gyre CTD Parameters. This table is provided in a separate XLSX file.

Table 4.5 Aloha CTD Parameters. This table is provided in a separate XLSX file.

Table 4.6 Gyre and Aloha Lipid Concentrations

Depth (m)	Day/LVF	$C_{37:2}$ Alkenone (ng/L)	$C_{37:3}$ Alkenone (ng/L)	C16:0 Fatty Acid (ng/L)	C14:0 Fatty Acid (ng/L)	Brassicasterol (ng/L)	Dinosterol (ng/L)
Gyre							
15	1	1.60	3.34	2.80	7.82	5.41	2.16
25	1	0.67	1.72	28.7	85.7	2.92	0.95
35	1	2.17	3.85	0.70	2.56	19.6	9.36
45	1	5.43	13.4	12.8	19.1	9.96	4.49
55	1	6.26	18.6	0.00	0.40	3.79	1.65
65	1	1.14	3.67	42.1	1199	5.33	2.75
15	2	5.25	10.6	20.8	55.4	9.92	3.98
25	2	0.85	5.30	2.92	0.92	20.8	10.2
35	2	2.91	6.58	0.00	0.00	4.95	2.11
45	2	8.05	24.6	14.7	19.1	8.32	3.75
55	2	5.86	17.7	7.51	21.9	13.8	7.54
65	2	1.55	4.41	55.5	117	4.74	2.42
Aloha							
10	1	1.79		4.96	1.85	7.03	3.42
25	1	2.03		0.47	0.32	7.23	2.93
50	1	1.57		0.67	0.16	5.10	2.02
70	1	1.13		2.34	0.80	3.49	1.30
95	1	0.37		1.34	0.48	2.25	1.06
120	1	0.17		4.15	2.01	1.27	0.46
10	2	3.23		16.5	12.6	9.03	4.09
25	2	2.28		6.30	3.09	5.95	2.36
50	2	1.78		0.90	0.23	3.99	1.67
70	2	1.38		7.39	4.90	4.16	1.71
95	2	0.66		2.07	0.75	3.37	1.59
120	2	0.31		0.40	0.17	2.82	1.35

Table 4.7 Gyre δ^2H Lipid Values

Depth (m)	Day/LVF	$\delta^2H_{C37:3\ Alkenone}$	σ	$\delta^2H_{Brassicasterol}$	σ	$\delta^2H_{Dinosterol}$	σ
15	1	-232	5	-268	5	-297	9
25	1	-232	6	-265	4	-295	8
35	1	-215	7	-260	3	-293	9
45	1	-227	5	-270	3	-292	9
55	1	-234	4	-272	9	-291	9
65	1	-238	6	-271	8	-284	6
15	2	-232	6	-272	8	-291	10
25	2	-233	7	-270	13	-286	10
35	2	-227	5	-268	11	-291	5
45	2	-244	4	-270	8	-295	5
55	2	-252	9	-278	8	-297	9
65	2	-248	6	-279	6	-284	9

Table 4.8 Aloha δ^2H Lipid Values

Depth (m)	**Day/LVF**	**$\delta^2H_{C37:2\ Alkenone}$***	**σ**	**$\delta^2H_{Brassicasterol}$**	**σ**	**$\delta^2H_{Dinosterol}$**	**σ**
10	1	-177	5	-278	15	-292	5
25	1	-186	2	-283	6	-302	5
50	1	-184	6	-308	4	-298	8
70	1	-183	7	-282	11	-294	4
95	1	-191	15	-284	5	-289	5
120	1	-185	4	-284	7		
10	2			-287	19	-297	5
25	2			-288.6	10	-293	7
50	2			-287	22	-296	3
70	2			-281	11	-290	6
95	2			-282	10	-290	5
120	2			-290	6	-289	5

*Alkenone δ^2H values are measurements from samples of both days combined

Table 4.9 Gyre α Values. This table is provided in a separate XLSX file.

Table 4.10 Aloha α Values. This table is provided in a separate XLSX file.

Table 4.11 Gyre δ^2H Lipid Values at All Times

Depth (m)	Day and Time	$\delta^2H_{C37:3\ Alkenone}$	σ	$\delta^2H_{Brassicasterol}$	σ	$\delta^2H_{Dinosterol}$	σ
15	1a	-227	6	-272	3		
25	1a	-231	3	-264	6		
35	1a	-208	5	-261	2	-286	4
45	1a	-230	6	-268	1	-283	5
55	1a	-234	2	-273	7		
65	1a	-237	3	-275	9	-283	5
15	1b	-233	1	-264	0	-293	7
25	1b	-232	9	-266	4	-295	12
35	1b	-214	1	-258	0	-298	8
45	1b	-226	3	-271	2	-296	1
55	1b	-235	4	-270	15	-290	5
65	1b	-236	8	-268	10	-285	5
15	1c	-238	2	-269	5	-305	5
25	1c	-238	5				
35	1c	-223	7	-262	1	-289	7
45	1c	-226	7	-272	3	-299	5
55	1c	-233	5	-272	0	-289	3
65	1c	-240	6	-269	4		
15	2a	-232	7	-272	11	-283	4
25	2a	-226	7	-261	5	-290	5
35	2a	-230	3	-273	16	-292	6
45	2a	-248	5	-266	2	-299	5
55	2a	-253	5	-279	2	-292	5
65	2a	-245	5	-274	4	-281	5
15	2b	-230	6	-275	8	-289	5
25	2b	-231	5	-285	6	-290	14
35	2b	-228	2	-271	6	-291	6
45	2b	-243	5	-275	2	-294	1
55	2b	-257	6	-283	1	-293	7
65	2b	-250	3	-284	3	-290	5
15	2c	-233	7	-270	5	-300	5
25	2c	-239	0	-269	3	-197	15
35	2c	-223	8	-262	9	-174	5
45	2c	-245	2	-267	13	-227	5
55	2c	-244	5	-269	13	-305	5
65	2c	-242	3	-278	6	-278	5

Table 4.12 Aloha δ^2H Lipid Values at All Times

Depth (m)	Day and Time	$\delta^2H_{C37:2\ Alkenone}$*	σ	$\delta^2H_{Brassicasterol}$	σ	$\delta^2H_{Dinosterol}$	σ
10	1a	-177	5	-295	1		
25	1a	-186	2	-310	4		
50	1a	-184	6	-290	2	-296	5
70	1a	-183	7	-301	4	-298	5
95	1a	-191	15	-310	4	-289	5
120	1a	-185	4	-310	1		
10	1b			-267	12	-292	5
25	1b			-307	4		
50	1b			-279	3	-290	5
70	1b			-282	1	-293	5
95	1b			-305	4		
120	1b			-269	1		
10	1c			-287	1		
25	1c			-280	6	-302	5
50	1c			-281	3	-304	5
70	1c			-293	7		
120	1c			-286	10		
10	2a			-274	3	-297	5
25	2a			-272	4	-300	5
50	2a			-285	7	-295	5
70	2a			-272	4	-294	5
95	2a			-287	3	-289	5
120	2a			-287	2	-291	5
10	2b			-283	1	-290	5
25	2b			-280	0	-285	5
50	2b			-286	1	-296	1
70	2b			-278	2	-288	2
95	2b			-287	3	-284	5
120	2b			-296	7	-285	5
10	2c			-292	6	-300	2
25	2c			-290	7	-294	5
50	2c			-277	1	-297	5
70	2c			-290	5	-289	8
95	2c			-282	12	-292	2
120	2c			-290	5	-291	5

Table 4.13 Gyre $\delta^{13}C$ Alkenone and Sterol Values. This table is provided in a separate XLSX file.

Table 4.14 Gyre $\delta^{13}C$ Fatty Acid Values. This table is provided in a separate XLSX file.

Table 4.15 Gyre μ (d^{-1}) Values. This table is provided in a separate XLSX file.

Table 4.16 Aloha $\delta^{13}C$ Lipid Values. This table is provided in a separate XLSX file.

Table 4.17 Aloha μ (d^{-1}) Values. This table is provided in a separate XLSX file.

4.10 SUPPLEMENTAL FIGURES

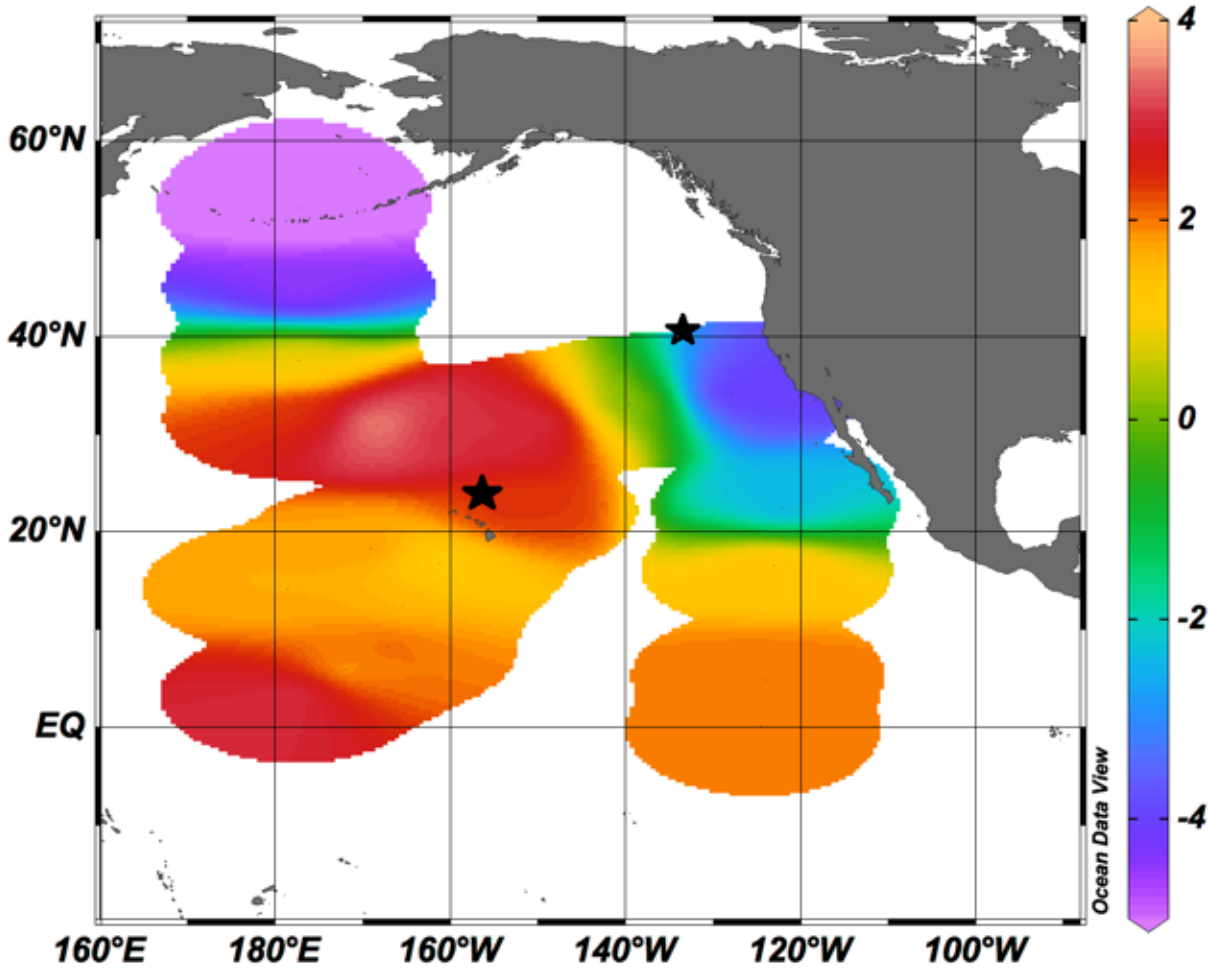

Figure 4.6. Surface water δ^2H values in the North Pacific (173). Units for the color bar are ‰. The field sites in this study are marked, with Gyre at 41°N 132°W and Aloha at 22°N 158°W.

BIBLIOGRAPHY

1. Swart PK (2013) Coral Reefs: Canaries of the Sea, Rainforest of the Ocean. *Nat Educ Knowl* 4(3):5.
2. Why do we care about reefs? (2017) *Coral Reef Alliance*.
3. Erez J, Reynaud S, Silverman J, Schneider K, Allemand D (2011) Coral Calcification Under Ocean Acidification and Global Change. *Coral Reefs: An Ecosystem in Transition*, eds Dubinsky Z, Stambler N, pp 151–176.
4. Edmunds PJ, Brown D, Moriarty V (2012) Interactive effects of ocean acidification and temperature on two scleractinian corals from Moorea, French Polynesia. *Glob Chang Biol* 18(7):2173–2183.
5. Schneider K, Erez J (2006) The effect of carbonate chemistry on calcification and photosynthesis in the hermatypic coral Acropora eurystoma. *Limnol Oceanogr* 51(3):1284–1293.
6. Marubini F, Ferrier-Pagès C, Furla P, Allemand D (2008) Coral calcification responds to seawater acidification: A working hypothesis towards a physiological mechanism. *Coral Reefs* 27(3):491–499.
7. PMEL Carbon Program A primer on pH. *NOAA*. Available at: https://www.pmel.noaa.gov/co2/story/A+primer+on+pH [Accessed May 7, 2018].
8. Caldeira K, Wickett ME (2003) Anthropogenic carbon and ocean pH. *Nature* 425(6956):365–365.
9. Feely RA, et al. (2004) Impact of Anthropogenic CO2 on the CaCO3 System in the Oceans. *Science* 305(5682):362–366.
10. Silverman J, Lazar B, Cao L, Caldeira K, Erez J (2009) Coral reefs may start dissolving

when atmospheric CO2 doubles. *Geophys Res Lett* 36(5):1–5.

11. Pachauri RK, Meyer LA eds. (2014) IPCC 2014: Climate Change 2014: Synthesis Report. *IPCC* (Contribution of Working Groups I, II, and III to the Fifth Assessment Report of the Intergovernmental Panel on Climate Change, Geneva). Available at: http://www.ipcc.ch/report/ar5/syr/ [Accessed May 7, 2018].
12. Gladfelter EH (1982) Coral Reefs Skeletal Development in Acropora cervicornis : I . Patterns of Calcium Carbonate Accretion in the Axial Corallite. *Coral Reefs* 1:45–51.
13. Gladfelter EH (1984) Skeletal development in Acropora cervicornis - III. A comparison of monthly rates of linear extension and calcium carbonate accretion measured over a year. *Coral Reefs* 3(1):51–57.
14. Gladfelter EH (2007) Skeletal development in Acropora palmata (Lamarck 1816): A scanning electron microscope (SEM) comparison demonstrating similar mechanisms of skeletal extension in axial versus encrusting growth. *Coral Reefs* 26(4):883–892.
15. DeYoreo JJ, Vekilov PG (2003) Principles of Crystal Nucleation and Growth. *Rev Mineral Geochemistry* 54(1):57–93.
16. De Yoreo JJ, et al. (2015) Crystallization by particle attachment in synthetic, biogenic, and geologic environments. *Science (80-)* 349(6247):aaa6760–aaa6760.
17. Erez J, Braun A (2007) Calcification in hermatypic corals is based on direct seawater supply to the biomineralization site. *Geochim Cosmochim Acta* 71(15 (Supplement 1)):A260.
18. Cohen AL, McConnaughey TA (2003) Geochemical Perspectives on Coral Mineralization. *Rev Mineral Geochemistry* 54(1):151–187.
19. Gagnon AC, Adkins JF, Erez J (2012) Seawater transport during coral biomineralization.

Earth Planet Sci Lett 329–330:150–161.

20. Tambutté E, et al. (2012) Calcein labelling and electrophysiology: insights on coral tissue permeability and calcification. *Proceedings Biol Sci* 279(1726):19–27.
21. Allison N, Cohen I, Finch AA, Erez J, Tudhope AW (2014) Corals concentrate dissolved inorganic carbon to facilitate calcification. *Nat Commun* 5:5741.
22. Al-Horani FA, Al-Moghrabi SM, de Beer D (2003) The mechanism of calcification and its relation to photosynthesis and respiration in the scleractinian coral Galaxea fascicularis. *Mar Biol* 142(3):419–426.
23. Venn A, Tambutté E, Holcomb M, Allemand D, Tambutté S (2011) Live tissue imaging shows reef corals elevate pH under their calcifying tissue relative to seawater. *PLoS One* 6(5). doi:10.1371/journal.pone.0020013.
24. Venn AA, et al. (2013) Impact of seawater acidification on pH at the tissue-skeleton interface and calcification in reef corals. *Proc Natl Acad Sci* 110(5):1634–1639.
25. Gagnon AC (2013) Coral calcification feels the acid. *Proc Natl Acad Sci U S A* 110(5):1567–8.
26. DeCarlo TM, et al. (2017) Coral calcifying fluid aragonite saturation states derived from Raman spectroscopy. *Biogeosciences* 14(22):5253–5269.
27. Sevilgen DS, et al. (2019) Full in vivo characterization of carbonate chemistry at the site of calcification in corals. *Sci Adv* 5(1):eaau7447.
28. Goreau TF (1959) the Physiology of Skeleton Formation in Corals. I. a Method for Measuring the Rate of Calcium Deposition By Corals Under Different Conditions. *Biol Bull* 116(1):59–75.
29. Mitterer RM (1978) Amino acid composition and metal binding capability of the skeletal

protein of corals. *Bull Mar Sci* 28(1):173–180.

30. Constantz B, Weiner S (1988) Acidic macromolecules associated with the mineral phase of scleractinian coral skeletons. *J Exp Zool* 248(3):253–258.
31. Ingalls AE, Lee C, Druffel ERM (2003) Preservation of organic matter in mound-forming coral skeletons. *Geochim Cosmochim Acta* 67(15):2827–2841.
32. Addadi L, Weiner S (1985) Interactions between acidic proteins and crystals: stereochemical requirements in biomineralization. *Proc Natl Acad Sci* 82(12):4110–4114.
33. Weiner S, Addadi L (1991) Acidic macromolecules of mineralized tissues: the controllers of crystal formation. *Biochem Isr* (July).
34. Drake JL, et al. (2013) Proteomic analysis of skeletal organic matrix from the stony coral Stylophora pistillata. *Proc Natl Acad Sci* 110(10):3788–3793.
35. Mass T, et al. (2013) Cloning and characterization of four novel coral acid-rich proteins that precipitate carbonates in vitro. *Curr Biol* 23(12):1126–1131.
36. Heywood BR, Mann S (1994) Molecular Construction of Oriented Inorganic Materials: Controlled Nucleation of Calcite and Aragonite under Compressed Langmuir Monolayers. *Chem Mater* 6:311–318.
37. Mann S, et al. (1993) Crystallization at Inorganic-Organic Interfaces : Biominerals and Biomimetic Synthesis Published by : American Association for the Advancement of Science Crystallization at Inorganic- Organic Interfaces : Biominerals and Biomimetic Synthesis. *Science (80-)* 261(5126):1286–1292.
38. Aizenberg J, Black AJ, Whitesides GM (1999) Oriented growth of calcite controlled by self-assembled monolayers of functionalized alkanethiols supported on gold and silver. *J Am Chem Soc* 121(18):4500–4509.

39. Teng HH, Dove PM, Orme CA, De Yoreo JJ JJ De, Isdale PJ (1998) Thermodynamics of Calcite Growth: Baseline for Understanding Biomineral Formation. *Science (80-)* 282(5389):724–727.

40. Orme CA, et al. (2001) Formation of chiral morphologies through selective binding of amino acids to calcite surface steps. *Lett to Nat* 411:775–779.

41. Hu Q, et al. (2012) The thermodynamics of calcite nucleation at organic interfaces: Classical vs. non-classical pathways. *Faraday Discuss* 159:509.

42. Hamm LM, et al. (2014) Reconciling disparate views of template-directed nucleation through measurement of calcite nucleation kinetics and binding energies. *Proc Natl Acad Sci* 111(4):1304–1309.

43. Mass T, Drake JL, Peters EC, Jiang W, Falkowski PG (2014) Immunolocalization of skeletal matrix proteins in tissue and mineral of the coral Stylophora pistillata. *Proc Natl Acad Sci U S A* 111(35):12728–33.

44. Mass T, et al. (2016) Temporal and spatial expression patterns of biomineralization proteins during early development in the stony coral Pocillopora damicornis. *Proc R Soc London B Biol Sci* 283(1829). Available at: http://rspb.royalsocietypublishing.org/content/283/1829/20160322.abstract.

45. Akiva A, et al. (2018) Minerals in the pre-settled coral Stylophora pistillata crystallize via protein and ion changes. *Nat Commun* 9(1):1880.

46. Mass T, Drake JL, Heddleston JM, Falkowski Correspondence PG, Falkowski PG (2017) Nanoscale Visualization of Biomineral Formation in Coral Proto-Polyps. *Curr Biol* 27:3191-3196.e3.

47. Drake JL, et al. (2017) Molecular and geochemical perspectives on the influence of CO_2

on calcification in coral cell cultures. *Limnol Oceanogr*. doi:10.1002/lno.10617.

48. Gavriel R, et al. (2018) The Coral Protein CARP3 Acts from a Disordered Mineral Surface Film to Divert Aragonite Crystallization in Favor of Mg-Calcite. *Adv Funct Mater*:1707321.

49. Laipnik R, et al. (2020) Coral acid rich protein selects vaterite polymorph in vitro. *J Struct Biol* 209(2):107431.

50. Jiang L-Q, et al. (2015) Climatological distribution of aragonite saturation state in the global oceans. *Global Biogeochem Cycles* 29(10):1656–1673.

51. Venn A, Tambutté E, Holcomb M, Allemand D, Tambutté S (2011) Live Tissue Imaging Shows Reef Corals Elevate pH under Their Calcifying Tissue Relative to Seawater. *PLoS One* 6(5):e20013.

52. Ramos-Silva P, et al. (2013) The Skeletal Proteome of the Coral Acropora millepora: The Evolution of Calcification by Co-Option and Domain Shuffling. *Mol Biol Evol* 30(9):2099–2112.

53. Takeuchi T, Yamada L, Shinzato C, Sawada H, Satoh N (2016) Stepwise Evolution of Coral Biomineralization Revealed with Genome-Wide Proteomics and Transcriptomics. *PLoS One* 11(6):e0156424.

54. Stolarski J (2003) Three-diensional micro- and nanostructural characteristics of the scleractinian coral skeleton: A biocalcification proxy. *Acta Palaeontol Pol* 48(4):497–530.

55. Emerson SR, Hedges JI (2008) *Chemical Oceanography and the Marine Carbon Cycle* (Cambridge University Press, Cambridge). Fourth.

56. Mucci A, Canuel R, Zhong S (1989) THE SOLUBILITY OF CALCITE AND ARAGONITE IN SULFATE- FREE SEAWATER AND THE SEEDED GROWTH

KINETICS AND COMPOSITION OF THE PRECIPITATES AT 25 °C. *Chem Geol Elsevier Sci Publ BV* 74:309–320.

57. De Yoreo JJ, Vekilov PG (2003) Principles of Crystal Nucleation and Growth. *Rev Mineral Geochemistry* 54(1):57–93.

58. Markov I V (2003) *Crystal Growth for Beginners: Fundamentals of Nuclation, Crystal Growth and Epitaxy* (WORLD SCIENTIFIC). 2nd Ed. doi:10.1142/5172.

59. Sun W, Jayaraman S, Chen W, Persson KA, Ceder G (2015) Nucleation of metastable aragonite CaCO3 in seawater. *Proc Natl Acad Sci U S A* 112(11):3199–204.

60. Giuffre AJ, et al. Polysaccharide chemistry regulates kinetics of calcite nucleation through competition of interfacial energies. doi:10.1073/pnas.1222162110.

61. Westin K-J, Rasmuson ÅC (2005) Nucleation of calcium carbonate in presence of citric acid, DTPA, EDTA and pyromellitic acid. *J Colloid Interface Sci* 282(2):370–379.

62. Söhnel O (1982) Electrolyte crystal-aqueous solution interfacial tensions from crystallization data. *J Cryst Growth* 57(1):101–108.

63. Söhnel O, Mullin JW (1978) A method for the determination of precipitation induction periods. *J Cryst Growth* 44(4):377–382.

64. Verdoes D, Kashchiev D, van Rosmalen GM (1992) Determination of nucleation and growth rates from induction times in seeded and unseeded precipitation of calcium carbonate. *J Cryst Growth* 118(3–4):401–413.

65. Gómez-Morales J, Torrent-Burgués J, Rodríguez-Clemente R (1996) Nucleation of calcium carbonate at different initial pH conditions. *J Cryst Growth* 169(2):331–338.

66. Manoli F, Kanakis J, Malkaj P, Dalas E (2002) The effect of aminoacids on the crystal growth of calcium carbonate. *J Cryst Growth* 236(1–3):363–370.

67. Elhadj S, De Yoreo JJ, Hoyer JR, Dove PM (2006) *Role of molecular charge and hydrophilicity in regulating the kinetics of crystal growth*.

68. Reynaud-Vaganay S, Gattuso J-P, Cuif J-P, Jaubert J, Juillet-Leclerc A (1999) A novel culture technique for scleractinian corals: application to investigate changes in skeletal d180 as a function of temperature. *Mar Ecol Prog Ser* 180:121–130.

69. Larsen A (2020) Role of Aragonite Nucleation Rate and Crystal Morphology in Lateral Skeletal Growth in the Tropical Coral Acropora microphthalma. Dissertation (University of Washington).

70. Gangstø R, et al. (2008) *Modeling the marine aragonite cycle: changes under rising carbon dioxide and its role in shallow water CaCO 3 dissolution* Available at: www.biogeosciences.net/5/1057/2008/ [Accessed March 7, 2019].

71. Sevilgen DS, et al. (2019) Full in vivo characterization of carbonate chemistry at the site of calcification in corals. *Sci Adv* 5(1):eaau7447.

72. Teng HH, Dove PM, Orme CA, De Yoreo JJ (1998) Thermodynamics of calcite growth: Baseline for understanding biomineral formation. *Science (80-)* 282(5389):724–727.

73. Hu Q, et al. (2012) The thermodynamics of calcite nucleation at organic interfaces: Classical vs. non-classical pathways. *Faraday Discuss* 159(1):509.

74. Mann S (1988) Molecular recognition in biomineralization. *Nature* 332(6160):119–124.

75. Weiner S, Addadi L (2011) Crystallization Pathways in Biomineralization. *Annu Rev Mater Res* 41(1):21–40.

76. Orme CA, et al. (2001) Formation of chiral morphologies through selective binding of amino acids to calcite surface steps. *Nature* 411(6839):775–779.

77. Marin F, Luquet G (2008) Unusually Acidic Proteins in Biomineralization. *Handbook of*

Biomineralization: Biological Aspects and Structure Formation (Wiley-VCH Verlag GmbH & Co. KGaA), pp 273–290.

78. Giuffre AJ, Hamm LM, Han N, De Yoreo JJ, Dove PM (2013) Polysaccharide chemistry regulates kinetics of calcite nucleation through competition of interfacial energies. *Proc Natl Acad Sci U S A* 110(23):9261–6.

79. Njegić Džakula B, et al. (2019) In Vitro Coral Biomineralization under Relevant Aragonite Supersaturation Conditions. *Chem - A Eur J*:10616–10624.

80. Finney AR, Innocenti Malini R, Freeman CL, Harding JH (2020) Amino Acid and Oligopeptide Effects on Calcium Carbonate Solutions. *Cryst Growth Des* 20(5):3077–3092.

81. Finney AR, Rodger PM (2012) Probing the structure and stability of calcium carbonate pre-nucleation clusters. *Faraday Discuss* 159(1):47–60.

82. Picker A, Kellermeier M, Seto J, Gebauer D, Cölfen H (2012) The multiple effects of amino acids on the early stages of calcium carbonate crystallization. *Zeitschrift Fur Kristallographie* (De Gruyter), pp 744–757.

83. Tobler DJ, et al. (2014) The Effect of Aspartic Acid and Glycine on Amorphous Calcium Carbonate (ACC) Structure, Stability and Crystallization. *Procedia Earth Planet Sci* 10:143–148.

84. Montanari G, et al. (2016) Effect of Aspartic Acid and Glycine on Calcite Growth. *Cryst Growth Des* 16(9):4813–4821.

85. Raiteri P, et al. (2012) Exploring the influence of organic species on pre- and post-nucleation calcium carbonate. *Faraday Discuss* 159(1):61–85.

86. Elhadj S, et al. (2006) Peptide Controls on Calcite Mineralization: Polyaspartate Chain

Length Affects Growth Kinetics and Acts as a Stereochemical Switch on Morphology. doi:10.1021/cg050288.

87. De Yoreo JJ, Wierzbicki A, Dove PM (2007) New insights into mechanisms of biomolecular control on growth of inorganic crystals. *CrystEngComm* 9(12):1144–1152.

88. Njegić-Džakula B, Brečević L, Falini G, Kralj D (2009) Calcite crystal growth kinetics in the presence of charged synthetic polypeptides. *Cryst Growth Des* 9(5):2425–2434.

89. De Yoreo JJ, et al. (2015) CRYSTAL GROWTH. Crystallization by particle attachment in synthetic, biogenic, and geologic environments. *Science* 349(6247):aaa6760.

90. Gebauer D, Cölfen H, Verch A, Antonietti M (2009) The Multiple Roles of Additives in $CaCO_3$ Crystallization: A Quantitative Case Study. *Adv Mater* 21(4):435–439.

91. Kelley LA, Mezulis S, Yates CM, Wass MN, Sternberg MJE (2015) The Phyre2 web portal for protein modeling, prediction and analysis. *Nat Protoc* 10(6):845–858.

92. Kasper S, et al. (2014) Salinity changes in the Agulhas leakage area recorded by stable hydrogen isotopes of C_{37} alkenones during Termination I and II. *Clim Past* 10(1):251–260.

93. van der Meer MTJ, et al. (2007) Hydrogen isotopic compositions of long-chain alkenones record freshwater flooding of the Eastern Mediterranean at the onset of sapropel deposition. *Earth Planet Sci Lett* 262(3–4):594–600.

94. Nelson DB, Sachs JP (2016) Galápagos hydroclimate of the Common Era from paired microalgal and mangrove biomarker 2H/1H values. *Proc Natl Acad Sci U S A* 113(13):3476–81.

95. Sachs JP, et al. (2009) Southward movement of the Pacific intertropical convergence zone AD 1400–1850. *Nat Geosci* 2(7):519–525.

96. Smittenberg RH, Saenger C, Dawson MN, Sachs JP (2011) Compound-specific D/H ratios of the marine lakes of Palau as proxies for West Pacific Warm Pool hydrologic variability. *Quat Sci Rev* 30(7–8):921–933.

97. van der Meer M, et al. (2008) Molecular isotopic and dinoflagellate evidence for Late Holocene freshening of the Black Sea. *Earth Planet Sci Lett* 267(3–4):426–434.

98. Richey JN, Sachs JP (2016) Precipitation changes in the western tropical Pacific over the past millennium. *Geology* 44(8):671–674.

99. Vasiliev I, et al. (2017) How dry was the Mediterranean during the Messinian salinity crisis? *Palaeogeogr Palaeoclimatol Palaeoecol* 471:120–133.

100. Simon MH, et al. (2015) Salt exchange in the Indian-Atlantic Ocean Gateway since the Last Glacial Maximum: A compensating effect between Agulhas Current changes and salinity variations? *Paleoceanography* 30(10):1318–1327.

101. Vasiliev I, Reichart G-J, Krijgsman W (2013) Impact of the Messinian Salinity Crisis on Black Sea hydrology—Insights from hydrogen isotopes analysis on biomarkers. *Earth Planet Sci Lett* 362:272–282.

102. Englebrecht AC, Sachs JP (2005) Determination of sediment provenance at drift sites using hydrogen isotopes and unsaturation ratios in alkenones. *Geochim Cosmochim Acta* 69(17):4253–4265.

103. Zhang Z, Sachs JP (2007) Hydrogen isotope fractionation in freshwater algae: I. Variations among lipids and species. *Org Geochem* 38(4):582–608.

104. Craig H, Gordon LI (1965) *Deuterium and Oxygen 18 Variations in the Ocean and the Marine Atmosphere* (Consiglio nazionale delle richerche, Laboratorio de geologia nucleare) Available at:

https://books.google.com/books/about/Deuterium_and_Oxygen_18_Variations_in_th.html?id=6wIKAQAAIAAJ&pgis=1 [Accessed May 8, 2016].

105. Craig H (1961) Isotopic Variations in Meteoric Waters. *Science* 133(3465):1702–3.

106. Gat JR (1996) Oxygen and Hydrogen Isotopes in the Hydrologic Cycle. *Annu Rev Earth Planet Sci* 24:225–62.

107. Sessions AL, Burgoyne TW, Schimmelmann A, Hayes JM (1999) Fractionation of hydrogen isotopes in lipid biosynthesis, Org. *Org Geochem* 30:1193–1200.

108. Chivall D, et al. (2014) The effects of growth phase and salinity on the hydrogen isotopic composition of alkenones produced by coastal haptophyte algae. *Geochim Cosmochim Acta* 140:381–390.

109. M'boule D, et al. (2014) Salinity dependent hydrogen isotope fractionation in alkenones produced by coastal and open ocean haptophyte algae. *Geochim Cosmochim Acta* 130:126–135.

110. Nelson DB, Sachs JP (2014) The influence of salinity on D/H fractionation in alkenones from saline and hypersaline lakes in continental North America. *Org Geochem* 66:38–47.

111. Sachs JP, Maloney AE, Gregersen J, Paschall C (2016) Effect of salinity on 2H/1H fractionation in lipids from continuous cultures of the coccolithophorid Emiliania huxleyi. *Geochim Cosmochim Acta* 189:96–109.

112. Sachse D, Sachs JP (2008) Inverse relationship between D/H fractionation in cyanobacterial lipids and salinity in Christmas Island saline ponds. *Geochim Cosmochim Acta* 72(3):793–806.

113. Schouten S, et al. (2006) The effect of temperature, salinity and growth rate on the stable hydrogen isotopic composition of long chain alkenones produced by <I>Emiliania

huxleyi</I> and <I>Gephyrocapsa oceanica</I>. *Biogeosciences* 3(1):113–119.

114. Maloney AE, Shinneman ALC, Hemeon K, Sachs JP (2016) Exploring lipid 2 H/ 1 H fractionation mechanisms in response to salinity with continuous cultures of the diatom Thalassiosira pseudonana. *Org Geochem* 101:154–165.

115. Weiss GM, Pfannerstill EY, Schouten S, Sinninghe Damsté JS, van der Meer MTJ (2017) Effects of alkalinity and salinity at low and high light intensity on hydrogen isotope fractionation of long-chain alkenones produced by <i>Emiliania huxleyi</i> *Biogeosciences* 14(24):5693–5704.

116. Estep MF, Hoering TC (1980) Biogeochemistry of the stable hydrogen isotopes. *Geochim Cosmochim Acta* 44(8):1197–1206.

117. Wolhowe MD, Prahl FG, Probert I, Maldonado M (2009) Growth phase dependent hydrogen isotopic fractionation in alkenone-producing haptophytes. *Biogeosciences Discuss* 6(2):4165–4200.

118. Zhang Z, Sachs JP, Marchetti A (2009) Hydrogen isotope fractionation in freshwater and marine algae: II. Temperature and nitrogen limited growth rate effects. *Org Geochem* 40(3):428–439.

119. Sachs JP, Kawka OE (2015) The Influence of Growth Rate on 2H/1H Fractionation in Continuous Cultures of the Coccolithophorid Emiliania huxleyi and the Diatom Thalassiosira pseudonana. *PLoS One* 10(11):e0141643.

120. Wolhowe MD, Prahl FG, Langer G, Oviedo AM, Ziveri P (2015) Alkenone δD as an ecological indicator: A culture and field study of physiologically-controlled chemical and hydrogen-isotopic variation in C37 alkenones. *Geochim Cosmochim Acta* 162:166–182.

121. van der Meer MTJ, et al. (2015) Large effect of irradiance on hydrogen isotope

fractionation of alkenones in Emiliania huxleyi. *Geochim Cosmochim Acta* 160:16–24.

122. Sachs JP, Maloney AE, Gregersen J (2017) Effect of light on 2 H/ 1 H fractionation in lipids from continuous cultures of the diatom Thalassiosira pseudonana. doi:10.1016/j.gca.2017.04.008.

123. Marlowe IT, et al. (2007) Long chain (n -C 37 –C 39) alkenones in the Prymnesiophyceae. Distribution of alkenones and other lipids and their taxonomic significance. *Br Phycol J* 19(3):203–216.

124. Volkman JK, Barrerr SM, Blackburn SI, Sikes EL (1995) Alkenones in Gephyrocapsa oceanica: Implications for studies of paleoclimate. *Geochim Cosmochim Acta* 59(3):513–520.

125. Volkman JK, Eglinton G, Corner EDS, Forsberg TEV (1980) Long-chain alkenes and alkenones in the marine coccolithophorid Emiliania huxleyi. *Phytochemistry* 19(12):2619–2622.

126. Mansour MP, Volkman JK, Jackson AE, Blackburn SI (1999) The Fatty Acid and Sterol Composition of Five Marine Dinoflagellates. *J Phycol* 35(4):710–720.

127. Volkman JK (2003) Sterols in microorganisms. *Appl Microbiol Biotechnol* 60(5):495–506.

128. Volkman JK, Barrett SM, Dunstan GA, Jeffrey SW (1993) Geochemical significance of the occurrence of dinosterol and other 4-methyl sterols in a marine diatom. *Org Geochem* 20(1):7–15.

129. Rampen SW, Abbas BA, Schouten S, Sinninghe Damste JS (2010) A comprehensive study of sterols in marine diatoms (Bacillariophyta): Implications for their use as tracers for diatom productivity. *Limnol Oceanogr* 55(1):91–105.

130. Volkman JK (1986) A review of sterol markers for marine and terrigenous organic matter. *Org Geochem* 9(2):83–99.

131. Prahl FG, Wakeham SG (1987) Calibration of unsaturation patterns in long-chain ketone compositions for palaeotemperature assessment. *Nature* 330(6146):367–369.

132. Müller MN, Trull TW, Hallegraeff GM (2017) Independence of nutrient limitation and carbon dioxide impacts on the Southern Ocean coccolithophore Emiliania huxleyi. *ISME J* 11(8):1777–1787.

133. Sachse D, et al. (2012) Molecular Paleohydrology: Interpreting the Hydrogen-Isotopic Composition of Lipid Biomarkers from Photosynthesizing Organisms. *Annu Rev Earth Planet Sci* 40(1):221–249.

134. Heinzelmann SM, et al. (2015) Impact of metabolism and growth phase on the hydrogen isotopic composition of microbial fatty acids. *Front Microbiol* 6:408.

135. Popp BN, Prahl FG, Wallsgrove RJ, Tanimoto J (2006) Seasonal patterns of alkenone production in the subtropical oligotrophic North Pacific. *Paleoceanography* 21(1):n/a-n/a.

136. Popp BN, et al. (2006) A new method for estimating growth rates of alkenone-producing haptophytes. *Limnol Oceanogr Methods* 4(4):114–129.

137. Prahl FG, Popp BN, Karl DM, Sparrow MA (2005) Ecology and biogeochemistry of alkenone production at Station ALOHA. *Deep Sea Res Part I Oceanogr Res Pap* 52(5):699–719.

138. Doose H, Prahl FG, Lyle MW (1997) Biomarker temperature estimates for modern and last glacial surface waters of the California Current System between 33° and 42°N. *Paleoceanography* 12(4):615–622.

139. Lyle M, et al. (1992) Paleoproductivity and carbon burial across the California Current:

The multitracers transect, 42°N. *Paleoceanography* 7(3):251–272.

140. Hickey BM (1979) The California current system—hypotheses and facts. *Prog Oceanogr* 8(4):191–279.

141. Roden G (1991) Subarctic-subtropical transition zone of the North Pacific: large-scale aspects and mesoscale structure. *NOAA Tech Rep NMFS*. Available at: http://citeseerx.ist.psu.edu/viewdoc/download?doi=10.1.1.214.1552&rep=rep1&type=pdf#page=7 [Accessed June 28, 2016].

142. Polovina JJ, Howell E, Kobayashi DR, Seki MP (2001) The transition zone chlorophyll front, a dynamic global feature defining migration and forage habitat for marine resources. *Prog Oceanogr* 49(1):469–483.

143. Ribalet F, et al. (2010) Unveiling a phytoplankton hotspot at a narrow boundary between coastal and offshore waters. *Proc Natl Acad Sci* 107(38):16571–16576.

144. Booth BC, Lewin J, Postel JR (1993) Temporal variation in the structure of autotrophic and heterotrophic communities in the subarctic Pacific. *Prog Oceanogr* 32(1–4):57–99.

145. Booth BC (1988) Size classes and major taxonomic groups of phytoplankton at two locations in the subarctic pacific ocean in May and August, 1984. *Mar Biol* 97(2):275–286.

146. Taylor FJR, Waters RE (1982) Spring phytoplankton in the Subarctic North Pacific Ocean. *Mar Biol* 67(3):323–335.

147. Honjo S, Okada H (1974) Community structure of coccolithophores in the photic layer of the mid-Pacific. *Micropaleontology*. Available at: http://www.jstor.org/stable/1485061 [Accessed April 30, 2016].

148. Okada H, Honjo S (1973) The distribution of oceanic coccolithophorids in the Pacific.

Deep Sea Res Oceanogr Abstr 20(4):355–374.

149. Karl DM, Lukas R (1996) The Hawaii Ocean Time-series (HOT) program: Background, rationale and field implementation. *Deep Sea Res Part II Top Stud Oceanogr* 43(2–3):129–156.

150. Venrick EL (1999) Phytoplankton species structure in the central North Pacific 1973-1996: variability and persistence. *J Plankton Res* 21(6):1029–1042.

151. Venrick EL (1988) The vertical distributions of chlorophyll and phytoplankton species in the North Pacific central environment. *J Plankton Res* 10(5):987–998.

152. Venrick EL (1997) Comparison of the phytoplankton species composition and structure in the Climax area (1973-1985) with that of station ALOHA (1994). *Limnol Oceanogr* 42(7):1643–1648.

153. Cortés MY, Bollmann J, Thierstein HR (2001) Coccolithophore ecology at the HOT station ALOHA, Hawaii. *Deep Sea Res Part II Top Stud Oceanogr* 48(8–9):1957–1981.

154. Nelson DB, Sachs JP (2013) Concurrent purification of sterols, triterpenols and alkenones from sediments for hydrogen isotope analysis using high performance liquid chromatography. *Org Geochem* 64:19–28.

155. Polissar PJ, Freeman KH, Rowley DB, McInerney FA, Currie BS (2009) Paleoaltimetry of the Tibetan Plateau from D/H ratios of lipid biomarkers. *Earth Planet Sci Lett* 287(1–2):64–76.

156. Wolhowe MD, Prahl FG, White AE, Popp BN, Rosas-Navarro A (2014) A biomarker perspective on coccolithophorid growth and export in a stratified sea. *Prog Oceanogr* 122:65–76.

157. Torres ME, Mix AC, Rugh WD (2005) Precise δ^{13} C analysis of dissolved inorganic

carbon in natural waters using automated headspace sampling and continuous-flow mass spectrometry. *Limnol Oceanogr Methods* 3(8):349–360.

158. Monterey G, Levitus S (1997) Seasonal variability of the global ocean mixed layer depth. Available at: https://scholar.google.com/scholar?hl=en&q=seasonal+variability+of+the+global+ocean+mixed+layer+depth+levitus&btnG=&as_sdt=1%2C48&as_sdtp=#0 [Accessed April 29, 2016].

159. Chisholm SW, Brand LE (1981) Persistence of cell division phasing in marine phytoplankton in continuous light after entrainment to light: Dark cycles. *J Exp Mar Bio Ecol* 51(2–3):107–118.

160. Van Dolah FM, Leighfield TA (1999) Diel Phasing of the Cell-Cycle in the Florida Red Tide Dinoflagellate, Gymnodinium breve. *J Phycol* 35(6):1404–1411.

161. Fitt KW, Trench RK (1983) The Relation of Diel Patterns of Cell Division to Diel Patterns of Motility in the Symbiotic Dinoflagellate Symbiodinium microadria ticum Freudenthal in Culture. *New Phytol* 94(3):421–432.

162. Hitchcock GL (1980) Diel variation in chlorophyll a, carbohydrate and protein content of the marine diatom Skeletonema costatum. *Mar Biol* 57(4):271–278.

163. Smayda TJ (1975) Phased cell division in natural populations of the marine diatom Ditylum brightwelli and the potential significance of diel phytoplankton behavior in the sea. *Deep Sea Res Oceanogr Abstr* 22(3):151–165.

164. Tang EPY (1996) Why do dinoflagellates have lower growth rates? *J Phycol* 32(1):80–84.

165. Amo M, et al. (2010) *Sterol composition of dinoflagellates: Different abundance and composition in heterotrophic species and resting cysts* Available at:

https://pdfs.semanticscholar.org/6584/da9e77745b63855cee0d6437022f7ba6c12b.pdf [Accessed August 9, 2018].

166. Zhang X, Gillespie AL, Sessions AL (2009) Large D/H variations in bacterial lipids reflect central metabolic pathways. *Proc Natl Acad Sci U S A* 106(31):12580–6.

167. Volkman JK, Barrerr SM, Blackburn SI, Sikes EL (1995) Alkenones in Gephyrocapsa oceanica: Implications for studies of paleoclimate. *Geochim Cosmochim Acta* 59(3):513–520.

168. Volkman JK, Eglinton G, Corner EDS, Sargent JR (1980) Novel unsaturated straight-chain C37-C39 methyl and ethyl ketones in marine sediments and a coccolithophore Emiliania huxleyi. *Phys Chem Earth* 12:219–227.

169. Marlowe IT, et al. (1984) Long chain (*n* -C_{37} –C_{39}) alkenones in the Prymnesiophyceae. Distribution of alkenones and other lipids and their taxonomic significance. *Br Phycol J* 19(3):203–216.

170. Volkman JK, et al. (1998) Microalgal biomarkers: A review of recent research developments. *Org Geochem* 29:1163–1179.

171. Sachs JP (2014) Hydrogen Isotope Signatures in the Lipids of Phytoplankton. *Treatise on Geochemistry*, eds Holland HD, Turekian KK (Elsevier, Oxford), pp 79–94. Second Edi.

172. Pierrot DEL, Wallace DWR (2006) MS Excel Program Developed for CO2 System Calculations. *Carbon Dioxide Inf Anal Center, Oak Ridge, Natl Lab US Dep Energy, Oak Ridge, Tennessee*.

173. Schmidt GA, Bigg GR, Rohling EJ (1999) Global Seawater Oxygen-18 Database – v1.21. *NASA Goddard Inst Sp Sci*. Available at: http://data.giss.nasa.gov/o18data/.